

(2)

# STUDY OF O<sub>2</sub> (<sup>1</sup>Δ) PRODUCTION BY NUCLEAR PUMPING

George H. Miley

University of Illinois  
Dept of Nuclear Engineering  
Urbana, IL 61801

April 1984

Final Report

Approved for public release; distribution unlimited.

DTIC  
ELECTE  
MAY 23 1984  
S B D

AIR FORCE WEAPONS LABORATORY  
Air Force Systems Command  
Kirtland Air Force Base, NM 87117

84 05 22 036

DTIC FILE COPY

AD-A141 463

This final report was prepared by the University of Illinois, Urbana, Illinois, under Contract DE-AS08-82DP40173, Job Order ILIR 8204, with the Air Force Weapons Laboratory, Kirtland Air Force Base, New Mexico. First Lieutenant David S. Bury (AREA) was the Laboratory Project Officer-in-Charge.

When Government drawings, specifications, or other data are used for any purpose other than in connection with a definitely Government-related procurement, the United States Government incurs no responsibility or any obligation whatsoever. The fact that the Government may have formulated or in any way supplied the said drawings, specifications, or other data, is not to be regarded by implication, or otherwise in any manner construed, as licensing the holder, or any other person or corporation; or as conveying any rights or permission to manufacture, use, or sell any patented invention that may in any way be related thereto.

This report has been authored by a contractor of the United States Government. Accordingly, the United States Government retains a nonexclusive, royalty-free license to publish or reproduce the material contained herein, or allow others to do so, for the United States Government purposes.

This report has been reviewed by the Public Affairs Office and is releasable to the National Technical Information Service (NTIS). At NTIS, it will be available to the general public, including foreign nations.

If your address has changed, if you wish to be removed from our mailing list, or if your organization no longer employs the addressee, please notify AFWL/AREA, Kirtland AFB, NM 87117 to help us maintain a current mailing list.

This technical report has been reviewed and is approved for publication.



DAVID S. BURY  
1Lt, USAF  
Project Officer

FOR THE COMMANDER



STAN G. HRNCIR, JR.  
Major, USAF  
Chief, Performance & Analysis Branch



KEITH G. GILBERT  
Colonel, USAF  
Chief, LEAPS Division

---

DO NOT RETURN COPIES OF THIS REPORT UNLESS CONTRACTUAL OBLIGATIONS OR NOTICE ON A SPECIFIC DOCUMENT REQUIRES THAT IT BE RETURNED.

UNCLASSIFIED

SECURITY CLASSIFICATION OF THIS PAGE

## REPORT DOCUMENTATION PAGE

1a. REPORT SECURITY CLASSIFICATION Unclassified			1b. RESTRICTIVE MARKINGS		
2a. SECURITY CLASSIFICATION AUTHORITY			3. DISTRIBUTION/AVAILABILITY OF REPORT Approved for public release; distribution Unlimited.		
2b. DECLASSIFICATION/DOWNGRADING SCHEDULE					
4. PERFORMING ORGANIZATION REPORT NUMBER(S)			5. MONITORING ORGANIZATION REPORT NUMBER(S) AFWL-TR-83-79		
6a. NAME OF PERFORMING ORGANIZATION University of Illinois		6b. OFFICE SYMBOL (If applicable)	7a. NAME OF MONITORING ORGANIZATION Department of Energy Nevada Operations Office		
6c. ADDRESS (City, State and ZIP Code) Dept of Nuclear Engineering Urbana, IL 61801			7b. ADDRESS (City, State and ZIP Code) P.O. Box 14100 Las Vegas, NV 89114		
8a. NAME OF FUNDING/SPONSORING ORGANIZATION Air Force Weapons Laboratory		8b. OFFICE SYMBOL (If applicable) AREA	9. PROCUREMENT INSTRUMENT IDENTIFICATION NUMBER DE-AS08-82DP40173		
8c. ADDRESS (City, State and ZIP Code) Kirtland Air Force Base, NM 87117 (1 to 10)			10. SOURCE OF FUNDING NOS.		
			PROGRAM ELEMENT NO. 61101F	PROJECT NO. ILIR	TASK NO. 82
					WORK UNIT NO. 04
11. TITLE (Include Security Classification) STUDY OF $O_2(^1\Delta)$ PRODUCTION BY NUCLEAR PUMPING					
12. PERSONAL AUTHOR(S) Miley, George H.					
13a. TYPE OF REPORT Final		13b. TIME COVERED FROM 82 Apr TO 83 Mar		14. DATE OF REPORT (Yr., Mo., Day) 1984, April	
15. PAGE COUNT 98					
16. SUPPLEMENTARY NOTATION					
17. COSATI CODES			18. SUBJECT TERMS (Continue on reverse if necessary and identify by block number)		
FIELD 20	GROUP 05	SUB. GR.	Nuclear Pumped Lasers Oxygen-Kinetics Iodine Lasers Ozone Production DELTA		
19. ABSTRACT (Continue on reverse if necessary and identify by block number) Experimental studies using a fast-burst neutron reactor to produce $O_2(^1\Delta)$ for use in an iodine transfer laser are described. It was found that nuclear induced discharges in Oxygen-buffer gas mixtures favor copious ozone production at the expense of $O_2(^1\Delta)$ concentrations. Experimental results, kinetics, and scaling relations are given. Additional theoretical analyses of $O_2(^1\Delta)$ production at high pressure using nuclear-pumped flash-lamp photolysis of the ozone indicates an alternate practical method of $O_2(^1\Delta)$ generation for use in high power transfer lasers.					
20. DISTRIBUTION/AVAILABILITY OF ABSTRACT UNCLASSIFIED/UNLIMITED <input checked="" type="checkbox"/> SAME AS RPT. <input type="checkbox"/> DTIC USERS <input type="checkbox"/>			21. ABSTRACT SECURITY CLASSIFICATION Unclassified		
22a. NAME OF RESPONSIBLE INDIVIDUAL 1Lt David S. Bury			22b. TELEPHONE NUMBER (Include Area Code) (505) 844-2995		22c. OFFICE SYMBOL AREA

# TABLE OF CONTENTS

	<u>Page</u>
I. INTRODUCTION. . . . .	1
II. O <sub>2</sub> ( <sup>1</sup> Δ) PRODUCTION BY OZONE PHOTOLYSIS . . . . .	3
1. Ozone Measurements. . . . .	5
2. Ozone Photolysis Calculations . . . . .	9
3. System Parametric Studies . . . . .	12
4. Nuclear-Pumped Flashlamp Concepts . . . . .	15
5. Conclusions . . . . .	19
III. DIRECT PUMPING OF O <sub>2</sub> ( <sup>1</sup> Δ). . . . .	20
1. Experimental Arrangement. . . . .	20
2. Detector Calibration. . . . .	22
3. Transport Measurements. . . . .	25
4. Parametric Studies. . . . .	30
5. In-Core Fiber Optic Diagnostic. . . . .	34
6. Kinetic Model . . . . .	39
7. Nuclear Sustained Electrical Discharge. . . . .	41
8. Conclusions . . . . .	43
IV. ACKNOWLEDGEMENTS. . . . .	47
Appendix A. Kinetic Model of Photolytic O <sub>2</sub> ( <sup>1</sup> Δ) Generation . . . . .	49
Appendix B. Kinetic Model of O <sub>2</sub> -Noble Gas Nuclear Irradiation . . . . .	67

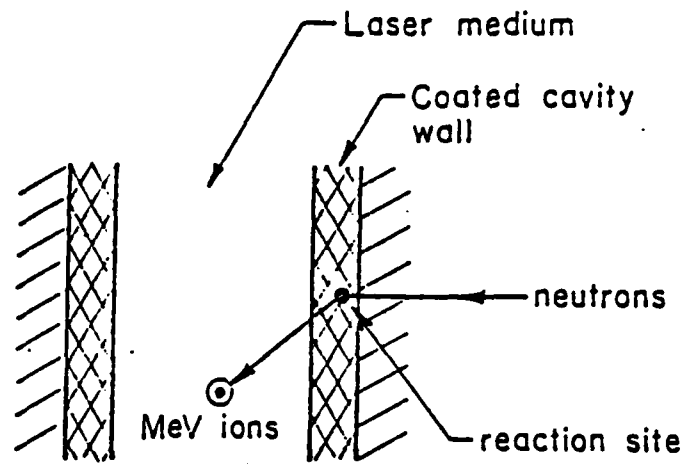


Accession For	
NTIS GRA&I	<input checked="checked" type="checkbox"/>
DTIC TAB	<input type="checkbox"/>
Unannounced	<input type="checkbox"/>
Justification	
By	
Distribution/	
Availability Codes	
Dist	Avail and/or Special
A-1	

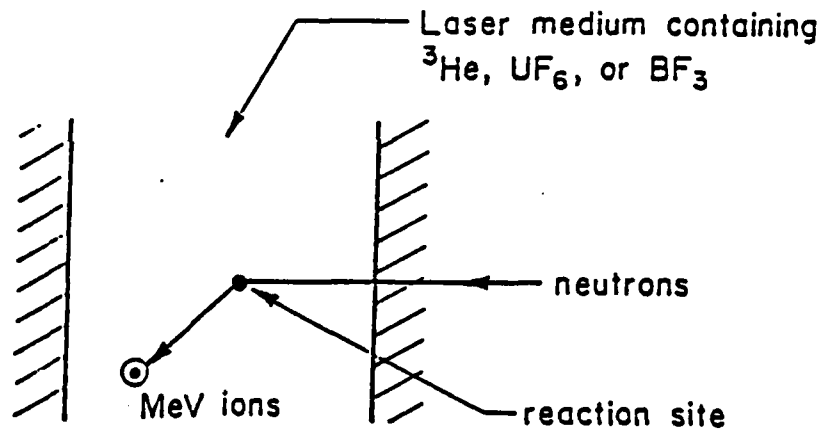
## I. INTRODUCTION

The main objective of this work was to determine  $O_2(^1\Delta)$  yield from the nuclear pumping of a noble gas- $O_2$  mixture. To achieve this goal it was necessary to benchmark a chemical kinetics model to predict the scaling of the  $O_2(^1\Delta)$  yield with noble gas pressure and with thermal neutron flux. A second goal was to test the suitability of nuclear produced  $O_2(^1\Delta)$  for the operation of an iodine laser. A third objective was to explore the potential of other methods for nuclear generation of  $O_2(^1\Delta)$ . This led to the identification of photolytic dissociation of ozone as a promising alternative to direct pumping of  $O_2(^1\Delta)$ .

A brief description of nuclear pumping is illustrated by Fig. 1A. The system typical of this set of experiments was an aluminum tube internally coated with Boron-10. The Boron-10 intercepts thermal neutrons escaping from the TRIGA reactor core and undergoes a nuclear reaction to generate MeV alpha particles and lithium ions. These ions stream through the gas creating ionization and excitation as they slow down, resulting in the formation of a plasma. An alternative approach to pumping the gas is shown in Fig. 1.B where the medium contains a gaseous pumping source i.e.,:  $^3He$ ,  $UF_6$  or  $BF_3$ . In the flashlamp studies proposed later in Section II.4, the photolytic fluorescer requires a volume source to achieve the required intensities.  $^3He$  is suggested for preliminary experiments since it is the easiest to handle. In a volume source, the thermal neutrons are captured by the reactive medium, resulting in nuclear reactions that generate MeV ions directly in the gas. The advantage of the volume source over a surface source is that virtually all of the energy released is deposited in the gas while with the surface source only a fraction of energy is deposited because ions travelling in the wrong direction are absorbed by the coating or the tube wall.



A. Coated tube design



B. Volume source design

Figure 1 Nuclear pumping sources are of two forms; A) a surface source where the high energy ions are created in a coating on the walls of the cell, or B) a volume source where a gas additive is used to create the high energy ions in the plasma.

In the following section we first discuss the results that lead to the proposal for  $O_2(^1\Delta)$  production by nuclear photolysis of ozone. In Section III experimental data obtained from measurement of direct nuclear pumping of  $O_2(^1\Delta)$  are presented. This includes results from transport measurements, parametric studies, and kinetic modeling. Also a summary of operating parameters observed for a nuclear sustained electrical discharge is included. This device was developed for steady-state generation of  $O_2(^1\Delta)$  and was used in the transport studies.

## II. $O_2(^1\Delta)$ PRODUCTION BY OZONE PHOTOLYSIS

A key discovery during this work was the realization that nuclear pumping favors the generation of ozone, particularly at higher pressures. In order to capitalize on this result, we considered the photolytic decomposition of ozone into  $O_2(^1\Delta)$  as an alternative. The peak ozone yield observed in a preliminary experiment was approximately 0.5 Torr  $O_3$  in a 4000 Torr He, 20 Torr  $O_2$  mixture at the observation cell. Based on a computer model for the decomposition of ozone by a KrF\* fluorecor ( $\lambda = 249$  nm), it appears to be possible to obtain  $> 5$  Torr  $O_2(^1\Delta)$  starting with the 0.5 Torr of  $O_3$  cited above. (Taking into consideration the gas expansion, then between 1 to 2 Torr peak  $O_3$  exists in the irradiation zone.) The computer model indicates that with an initial  $O_3$  pressure of 2 Torr,  $\sim 7$  Torr of  $O_2(^1\Delta)$  can be generated, representing a 35% concentration with respect to the total oxygen pressure. Furthermore, it appears that the nuclear-pumped flashlamp intensities necessary to completely dissociate the ozone are within current technology.

Figure 2 shows a straight flow-through design which would use a relatively fast flow rate to generate the ozone in the first half of the reactor pulse and photolyze the  $O_3$  into  $O_2(^1\Delta)$  during the second half of the pulse. Based on preliminary experiments, the nuclear production of ozone appears to be relatively efficient. The main production mechanism

FSL-82-178

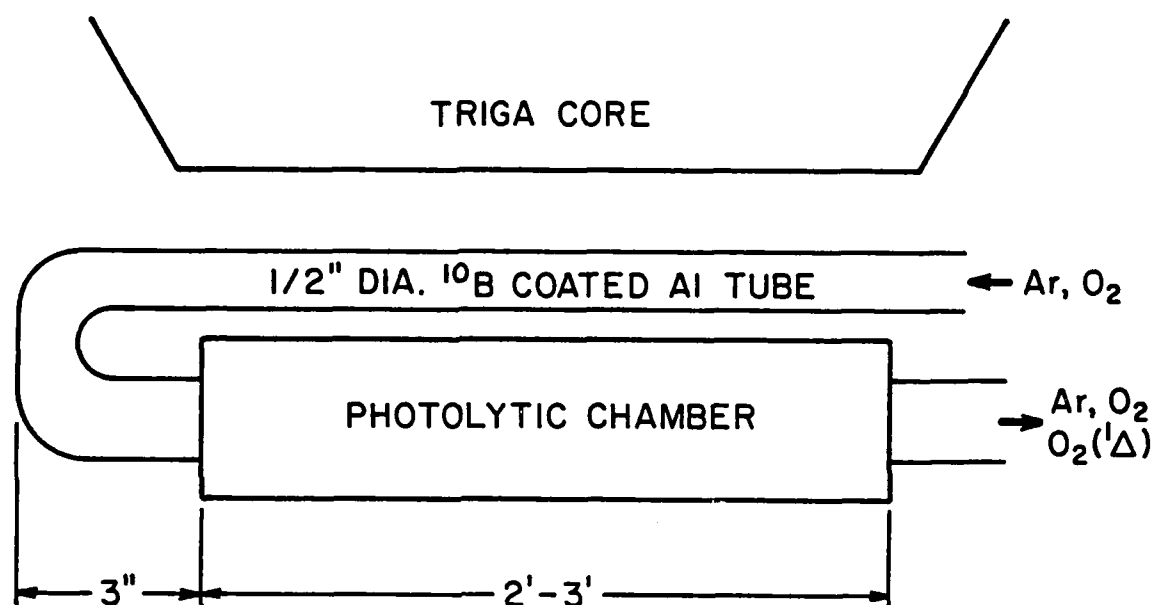


Fig. 2. Combined nuclear pumping and photolytic chamber for converting  $O_3$  in the afterglow to  $O_2(^1\Delta)$  via photodissociation. In this diagram the photolytic source is nuclear pumped by the  $^3\text{He}(n,p)\text{T}$  reaction.



that appears to be responsible for ozone production is three-body recombination of ground state atomic oxygen with ground state molecular oxygen in the presence of a third body such as helium or oxygen.

### 1. Ozone Measurements

The experimental apparatus that was used to determine the ozone concentration is shown in Figure 3. The reaction zone consisted of a 1.27 cm diameter Boron-10 coated aluminum tube 60 cm long which was placed adjacent to the TRIGA core. The excited He-O<sub>2</sub> mixture was then flowed through 10 meters of tubing (polyflow) to an absorption cell where the ozone concentration was measured. The detection of O<sub>3</sub> was accomplished with a He-Hg lamp radiating at 2537 Å, monitored by an RCA-31034 photomultiplier coupled to a Heath monochromator. In the case of the high pressure studies, the gas was simply vented out of the tube. At pressures below 1 atmosphere, an oxygen serviced vacuum pump was employed.

Experimental results from this system are shown in Figures 4 and 5. In Figure 4 the ozone pressure increases relatively rapidly with increasing He pressure and appears to saturate at around 3500 Torr of He. This saturation is attributed to power deposition saturation. This problem can be overcome with a smaller diameter tube that allows the alpha particles to reach the centerline at desired maximum pressure. However, this was not attempted in present experiments. The solid line in this figure shows the actual experimental data (approximately 0.5 Torr of ozone at the observation point 10 meters from the initial excitation zone). If the expansion of the excited gas slug is taken into account, the equivalent ozone pressure in the excitation zone in the core is estimated to be

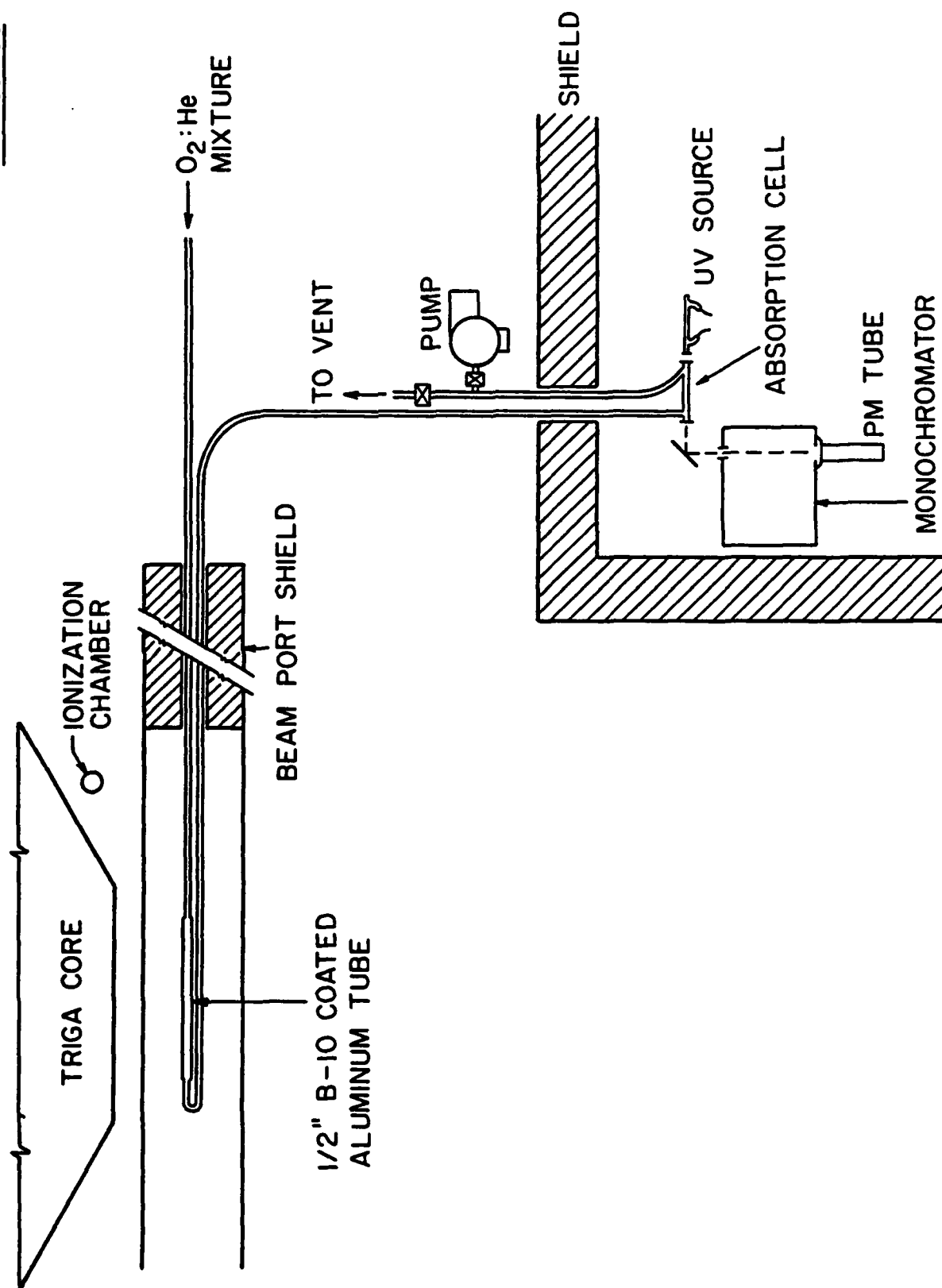


Fig. 3 Experimental apparatus used to monitor  $O_3$  yields from nuclear pumping.

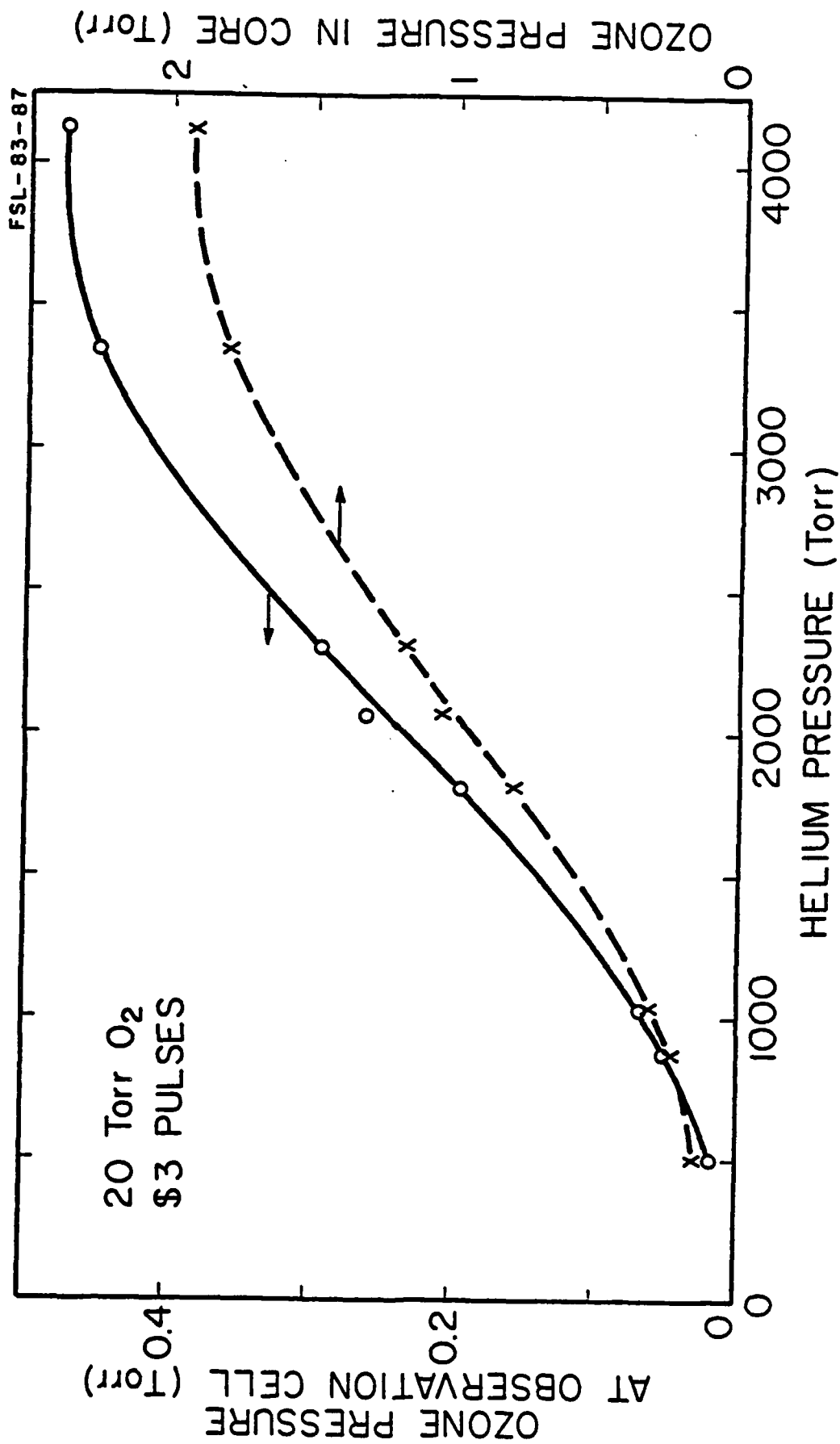


Fig. 4 Experimental results obtained with the apparatus diagram

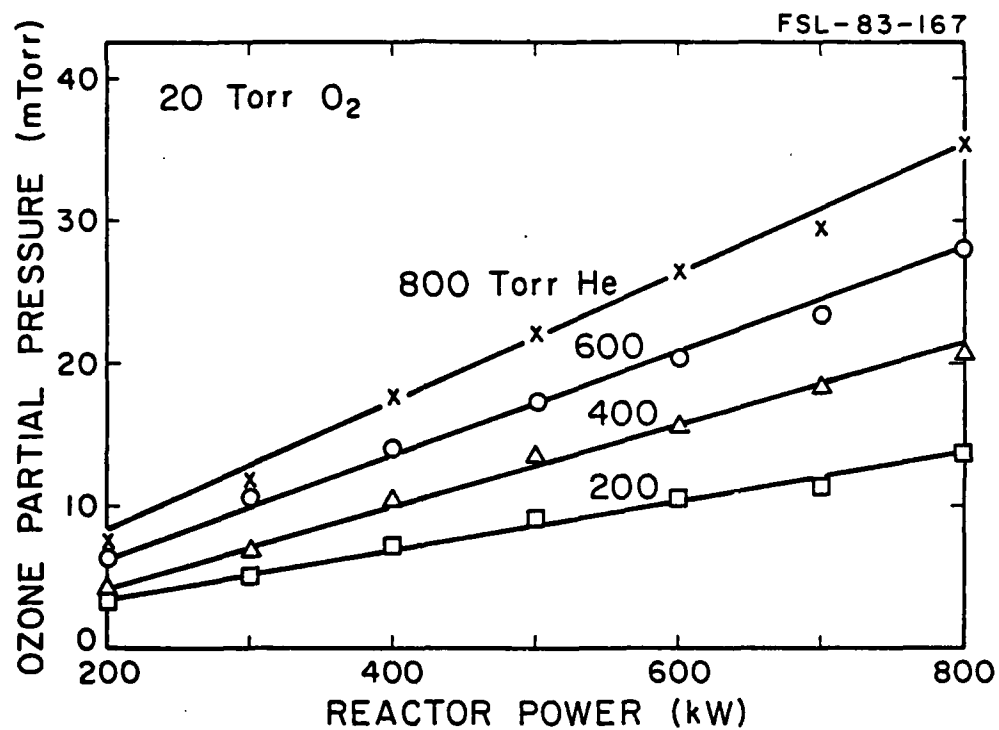


Fig. 5 Experimental results for ozone production from CW irradiation of He:O<sub>2</sub> mixtures.

approximately 2 Torr. These  $O_3$  yields are more than more than sufficient for the  $O_2(^1\Delta)$  generation technique suggested in the following section. Results shown in Figure 5 were obtained for cw operation of the reactor, eliminating the uncertainty associated with expansion of the gas slug. The increase of ozone yield with power deposition is clearly demonstrated by these results.

## 2. Ozone Photolysis Calculations

In the photolytic generation of  $O_2(^1\Delta)$  from ozone, a rather unique process can be exploited. First, the  $O_3$  is rapidly decomposed by UV light (typically less than 300 nanometers and greater than 230 nanometers) into  $O_2(^1\Delta)$  and  $O(^1D)$ . The  $O(^1D)$  is rapidly quenched by other species to ground state atomic oxygen which can then undergo three-body recombination with ground state molecular oxygen and a third body (e.g. He) to form ozone (see Figure 6). This mechanism forms a positive feedback which enhances the  $O_2(^1\Delta)$  concentrations by as much as an order of magnitude compared to the initial ozone concentrations. This technique operates best at high pressures where the three-body recombination process is fast throughout the pulse.

Note that, as shown in Figure 6, the ozone is initially photolyzed into  $O_2(^1\Delta)$  and  $O(^1D)$  or  $O(^3P)$  and  $O_2(^3\Sigma)$ . In the present calculation a 90% branching ratio was assumed for the  $O_2(^1\Delta) - O(^1D)$  channel. This is a rather conservative estimate since much of the recent literature states that this branching ratio is approximately unity (see Appendix A).

A fairly detailed kinetic model has been developed for calculation of  $O_3$  photolysis yield. This model is described in more detail in Appendix A. Results from these calculations, shown in Figure 10, indicate that as the flashlamp power increases, the ozone concentration slowly decreases.

FSL-83-168

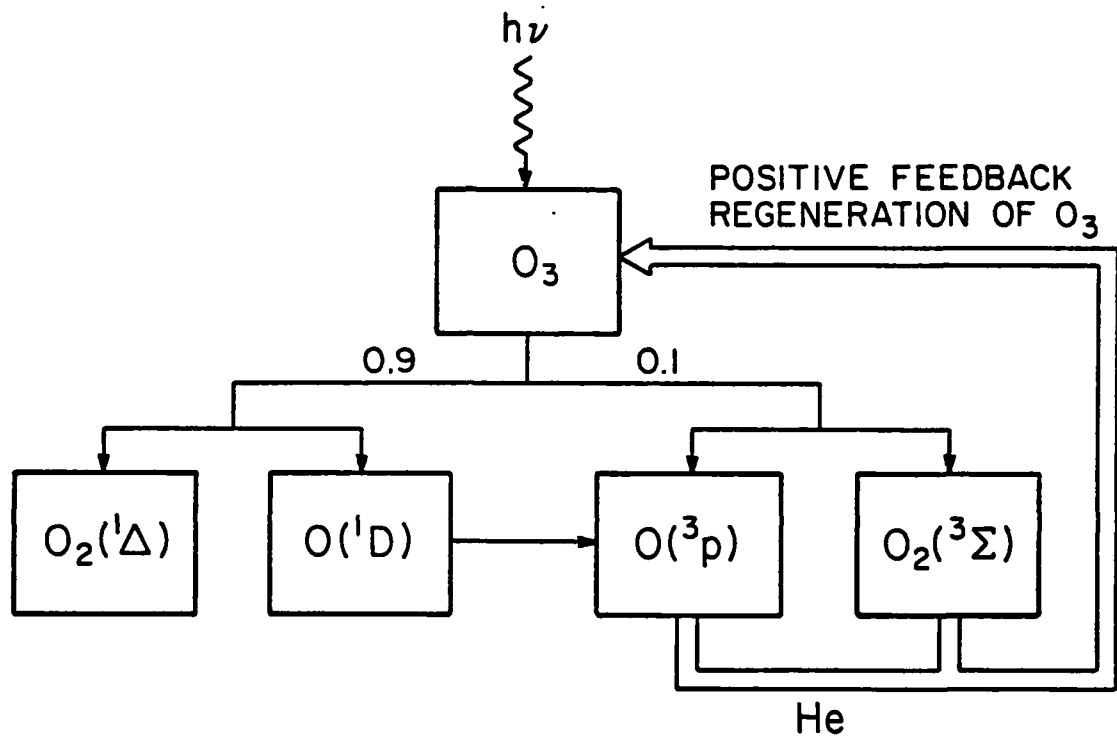


Fig. 6 Schematic of positive feedback mechanism which leads to an enhanced  $O_2(^1\Delta)$  yield.

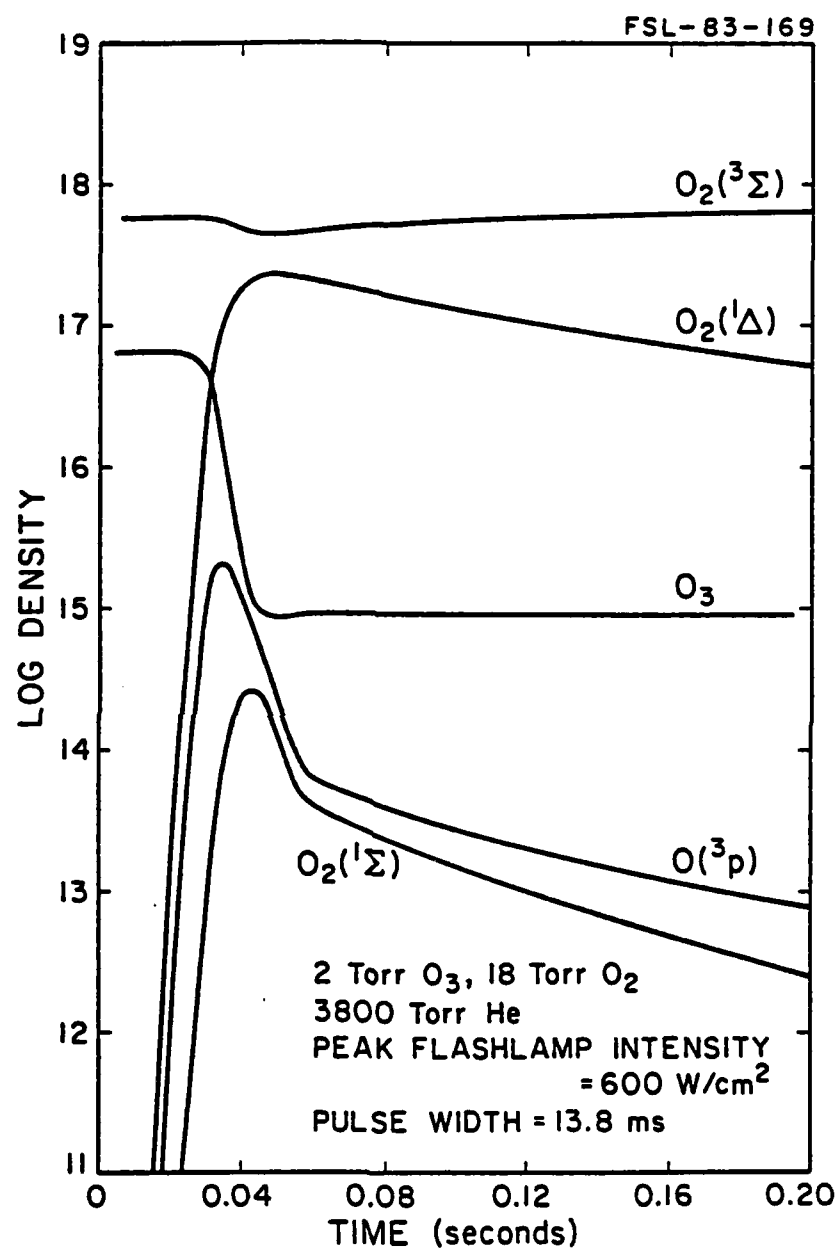


Fig. 7 Time dependent solution of chemical kinetics

$$\frac{[O_2(^1\Delta)]}{[O_2(^3\Sigma)]} \sim .5$$

$$[O_2(^1\Delta)] \simeq 7 \text{ Torr}$$

The peak flashlamp intensity assumed was  $600 \text{ W/cm}^2$  which appears to be achievable with current nuclear pumping technology. The rise in the atomic oxygen concentration is a direct result of the photolytic decomposition of the ozone. The  $\text{O}_2(^1\Delta)$  concentration exceeds the ozone concentration almost immediately due to the positive feedback mechanism already outlined. This calculation suggests that starting with 2 Torr of ozone, up to 7 Torr of  $\text{O}_2(^1\Delta)$  can be produced. This represents an  $\text{O}_2(^1\Delta)$  concentration equal to 35% of the total oxygen concentration, well above the requirements for pumping an iodine laser.

The next several figures show the  $\text{O}_2(^1\Delta)$  yield as a function of partial and total mixture pressure, flashlamp intensity and duration. This parametric study indicates that a flashlamp peak intensity of  $150 \text{ W/cm}^2$  is all that is necessary to create the  $\text{O}_2(^1\Delta)$  concentration ( $> 17\%$ ) required for operation of an iodine laser.

The most interesting point of Figure 8 is that if the flashlamp intensity falls between  $600\text{-}1000 \text{ W/cm}^2$ , this technique can generate approximately 7-8 Torr of  $\text{O}_2(^1\Delta)$  from a mixture of 18 Torr  $\text{O}_2$ , 2 Torr  $\text{O}_3$ , and 3800 Torr He. For a reduced ozone pressure (0.5 Torr ozone) and the above flashlamp intensity, between 5 and 6 Torr of  $\text{O}_2(^1\Delta)$  will be generated. Thus, there is a broad range over which significant  $\text{O}_2(^1\Delta)$  yields can be obtained.

### 3. System Parametric Studies

We have found that the three-body recombination rate for ozone formation increases directly with He pressures. Thus the enhancement mechanism for  $\text{O}_2(^1\Delta)$  production from the photolytic decomposition of ozone increases. This is apparent in Figure 9 which graphs the  $\text{O}_2(^1\Delta)$  yield as a function of the He pressure and as a function of various flashlamp intensities. It is important to remember that as the flashlamp



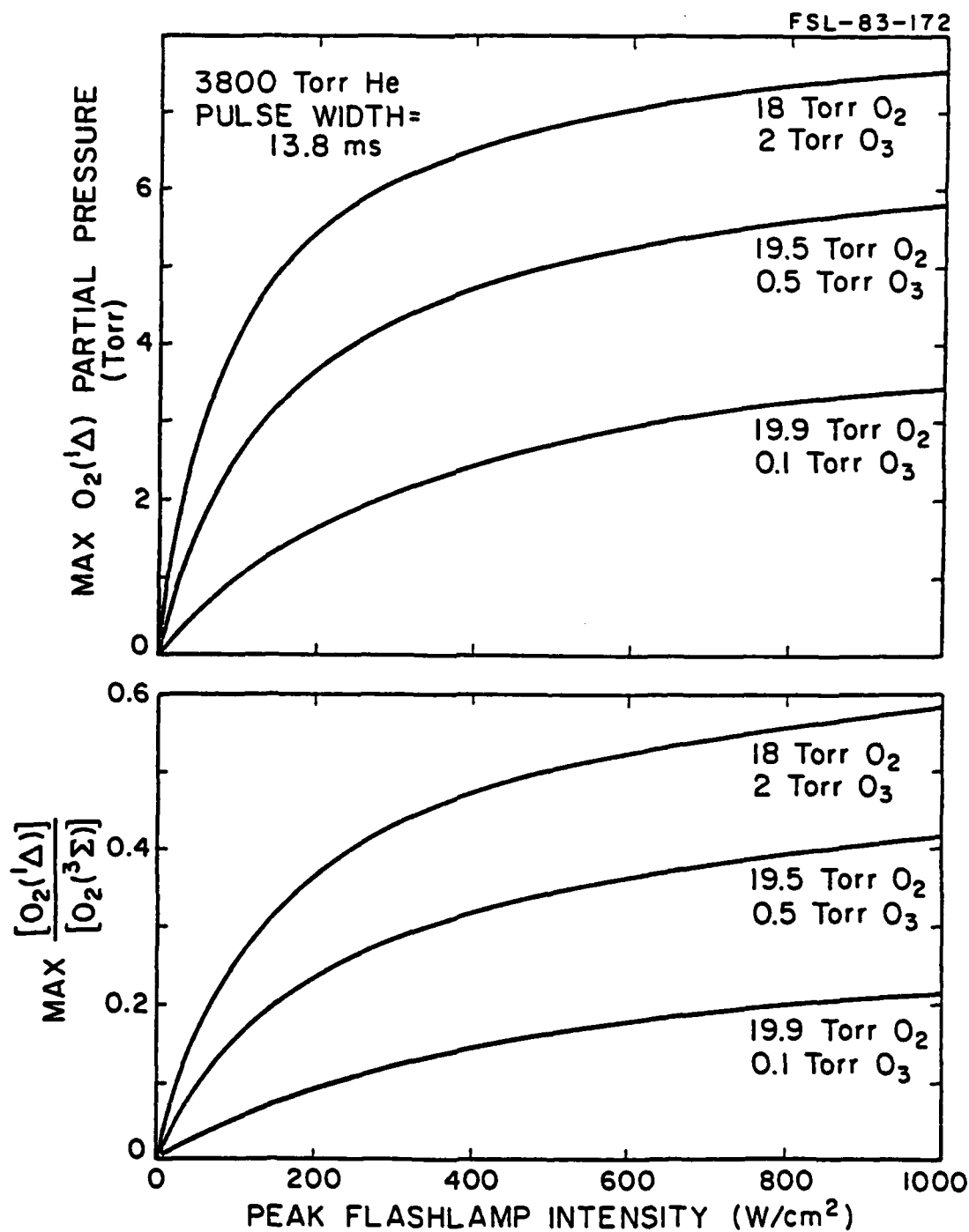


Fig. 8 Parametric study of the  $O_2(^1\Delta)$  yield as a function of the flashlamp intensity for various  $O_3:O_2$  mixtures.

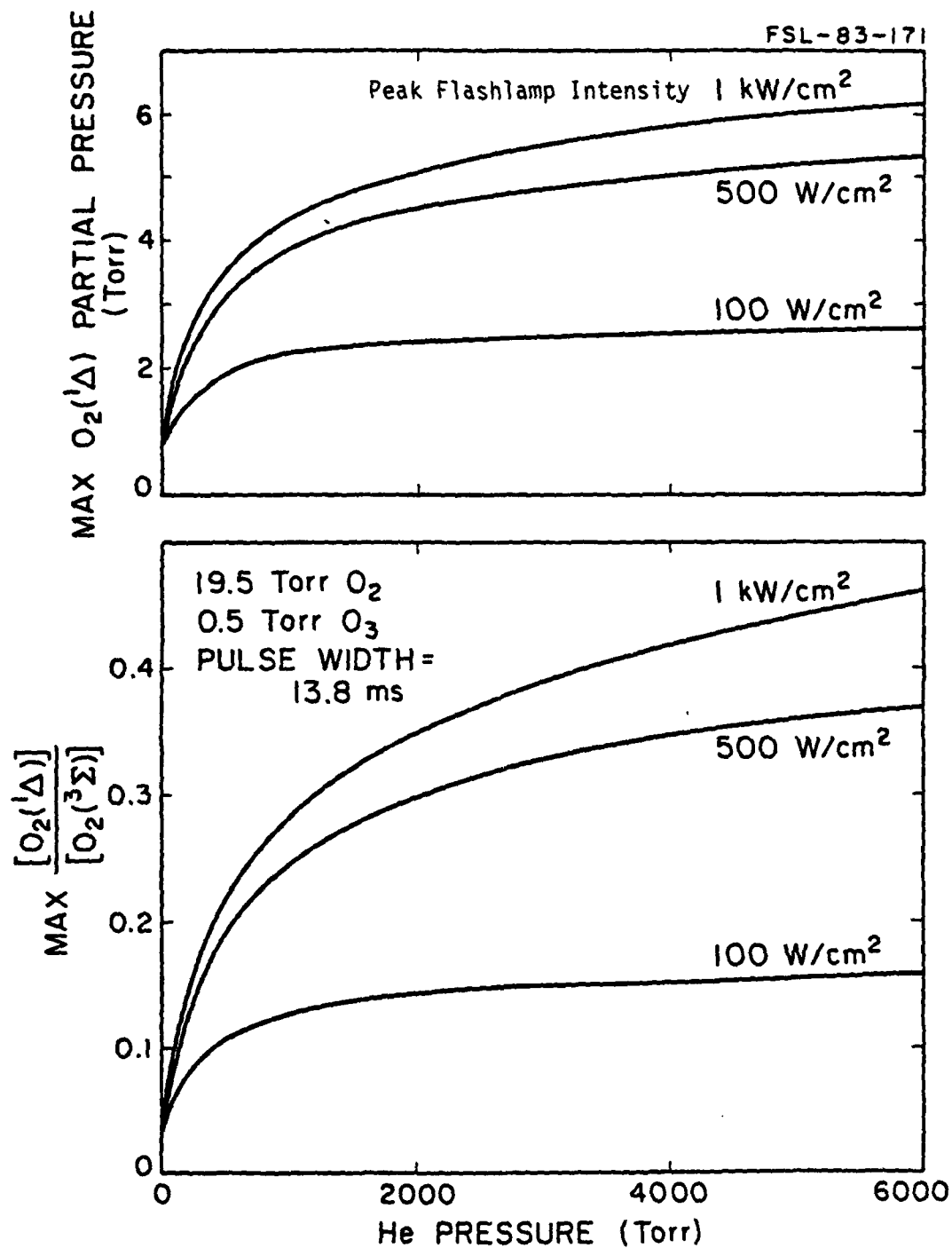


Fig. 9 The feedback mechanism proceeds more effectively at higher He pressures.

intensity increases the depletion of the ozone during the pulse increases. Since ozone strongly quenches  $O_2(^1\Delta)$ , the  $O_2(^1\Delta)$  lifetime increases. As a result, higher yields of  $O_2(^1\Delta)$  are achieved with higher flashlamp intensities. This point is also brought out in Figure 10 where with a 1 KW/cm<sup>2</sup> peak flashlamp intensity, 7.5 Torr  $O_2(^1\Delta)$  with an  $[O_2(^1\Delta)]/[O_2(^3\Sigma)]$  ratio of .58 is generated. The effective half-life of the generated  $O_2(^1\Delta)$  is 70 ms. A further increase in the effective lifetime of  $O_2(^1\Delta)$  is possible using a more intense UV source.

Figure 11 shows the dependence of  $O_2(^1\Delta)$  yield on flashlamp duration for different  $O_2:O_3$  mixtures and for a constant peak flashlamp intensity. The production efficiency of  $O_2(^1\Delta)$  is large for shorter pulses because of the rapid decomposition of  $O_3$  which, as already noted, is a strong quencher of  $O_2(^1\Delta)$ .

Thus, from this parametric study we conclude that  $O_2(^1\Delta)$  production by this method is suitable for iodine laser operation. Experimental testing of this model, however, is still needed in order to verify these results and determine optimum conditions.

#### 4. Nuclear-Pumped Flashlamp Concepts

A nuclear-pumped flashlamp concept for use in this scheme is illustrated in Figure 12. In this approach the high power densities needed at the center tube section (where the flowing ozone-helium mixture passes) are achieved by geometric focussing using a highly polished aluminum surface. This focussing concept concentrates the light generated in the large fluorescor volume while transferring it to the smaller volume of a very highly absorbing medium, in this case ozone. A possible fluorescor is KrF\* which emits at a wavelength of 249 nanometers, roughly the peak of the

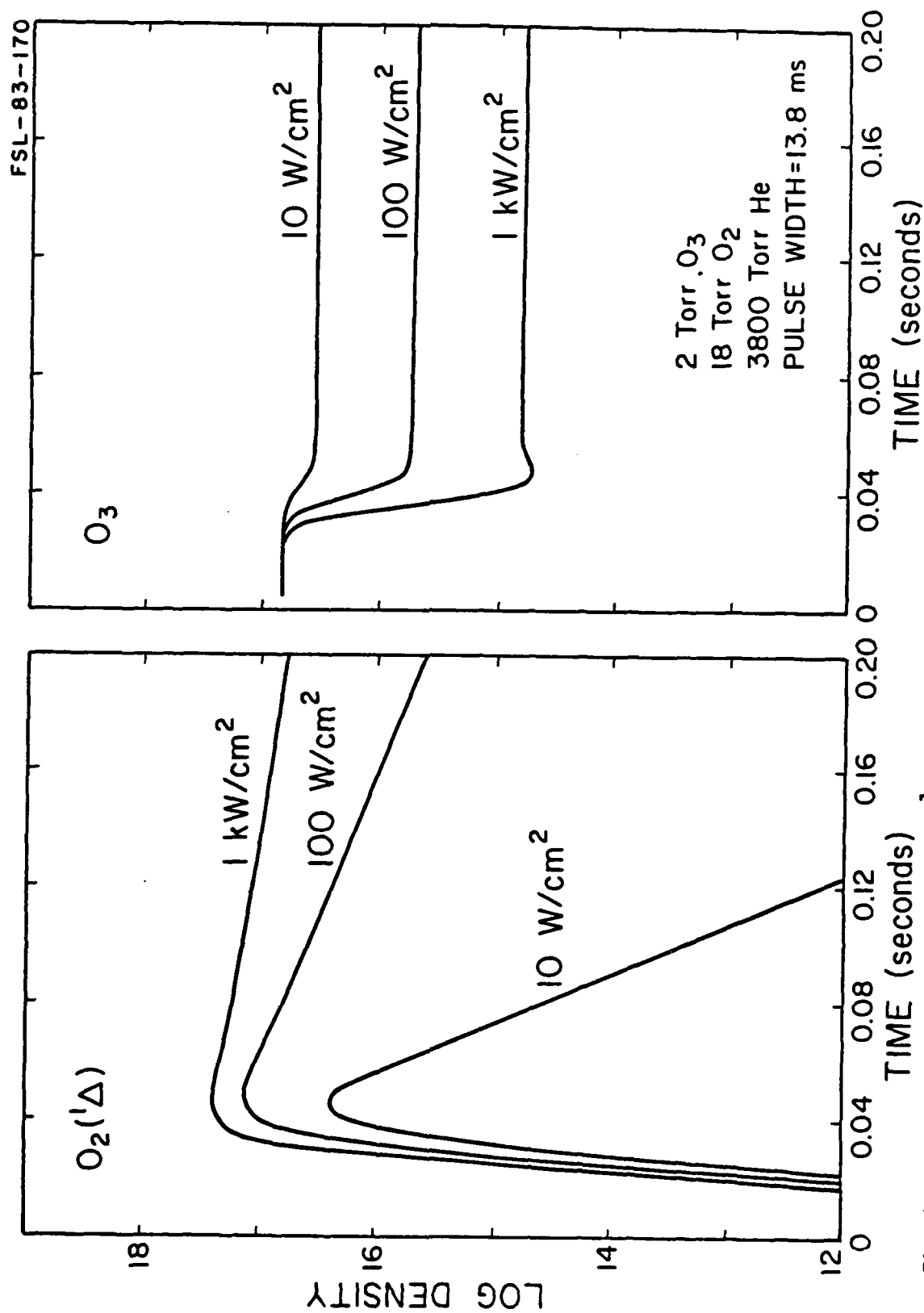


Fig. 10 Demonstration of increased  $O_2(^1\Delta)$  production and lifetime as a result of the enhanced  $O_3$  photodecomposition rate at higher flashlamp intensities.

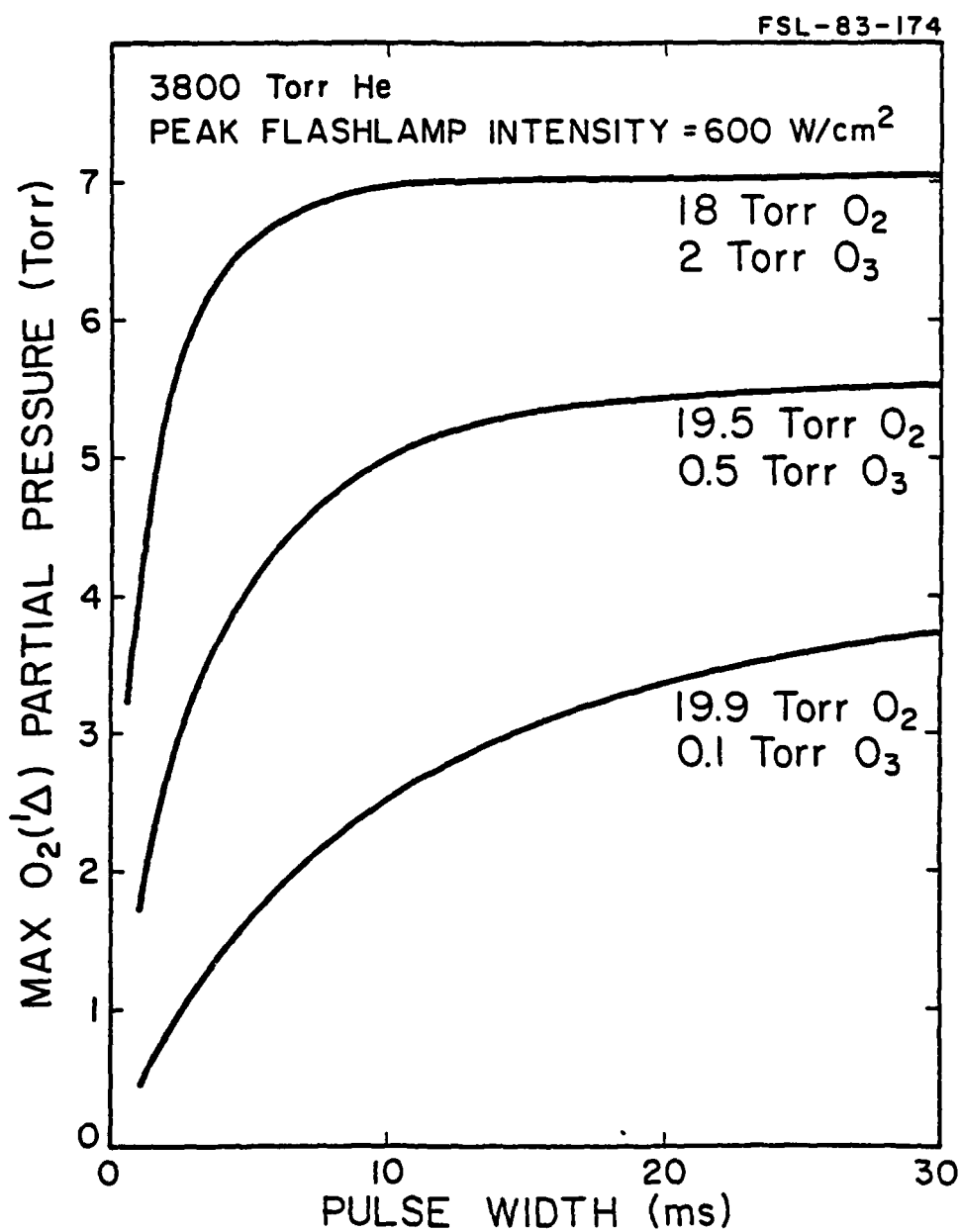


Fig. 11 O<sub>2</sub>(<sup>1</sup>Δ) production efficiency is greater for shorter pulses because of the rapid decomposition of O<sub>3</sub>.

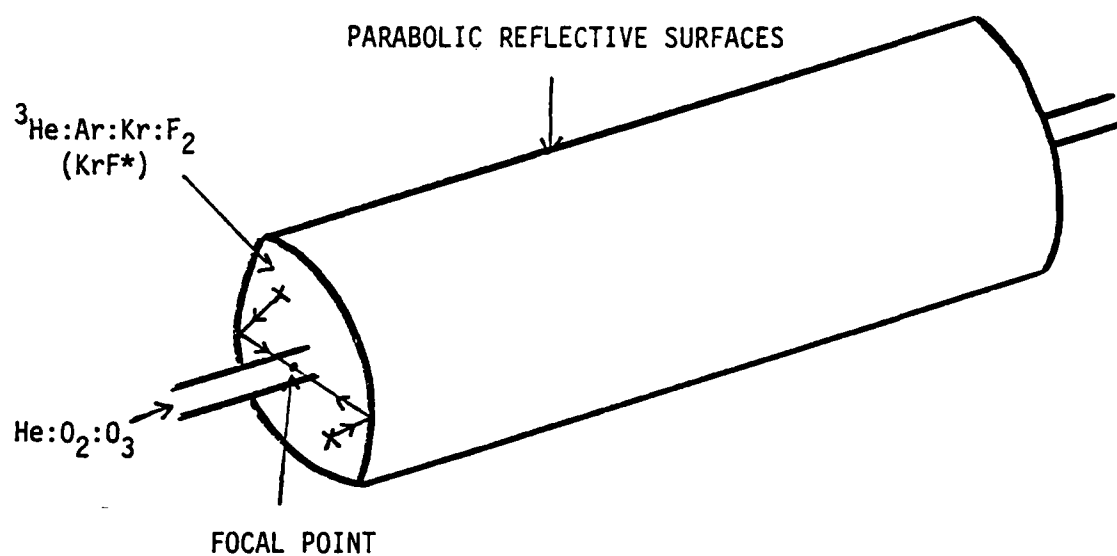


Fig. 12 A nuclear pumped flashlamp design which can focus the fluorescence from a large volume to a smaller volume resulting in a net increase in the intensity in the center cell.

ozone absorption cross section ( $\sim 11$  megabarns). The nuclear-induced fluorescence efficiency defined as ratio fluorescence energy to energy deposited in the fluorescence media has been calculated to be approximately 14% for KrF\*, a reasonably high value. The flashlamp intensity is a function of the power deposited in the fluorecor, the fluorecor efficiency, the coupling efficiency of the fluorescence to the inner-cell and the ratio of the volume of the fluorecor to the surface area of the ozone cell. Thus:

$$I_{\text{lamp}} = [P_{\text{in}} (\text{fluorecor})] [\eta_{\text{coupling}}] \frac{[\text{Volume of Fluorecor}]}{[\text{Surface area of absorber}]}$$

Then, for a TRIGA reactor which has a thermal neutron flux of approximately  $2.5 \times 10^{15} \text{ n/cm}^2\text{s}$ , the power deposition in 5 atms of  $^3\text{He}$  will be approximately  $120 \text{ W/cm}^3$ . If a parabolic reflector is assumed with a coupling efficiency of 80% to the inner cell, then for a flashlamp intensity of  $1 \text{ kW/cm}^2$ , the ratio required for the flashlamp volume to the surface area of the ozone cell is  $\sim 75$ .

### 5. Conclusions

In conclusion, the nuclear generation of  $\text{O}_2(^1\Delta)$  by the photolysis of ozone appears very promising. Indeed, a TRIGA reactor neutron pulse can generate workable yields. The theoretical scheme examined used a KrF-excimer flashlamp to photodissociate the ozone. This generates  $\text{O}_2(^1\Delta)$  directly along with atomic oxygen. The latter results in a feedback mechanism which greatly enhances  $\text{O}_2(^1\Delta)$  yields. For the case of 0.5 Torr  $\text{O}_3$ , 19.5 Torr  $\text{O}_2$ , and 3800 Torr He (corresponding to experimental ozone yields) and a  $1 \text{ kW/cm}^2$  flashlamp, the  $\text{O}_2(^1\Delta)$  yield will be approximately 10 Torr, corresponding to 30% of the total  $\text{O}_2$  concentration. The associated half-life of the  $\text{O}_2(^1\Delta)$  is estimated to be  $\sim 70 \text{ ms}$ .

### III. DIRECT PUMPING OF $O_2(^1\Delta)$

The idea which has just been discussed is a direct result of the experiments that were conducted on the direct nuclear pumping of Ar- $O_2$  to form  $O_2(^1\Delta)$ . These studies revealed that the most important species present in the afterglow is ozone. Consequently, the scheme just described would take advantage of the large ozone yield. The work which will now be discussed involved initial experiments on direct pumping of  $O_2(^1\Delta)$  and the associated development of reliable diagnostics for these and subsequent experiments.

The techniques developed used a flowing afterglow design with a Boron-10 coated excitation cell coupled to a 6-meter flow path of pyrex tubing. The tubing transported the excited gas slug from the radiation zone to the detectors which were located behind concrete shielding to reduce radiation noise. Another diagnostic developed was an in-core fiber optic designed to be highly resistant to both radiation damage and radiation-induced fluorescence. These techniques were then used to determine both  $O_2(^1\Delta)$  and  $O_3$  yields from a direct nuclear pumped system and also from a hybrid nuclear-electrical system. Emissions at 1.27 microns and at  $6340 \text{ \AA}$  were used to determine the  $O_2(^1\Delta)$  concentration. The ozone was simultaneously monitored by the absorption of the  $2537\text{-\AA}$  line from a mercury discharge directed through an observation cell approximately 108-cm long. These results were applied as the benchmark to the modeling which was then used to estimate how the  $O_2(^1\Delta)$  yield scales with increasing noble gas pressure and also with the reactor power levels.

#### 1. Experimental Arrangement

The experimental apparatus is diagrammed in Figure 13. The  $O_2(^1\Delta)$  was generated in an aluminum tube coated on the inside with Boron-10 and placed adjacent to the TRIGA reactor core. The argon and oxygen mixture is



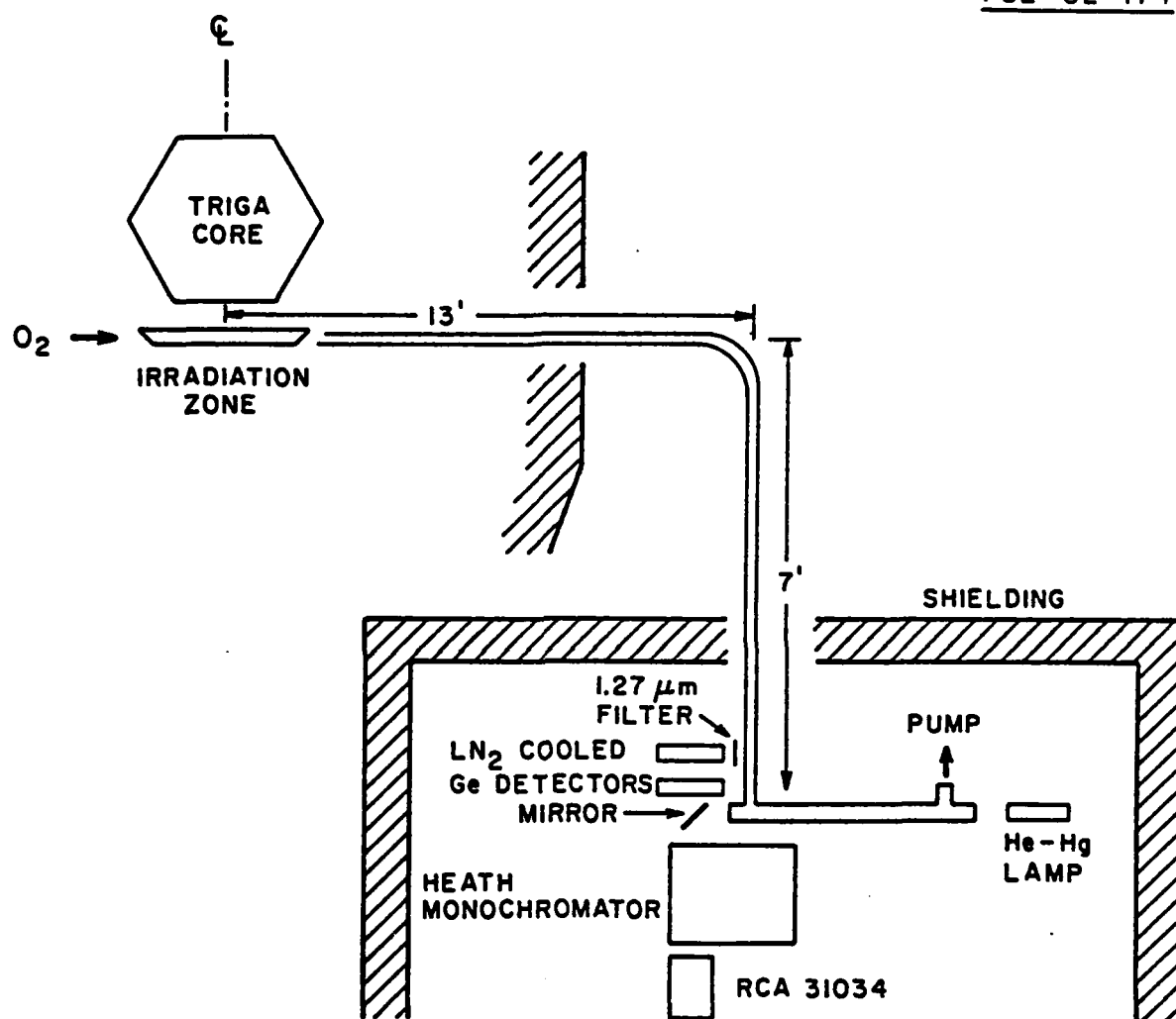
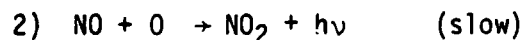
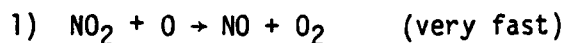


Fig. 13 Experimental set-up for monitoring  $O_2$  ( $^1\Delta$ ) at 1.27  $\mu m$ . Also, the  $O_3$  density is determined with the absorption of 2537  $\text{\AA}$  light from a He-Hg lamp.

were flowed through this excitation cell into a 6-meter long pyrex vacuum-line which transported the gas from the radiation zone to the detectors. The flow velocities, on the order of 20 meters per second, were provided by a roots-type pump. A  $\text{LN}_2$  cooled germanium detector with an interference filter centered at 1.27 microns was used to observe the emissions from  $\text{O}_2(^1\Delta)$ . A second detector, also a germanium unit, was used without a filter to monitor broadband emissions. By monitoring the emissions from 900 nm - 1.4  $\mu\text{m}$  and comparing their behavior to the 1.27  $\mu\text{m}$  line it is possible to determine how much the  $\text{NO} + \text{O}$  afterglow (caused by  $\text{N}_2$  impurities) affects the  $\text{O}_2(^1\Delta)$  measurements. Also depicted in this figure is the helium mercury lamp which illuminated the observation cell with UV light (2537Å). Ozone concentrations were determined by absorption of this light as monitored by a Heath monochromator coupled to an RCA 31034 photomultiplier. The shielding shown was necessary to prevent radiation from the reactor pulse from reaching the germanium detectors, which are highly susceptible to interference from gamma and x-ray radiation.

## 2. Detector Calibration

The detector calibration technique used a relatively straightforward method that involves a flowing afterglow with an  $\text{NO}_2$  titration. The technique relied upon the following reactions:



and the derived relation:

$$3) K_{\text{DET}} = K \frac{[\text{O}][\text{NO}]}{I_{\text{NO}}}$$

where  $K_{\text{DET}}$  = detector calibration constant

$K$  = literature constants

$[\text{O}]$  = atomic oxygen concentration

$[\text{NO}]$  = nitric oxide concentration

$I_{\text{NO}}$  = observed intensity of  $\text{NO-O}$  glow.

The above set of reactions is rather unique because the large difference in their reaction rates allows for a simple method of determining the atomic oxygen concentration. Suppose, for example, the  $\text{NO}_2$  and atomic oxygen concentrations are made equal. Reaction 1 will very quickly exhaust the supply of atomic oxygen. Since there is no regenerative mechanism for atomic oxygen in this system once it is gone, both reactions will cease. As a result, the light emitted by reaction 2 will "disappear." So by reversing the above argument, the termination of the  $\text{NO} + \text{O}$  afterglow represents the titration end point where the  $\text{NO}_2$  and atomic oxygen concentrations are equal.

The experimental apparatus used for the calibration is shown in Figure 14. As the  $\text{O}_2$  passes through the microwave cavity, it forms atomic oxygen,  $\text{O}_2(^1\Delta)$ , and various other species. The flow tube for viewing the afterglow is isolated from the discharge by a light trap downstream of the microwave cavity. The  $\text{NO}_2$  is injected with a small port upstream of the infrared detector which views the 1.27-micron emissions from both the  $\text{NO}_2$  glow and the  $\text{O}_2(^1\Delta)$ . The contribution from  $\text{O}_2(^1\Delta)$  is subtracted out of the signal through an initial background measurement (no  $\text{NO}_2$ ). This allows a direct measurement of  $I_{\text{NO}}$ . Then, by performing an  $\text{NO}_2$  titration as described above, the atomic oxygen concentration is readily obtained. Finally, since reaction 1 is so fast compared to 2, the  $\text{NO}$  concentration can be taken as the initial  $\text{NO}_2$  concentration.

The  $\text{NO}_2$  flow rate is then measured using a calibrated volume technique. At the appropriate  $\text{NO}_2$  flow rate, the flow is diverted into an evacuated calibrated volume. The time required for the calibrated volume to fill to a given pressure gives the flow rate of the  $\text{NO}_2$ . This technique is very reliable since the relatively long fill times involved result in a high accuracy in the flow rate determination.

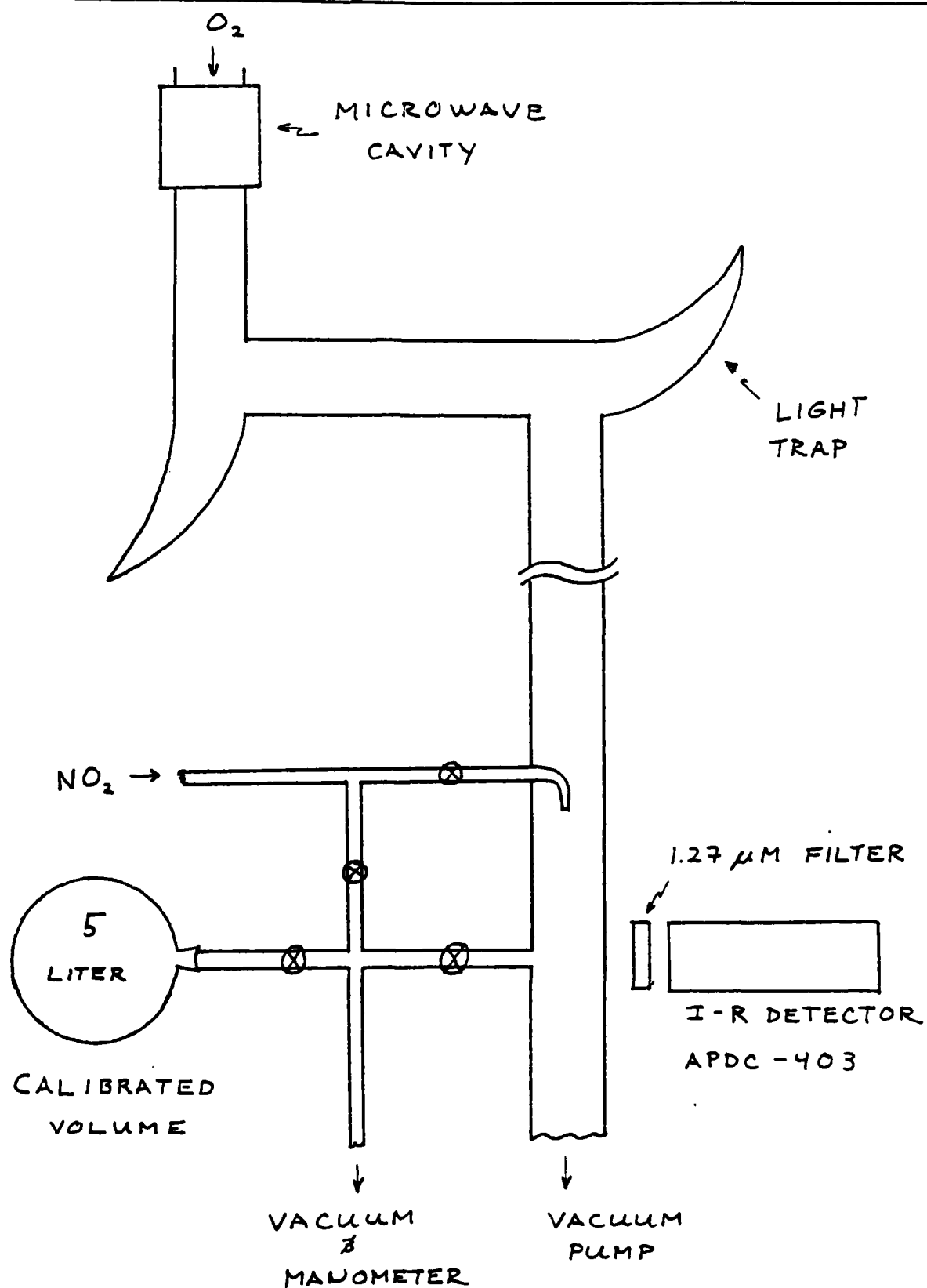


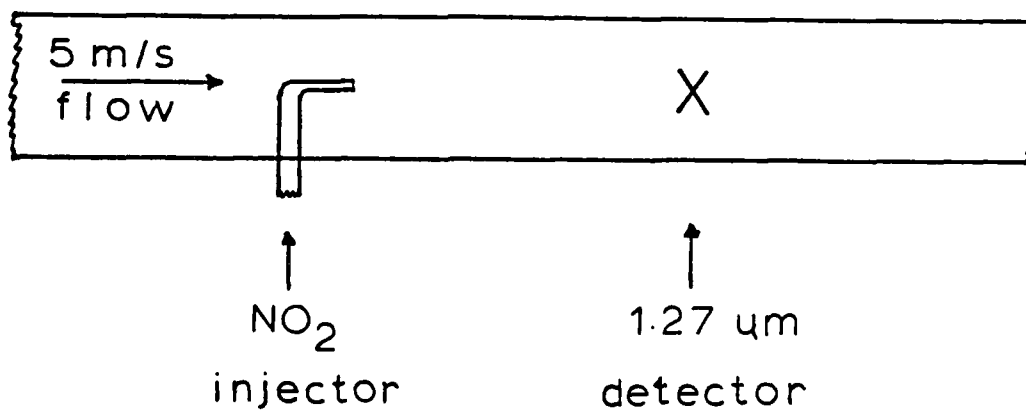
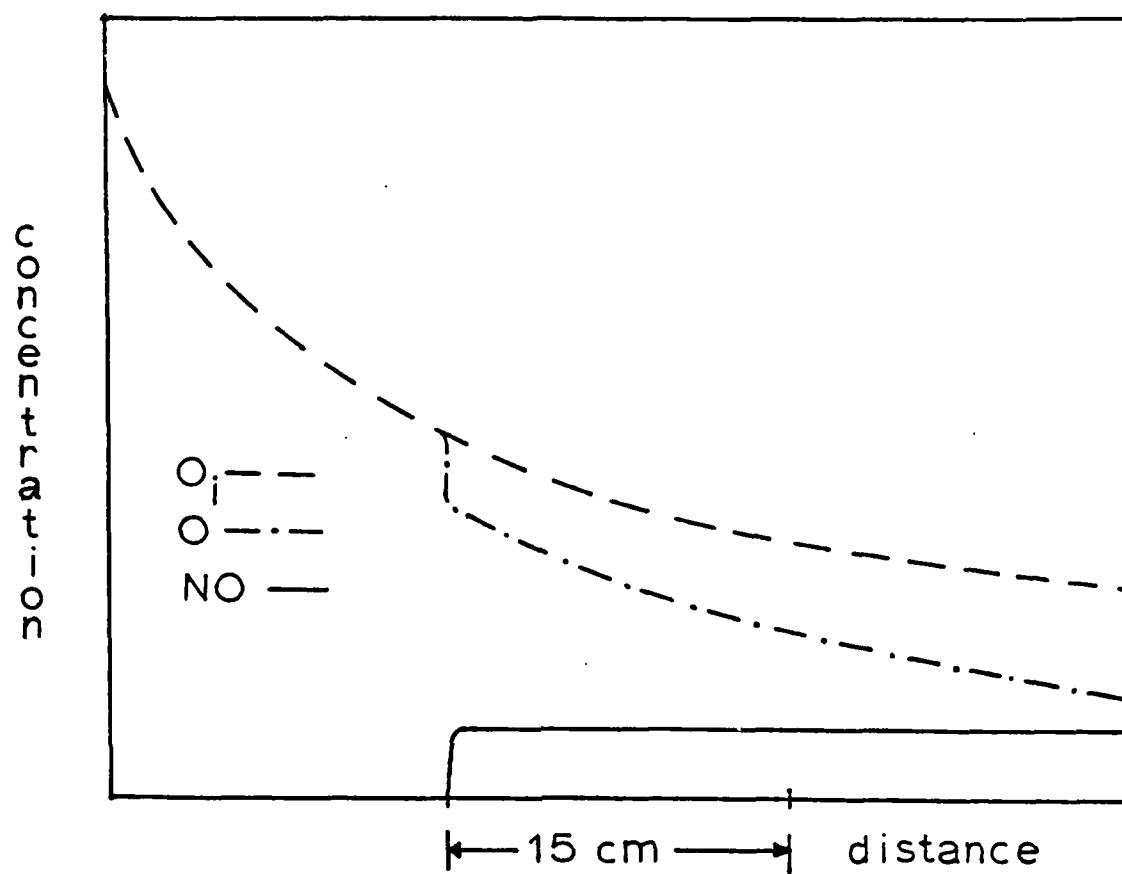
Fig. 14 Experimental apparatus used to calibrate the detectors.

Figure 15 illustrates concentration changes during operation of this system. A computer simulation of the atomic oxygen decay was performed and compared to experimental results to obtain this graph. Once the  $\text{NO}_2$  was injected, it was converted directly into NO and the atomic oxygen density was quenched abruptly as it was consumed by the  $\text{NO}_2 + \text{O}$  reaction. Using the computer model to estimate this jump, it was possible to predict the atomic oxygen and NO concentrations 15 cm downstream of the  $\text{NO}_2$  injector. These results were then used in Eq. (3) to obtain  $K_{\text{DET}}$  and listed in Table 1. These data have been reproduced under several different oxygen pressures.

### 3. Transport Measurements

To minimize the effects the radiation has on the detectors used it was apparent that the transport studies can only be completed at low steady state reactor power levels. However, at reactor powers of 1 MW or less, the  $\text{O}_2(^1\Delta)$  concentration was considerably less than what was obtained from a pulse. Consequently, a nuclear radiation sustained discharge (Figure 16) was constructed to enable steady state production of the  $\text{O}_2(^1\Delta)$  densities observed during a pulse. By utilizing the nuclear reactor as an external ionization source  $\text{O}_2(^1\Delta)$  densities of up to 1.4 mTorr in 1 Torr of  $\text{O}_2$  were generated. Since, the radiation levels were much lower during these experiments, the detectors could be moved along the flow path to obtain the decay rate of the  $\text{O}_2(^1\Delta)$ . By matching  $\text{O}_2(^1\Delta)$  and  $\text{O}_3$  yields from this system with the concentrations typical of the direct nuclear pumped approach, it was possible to determine the  $\text{O}_2(^1\Delta)$  decay rate for the conditions observed in an Ar- $\text{O}_2$  nuclear pumped system.

The results of the transport study are shown in Figure 17. For the mixture of 150 Torr Ar, 2 Torr  $\text{O}_2$  and 1 millitorr  $\text{O}_3$ , the  $\text{O}_2(^1\Delta)$  lifetime was found to be approximately 0.3 seconds. The lifetime does not



15. Computer simulation of reactions occurring after mixing  $NO_2$  with an atomic oxygen stream.

Table 1

Detector Calibration Constants Obtained  
with NO<sub>2</sub> Titration Experiments

ADC MODEL 403 @ 1.27 m	$[O_2(^1\Delta)] - (1.5 \pm .5) \times 10^{10} \left( \frac{\text{molecules}}{\text{cm}^3 \cdot \text{mV}} \right)$
RCA 31034 @ 1.8kV @ 6340A	$[O_2(^1\Delta)] - (7.8 \pm .5) \times 10^{10} \left( \frac{\text{molecules}}{\text{cm}^3 \cdot \text{mV}^{1/2}} \right)$

Table 2

O<sub>2</sub>(<sup>1</sup>Δ) Yields from a Direct Nuclear-Pumped  
Noble Gas - O<sub>2</sub> Mixture

150 Torr-Ne, 2 Torr-O <sub>2</sub>	0.18 mTorr	O <sub>2</sub> ( <sup>1</sup> Δ)
150 Torr-Ar, 2 Torr-O <sub>2</sub>	0.15 mTorr	O <sub>2</sub> ( <sup>1</sup> Δ)
150 Torr-He, 2 Torr-O <sub>2</sub>	0.14 mTorr	O <sub>2</sub> ( <sup>1</sup> Δ)

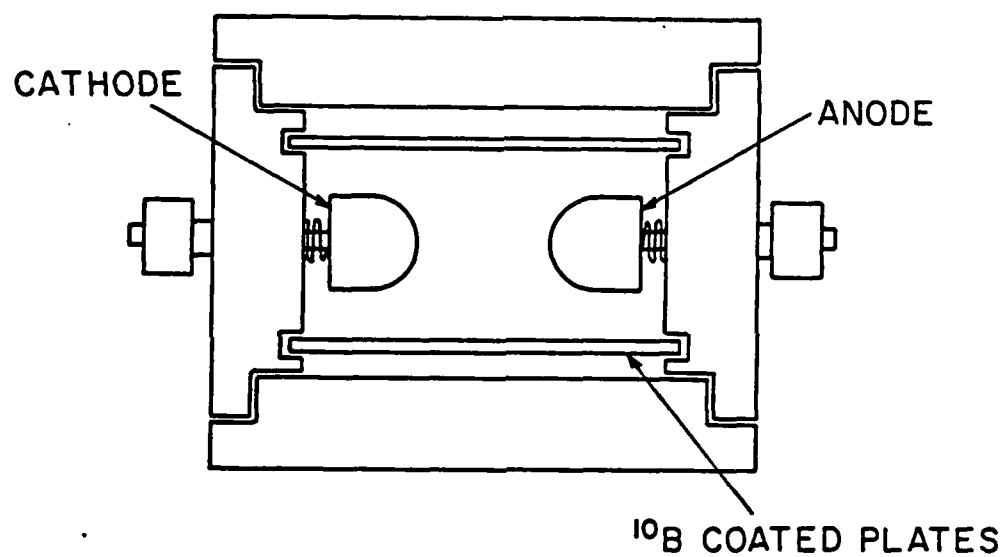
FSL-82-177

Fig. 16 Hybrid Nuclear/Electrical Discharge apparatus  
A  $^{10}\text{B}$  coating was placed on an aluminum  
plate and suspended by the Plexiglas walls.



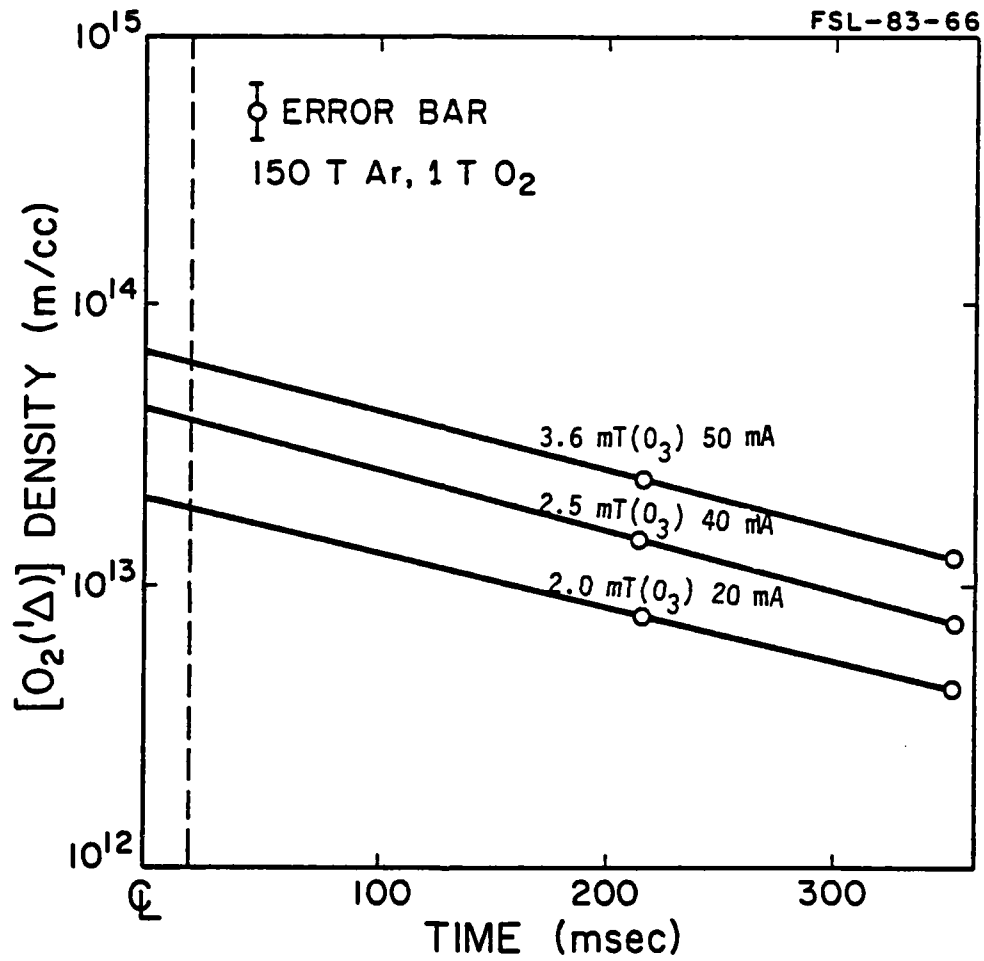


Fig. 17 Decay of O<sub>2</sub>(<sup>1</sup>Δ) for conditions similar to direct nuclear pumping.

vary significantly for the three cases shown because the dimole reaction,  $O_2(^1\Delta) + O_2(^1\Delta) \rightarrow O_2(^1\Delta) + O_2$ , was not important at the low  $O_2(^1\Delta)$  concentrations involved.

Figure 18 shows the measured spread of the excited gas slug as it passed the detectors. A gaussian shaped slug, approximately two-feet long was expected. But as seen in these diagrams, for the case of helium the excited gas slug was considerably broader than the initial dimensions of the Boron-10 coated aluminum tubes inside the reaction zone. Similar results were observed in Argon and Neon but the magnitude of the spreading was less pronounced. The differences appear to be largely associated with variations in gas viscosity. After correction for this expansion,  $O_2(^1\Delta)$  measurements indicated the neon oxygen mixtures produced the highest yield. These yields are shown in Figure 19 (also see Table 2) where the neon-oxygen mixtures produced 0.18 millitorr of  $O_2(^1\Delta)$ , the argon-oxygen mixtures yielded 0.15 millitorr  $O_2(^1\Delta)$ , and the helium-oxygen system peaked at 0.14 millitorr of  $O_2(^1\Delta)$ . These results were obtained with a pressure of 150 Torr noble gas and 2 Torr oxygen.

#### 4. Parametric Studies

The  $O_2(^1\Delta)$  yields were observed to increase with the buffer gas pressure and with increased neutron flux. However, as stressed earlier, at high buffer gas pressures, ozone production is favored. Figure 20 shows the scaling of the  $O_2(^1\Delta)$  yields with buffer gas pressure. Notice that in argon the yields appear to saturate at approximately 100 Torr which suggests the alpha particles have reached their maximum range for this pressure. In the case of neon-oxygen, the saturation begins at a considerably higher pressure (around 250 Torr). This is to be expected since the range of alpha particles in neon is larger than in argon.

The UV absorption diagnostic allowed the ozone yields to be monitored directly. The yields were observed to increase with  $O_2$  pressure, thermal

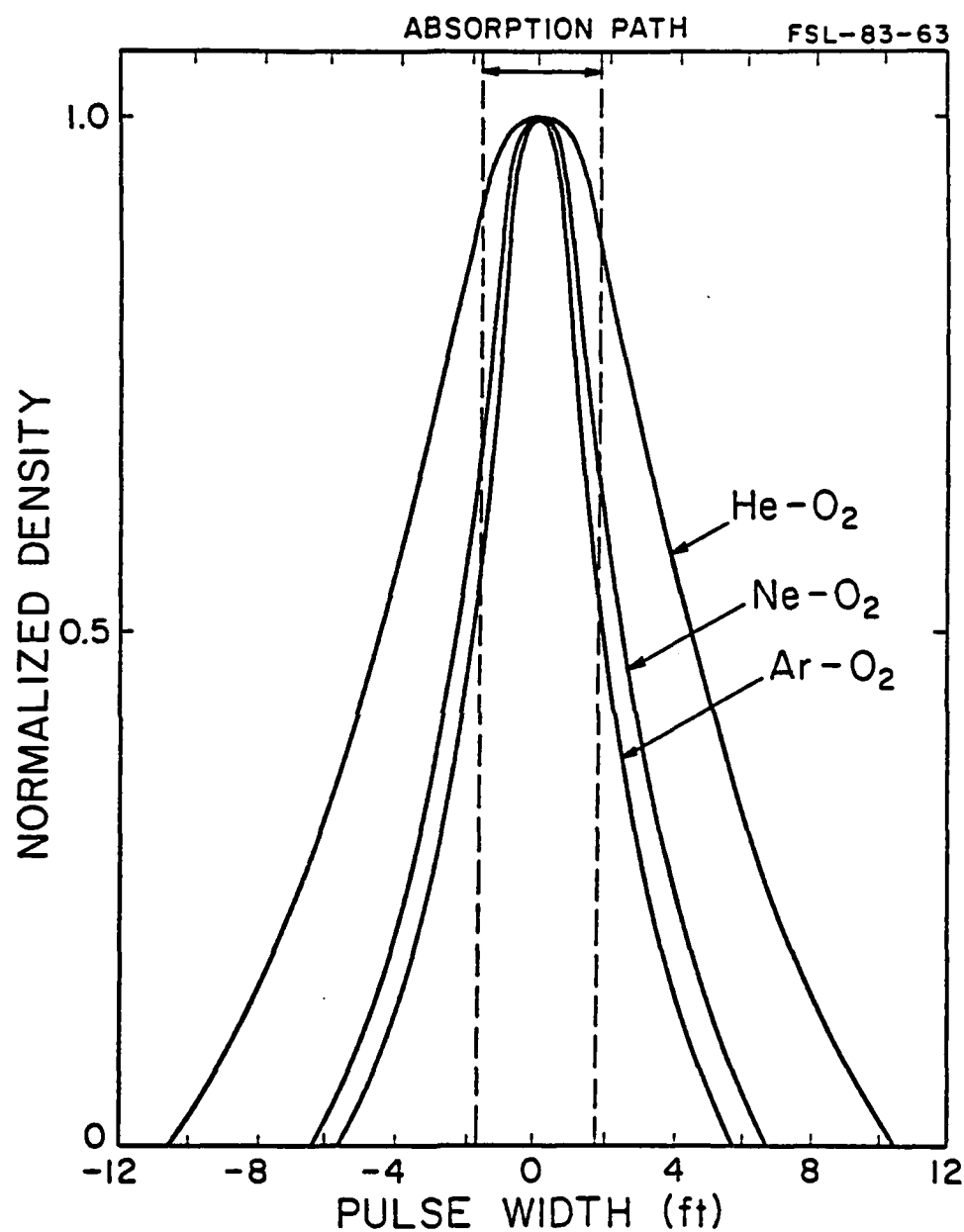


Fig. 18 A comparison between the spread out excited gas slug and the absorption path used to monitor  $O_3$ . The expansion factors were, He:3.2x, Ne:1.5x, Ar:1.2x.

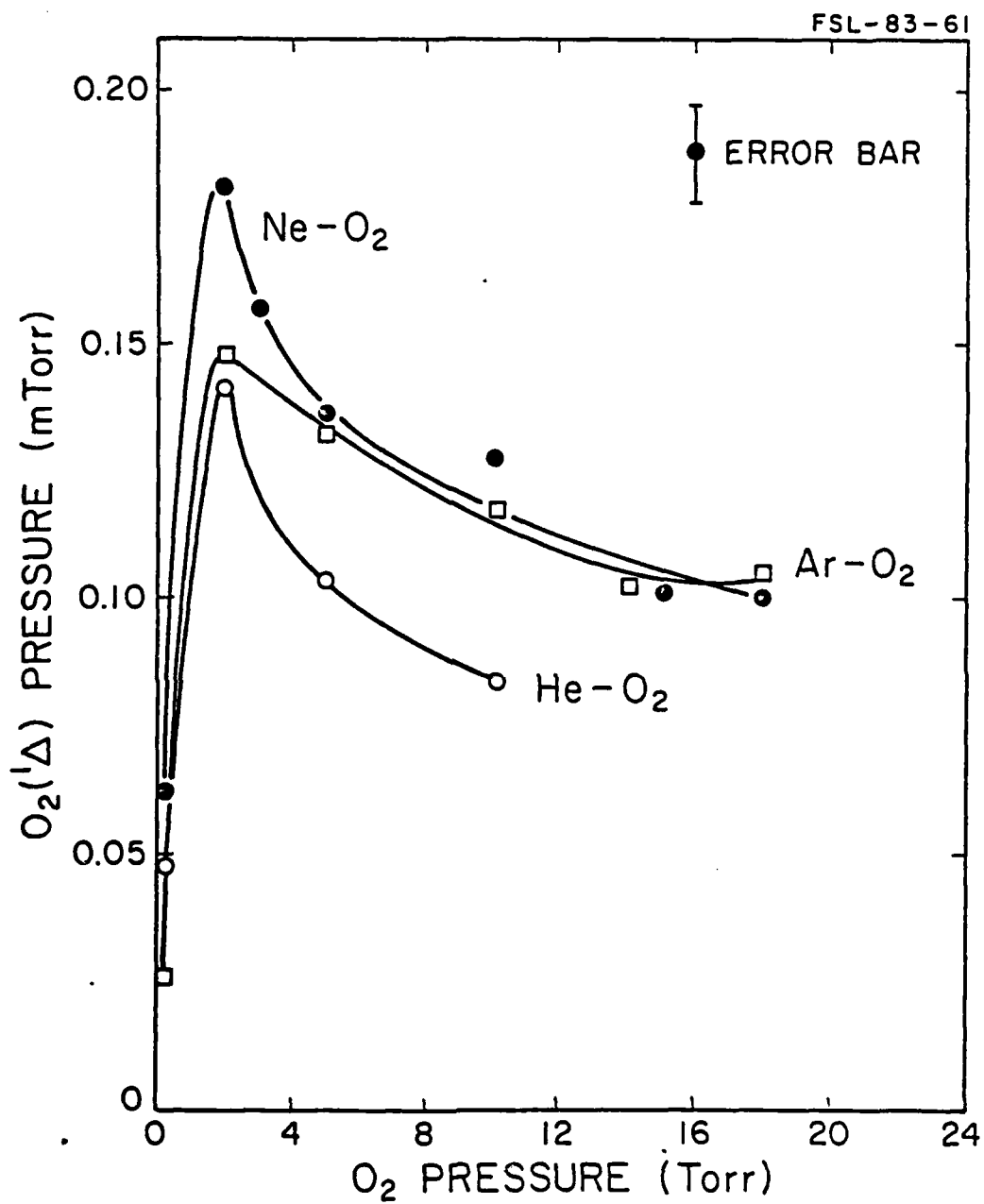


Fig. 19  $O_2(^1\Delta)$  yields in various noble gas buffers (150 Torr) as a function of  $O_2$  pressure.

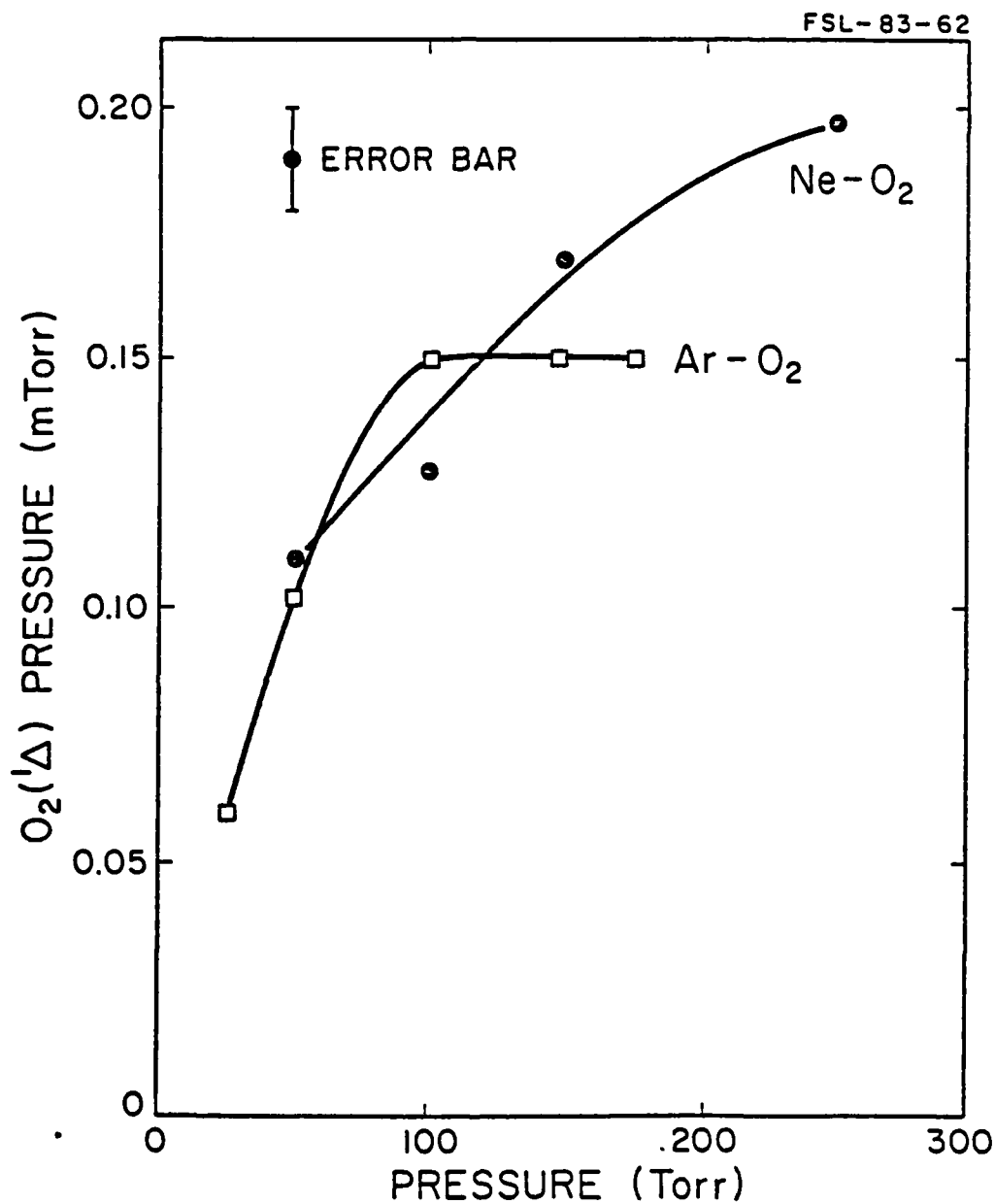


Fig. 20 Scaling of  $O_2(^1\Delta)$  yields with increasing buffer gas pressure. He-O<sub>2</sub> mixtures are not graphed due to the low  $O_2(^1\Delta)$  yields obtained.

neutron flux, and noble gas pressure. The net result of this study is that helium was found to be the best buffer gas for producing ozone under the present conditions. The dissociative resonant energy transfer:  $\text{He}_2^+ + \text{O}_2 \rightarrow \text{O} + \text{D}^+ + 2\text{He}$  is apparently responsible for the efficient formation of atomic oxygen in the discharge. At these high pressures the atomic oxygen is rapidly converted into ozone by three body recombination.

Figure 21 shows the uncorrected yields for ozone as a function of increasing  $\text{O}_2$  pressure. The apparent decrease in ozone yields for different noble gases was merely a result of the differences in spreading of the excited gas slug as it was transported 6 meters to the detectors. Upon correcting for this expansion (Figure 22), the helium oxygen mixture is found to have the highest yields. The scaling of the ozone yield with noble gas pressure is diagrammed in Figure 23. The yields in the  $\text{He-O}_2$  mixture increased at a faster rate than in  $\text{Ne-O}_2$ , which in turn increased at a faster rate than in the  $\text{Ar-O}_2$ . This is probably due to the more efficient dissociative resonant energy transfer in helium which results in the efficient formation of atomic oxygen.

##### 5. In-Core Fiber Optic Diagnostic

The in-core diagnostic system which was developed in this project employed a silica lens system to couple an observation cell with a fiber optic bundle (Figure 24). The silica lens system was necessary to locate the fiber optic bundle outside of the extremely intense radiation field which occurs close to the reactor core. The silica lenses were chosen to take advantage of their high resistance to radiation damage. The first series of measurements were made with a high purity silica fiberoptic bundle which had an attenuation of 20,000 dB per kilometer at 1.27 microns. Consequently, it was not possible to observe emissions from  $\text{O}_2(^1\Delta)$  at 1.27 microns. Since the attenuation was much less in the visible regime

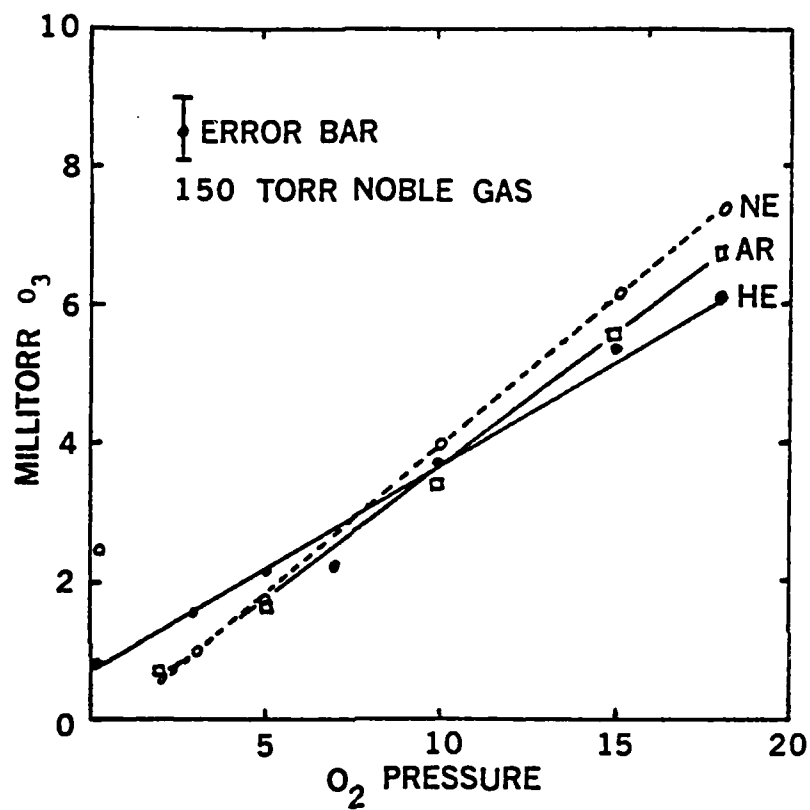


Fig. 21  $O_3$  yields as a function of increasing  $O_2$  pressure but uncorrected for the expansion observed in Fig. 18.

FSL-83-64

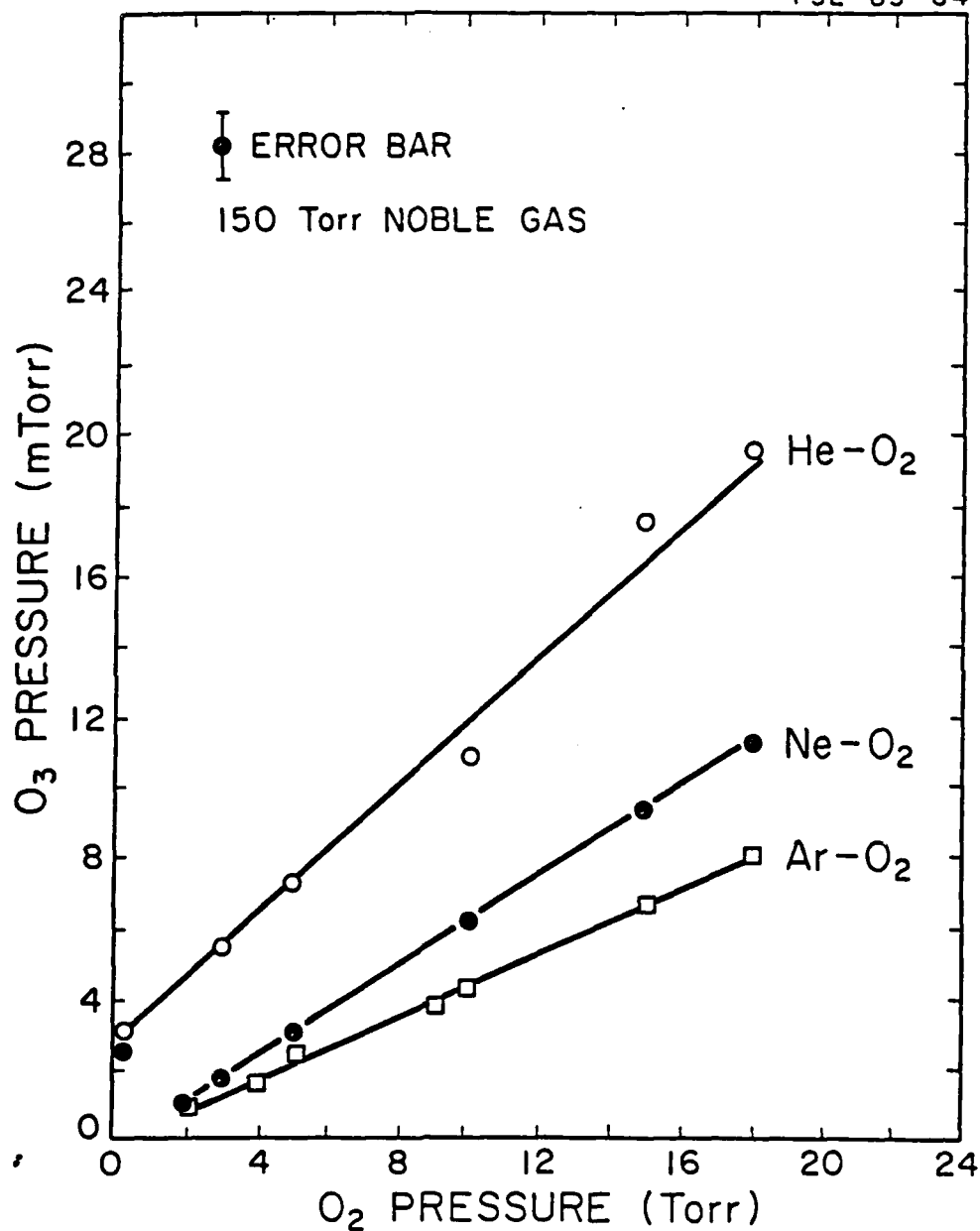


Fig. 22 O<sub>3</sub> yields from a \$3.00 pulse in 150 Torr of a Noble gas after correcting for the expansion diagrammed in Figure 17.



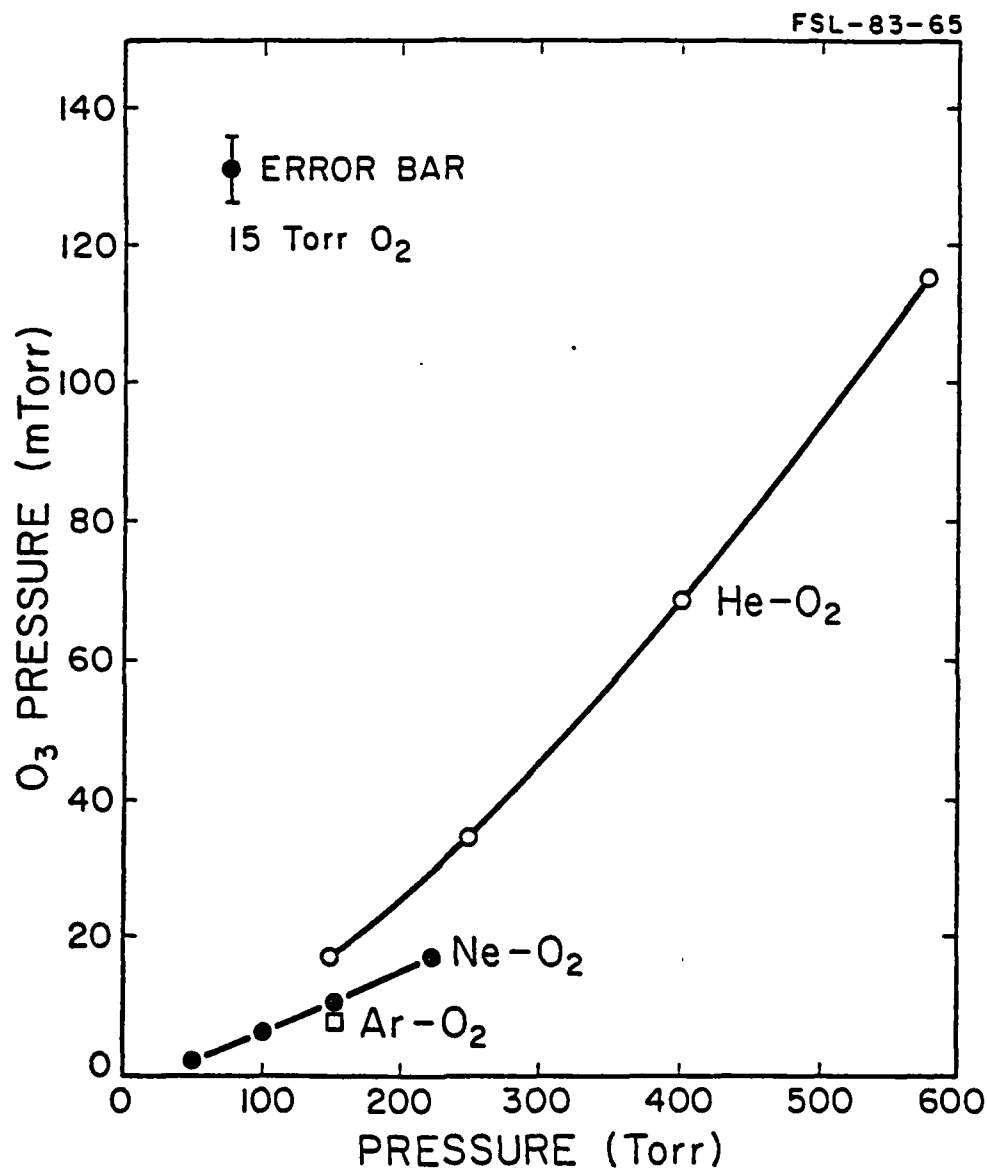


Fig. 23 Scaling of O<sub>3</sub> yield with increasing Noble gas pressure for a \$3.00 TRIGA pulse. These results are also corrected for the expansion depicted in figure 17.

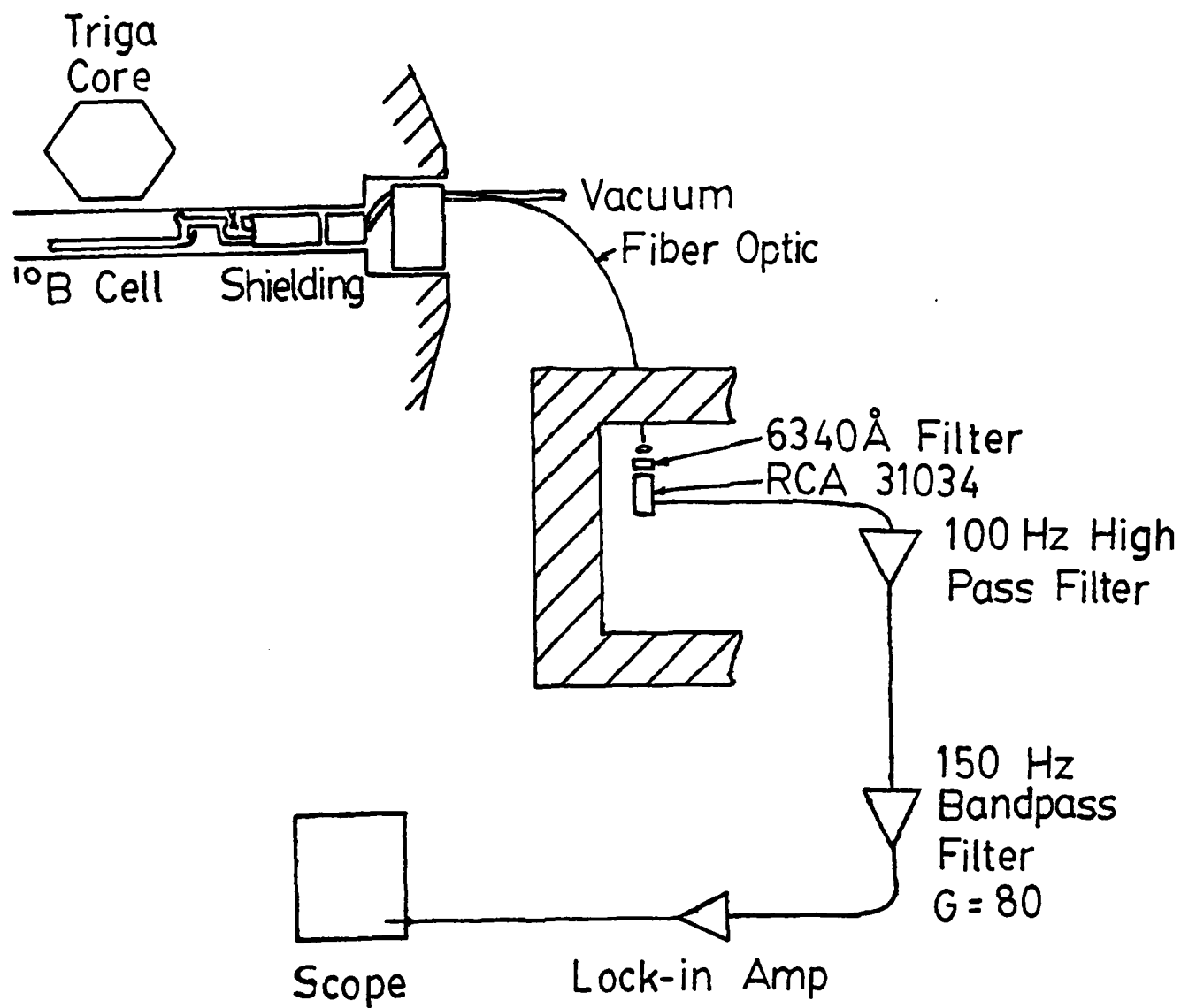


Fig. 24 In-core diagnostics used to monitor emissions from  $\text{O}_2(^1\Delta)$  near the reactor core. The observation cell was located between the B-10 cell and the shielding, while the silica lens system was embedded in the shielding.

(20dB/km), measurements were possible at  $6340 \text{ \AA}$  but this required electronic filters to suppress the fluorescence from the Cerenkov emissions generated in the lens-fiberoptic system. However, the emissions observed in the observation cell were of insufficient intensity to produce consistently reliable results at  $6340 \text{ \AA}$ . To overcome this problem an anhydrous silica bundle, which has an attenuation at 1.27 microns of only 20 db per kilometer, was ordered. This would have allowed operation on the higher intensity 1.27 microns emission, however there was insufficient time to perform the measurements before the termination of this contract.

The incore apparatus also employed a flowing afterglow design (Figure 24). With this design, observation of the afterglow occurs only 30 cm from the radiation zone vs. 6 meters in earlier designs. The observation cell was isolated from the discharge chamber by a pair of light traps and the light transport tube (using a series of silica lenses) was embedded in borated polyethelene to reduce the radiation interacting with the system. A small chopping fan was used at the entrance to the light transport tube, i.e. between the tube and the observation cell. The signal exiting the lens fiber optic system consisted of a component with the chopping frequency and a slowly varying emission which followed the neutron pulse ( $\omega \sim 100 \text{ Hz}$ ). Therefore, the low frequency component of the signal was eliminated with a 100 Hz high-pass electronic filter. A 150 Hz band pass filter was then used to eliminate the high frequency noise. The signal with the chopper frequency was finally reconverted to a DC level with a lock-in amplifier (PAR H-8). The processed signals were then displayed on the Tektronix scope and the results were recorded with a Polaroid camera.

## 6. Kinetic Models

Modeling of the argon and oxygen nuclear pump system has advanced quite significantly since the beginning of this project. A more detailed

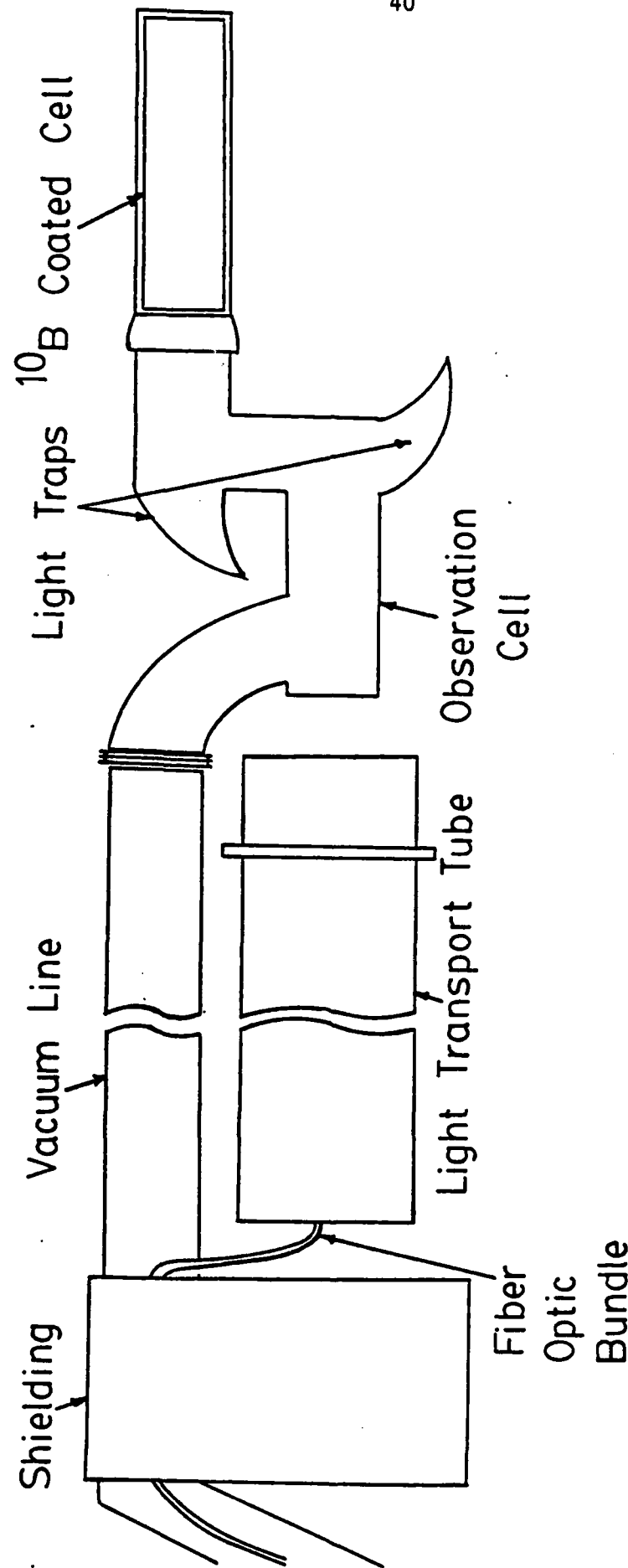


Figure 24 In core apparatus designed to monitor  $O_2(\Delta)$  emissions within 1' of the excitation region. The Light Transport Tube allowed relocation of the fiber bundle outside of the intense radiation zone.

description of the kinetic model and some of the calculations performed with it are presented in Appendix B. Calculations with the model exhibited the same dependences with increasing noble gas and  $O_2$  pressures as have been observed experimentally (see Figure 25). One of the more significant points in the modeling is that the results indicate that the  $O_2(^1\Delta)$  yields will increase with noble gas pressure and thermal neutron flux.

As the  $O_3$  yields begin to increase with the noble gas pressure and power deposition, the  $O_2(^1\Delta)$  lifetime will decrease. This is expected since ozone and  $O_2(^1\Delta)$  mutually quench each other in the afterglow. Figure 25 shows a comparison between the modeling and the experiments with increasing noble gas pressure. Relatively good agreement is generally observed. However, at the higher argon pressures, the ozone concentration is somewhat overestimated by the model. This may be because of a power saturation term and the effect of oxidation of the walls have not been included. (These effects are now being added to the model.) The results of the modeling at the peak of the pulse are important since they indicate the  $O_2(^1\Delta)$  concentration will increase with argon pressure but its lifetime will become shorter. Therefore, less  $O_2(^1\Delta)$  will be observed downstream.

## 7. Nuclear Sustained Electrical Discharge

The nuclear sustained discharge was constructed to perform the transport measurements. Throughout these experiments this system's operation had to be characterized to insure that the conditions present in a direct nuclear-pumped system could be simulated. The apparatus used was shown earlier in Figure 16. It was constructed out of a plexiglas box in which two Boron-10 coated aluminum plates were supported transverse to a pair of 1/2-inch diameter electrodes by the outer walls of the Plexiglas cell. In operation the discharge was observed to be unaffected by the Boron 10

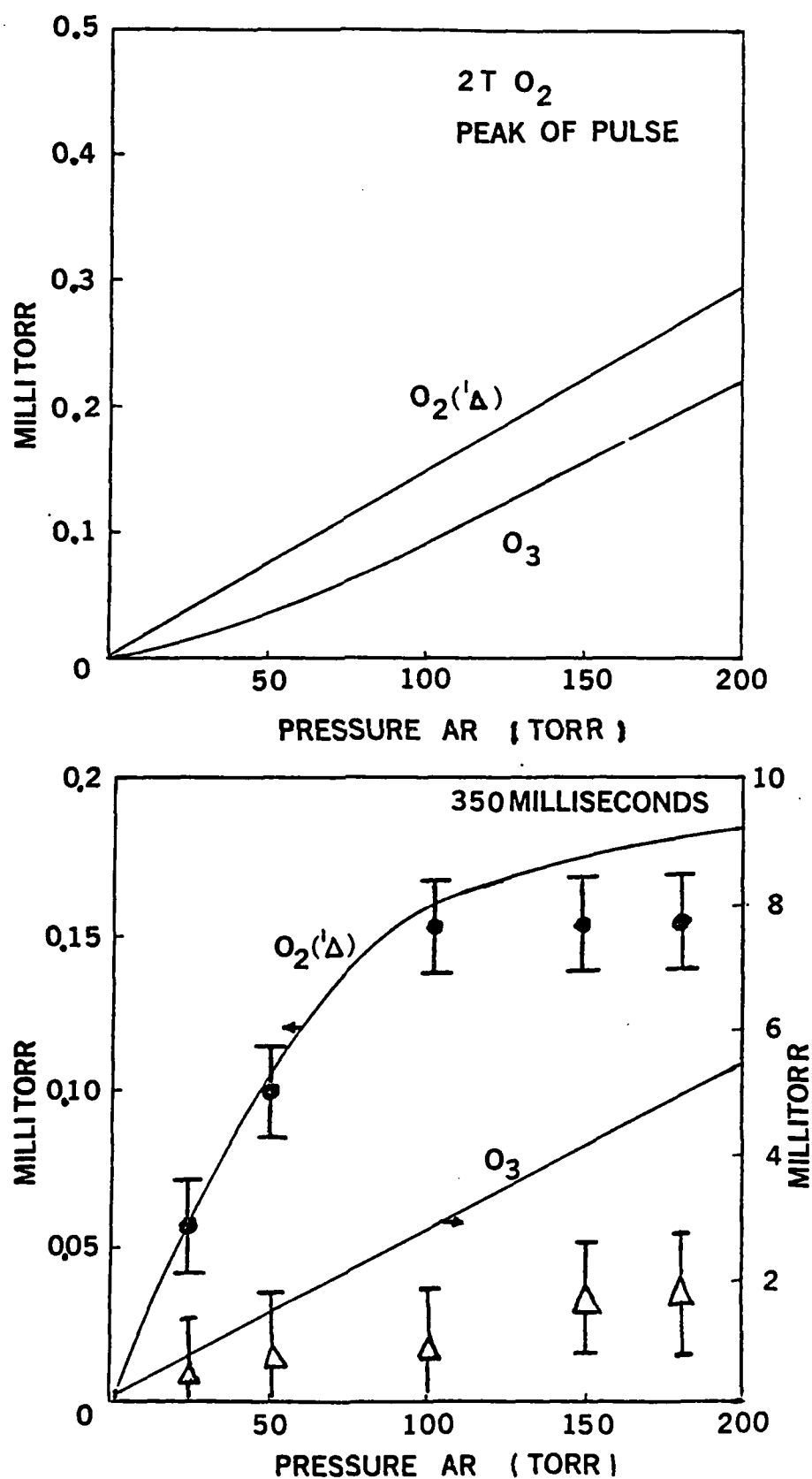


Fig. 25 The lower graph shows a comparison between the modeling and the experimental results. The upper graph illustrates the equivalent behavior at the peak of the pulse.

plates which are isolated from both the anode and the cathode by the Plexiglas walls. At moderate reactor power levels (<1 MW) a relatively stable discharge was obtained which could operate at low electric fields (Figure 26). We have observed up to 1.4 millitorr of  $O_2(^1\Delta)$  in 1 Torr  $O_2$  and 100-Torr Ar with a modest electrical power deposition. Figure 27 demonstrates how scaling to higher yields is indeed possible with lower gas pressures and higher electrical power input. This graph shows that the  $O_2(^1\Delta)$  concentrations increase relatively rapidly with respect to the square root of electrical power deposited in the system. If the curves for 150 Torr argon are compared to 100 Torr argon, the slope of the  $O_2(^1\Delta)$  yield does not change. However, the power level required to generate a given  $O_2(^1\Delta)$  yield is reduced. In addition, the  $O_3$  yields were observed to decrease with an increase of the electrical power input (Figure 28). This effect is probably a result of the  $O_2(^1\Delta)$  becoming the dominant species in the afterglow (rather than a decrease in the ozone production). This increased ozone deactivation rate in the afterglow causes the decrease in the ozone yields at the detector set up.

#### 8. Conclusions

In conclusion, we have found that direct nuclear pumping favors the production of ozone. In addition the  $O_2(^1\Delta)$  yield scales with the noble gas pressure but the ozone yield scales much faster for a given power input. Thus, we have identified the photolysis of ozone into  $O_2(^1\Delta)$  as a very promising approach for the efficient production of large  $O_2(^1\Delta)$  yields.  $O_2(^1\Delta)$  pressures of up to 10 Torr could be generated and the ozone yields necessary for this scheme have indeed been observed experimentally.

The nuclear sustained electrical discharge generated  $O_2(^1\Delta)$  yields which scaled according to the square root of the power. No saturation was

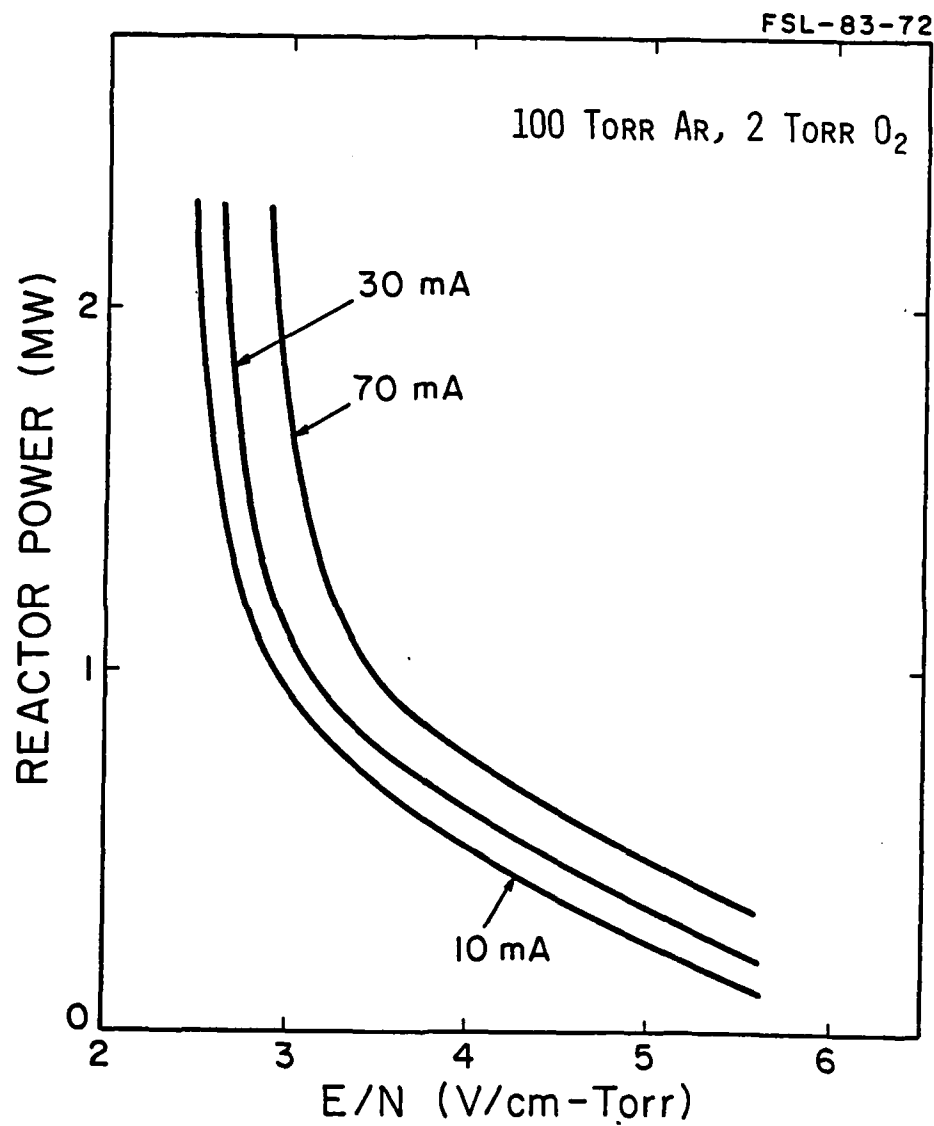


Fig. 26 Operational characteristics of a nuclear sustained discharge for an Ar-O<sub>2</sub> mixture.



FSL-83-69

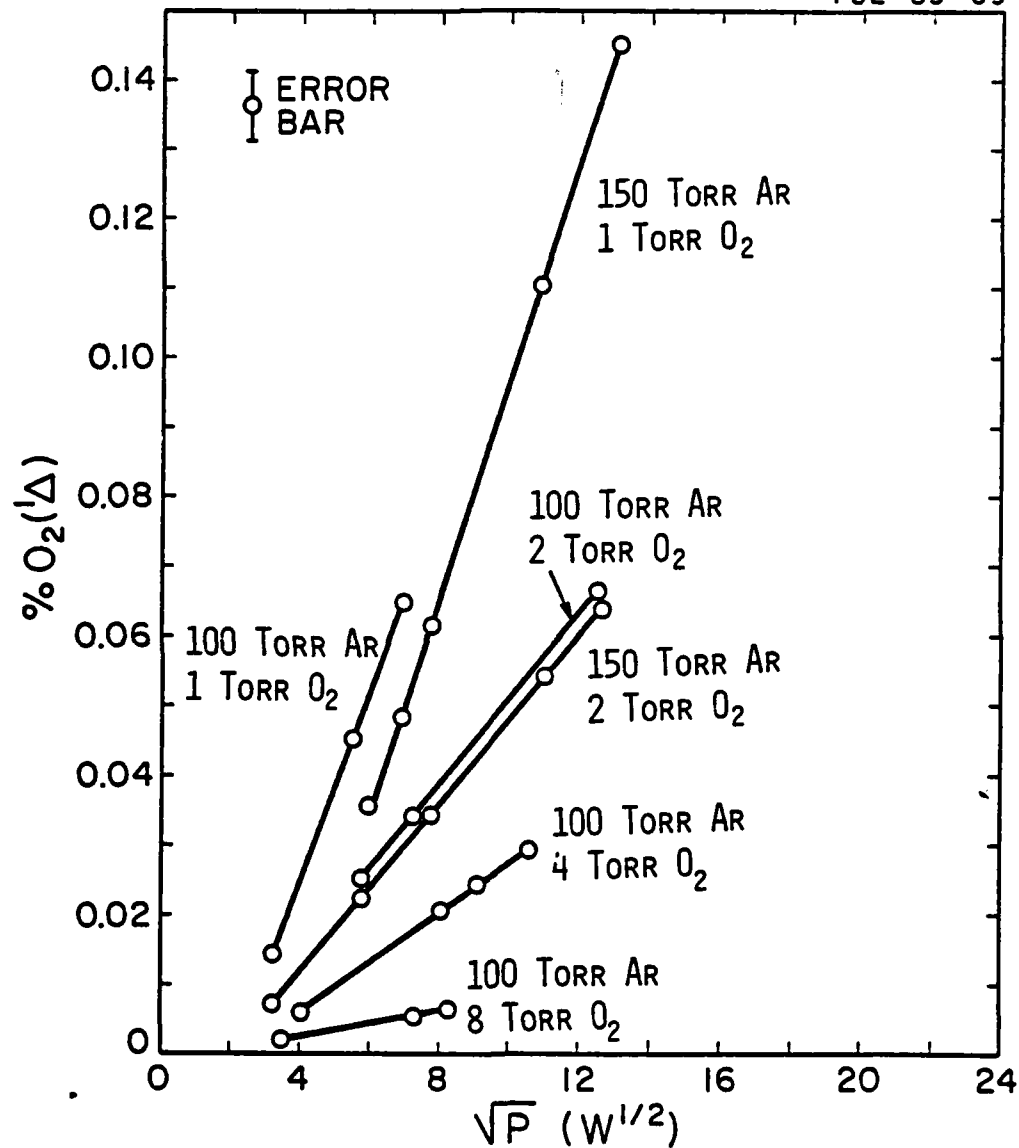


Fig. 27 Scaling of  $O_2(^1\Delta)$  yields with the square root of the power (recombination dominant plasma) and buffer gas pressure.

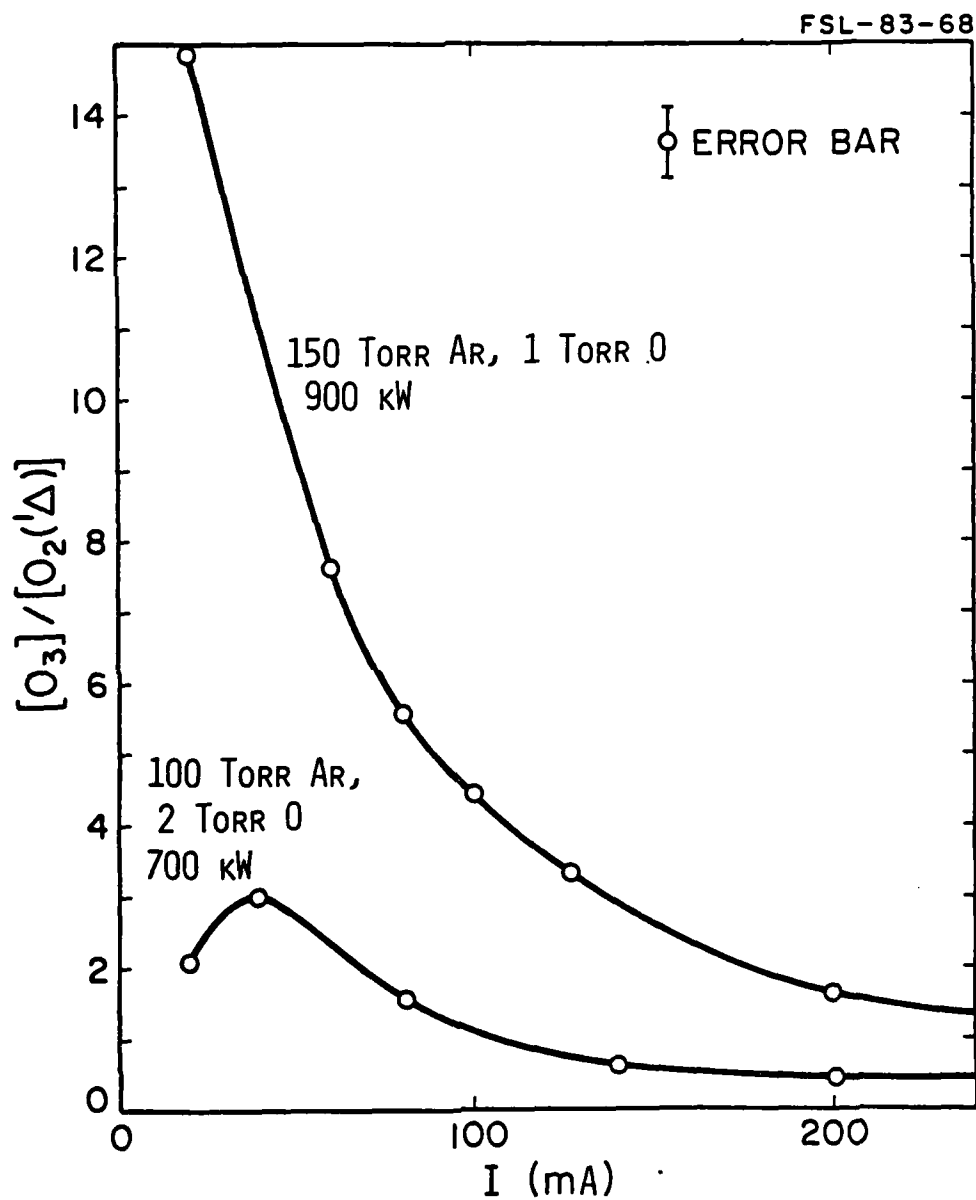


Fig. 28 Decrease in  $O_3/O_2(^1\Delta)$  ratio observed as a function of input current. This graph demonstrates how the low E/N discharge favors the production of  $O_2(^1\Delta)$ .

observed up to the limit of the power supply used which resulted in an  $O_2(^1\Delta)$  concentration of 1.4 mTorr in 1 Torr of  $O_2$ . In addition, despite an increase in power input only  $O_2(^1\Delta)$  was observed to increase substantially,  $O_3$  yields varied only slightly. Finally, the diagnostics developed for this work made the very sensitive concentration measurements possible despite the adverse conditions caused by extraneous radiation from the reactor.

#### Acknowledgements

This research was supported by contract DOE - DE-AS08-82DP40173 made possible through a grant from the office of the chief scientist, Dr. Arthur Guenther, at the Air Force Weapons Laboratory. Important technical contributions by the Technical monitor, Lt. D. Bury, as well as helpful discussions with Capt. R. Bjurstrom and Capt. J. Taylor are gratefully acknowledged.

In addition to Prof. G. H. Miley who served as principal investigator on this project, M. Zediker, H. Elsayed-Ali, and D. Shannon performed many of the experiments and calculations as research assistants in the Nuclear Engineering Program at the University of Illinois. Helpful discussions with C. Choi are also gratefully acknowledged.

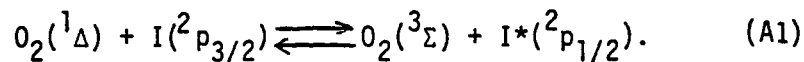
## Appendix A.

KINETIC MODEL OF PHOTOLYTIC  $O_2(^1\Delta)$  GENERATION

ABSTRACT: Kinetic analysis of photolysis of  $O_3:O_2:He$  mixtures by UV light has been studied. Dependence of  $O_2(^1\Delta)$  yield on partial pressures, flash-lamp intensity and duration was investigated. Results indicate sufficient  $O_2(^1\Delta)$  yield for operation of a high-power atomic iodine laser at the  $I^*(^2p_{1/2}) \xrightarrow{1.31\mu m} I(^2p_{3/2})$  transition.

## I. Introduction

Operation of an atomic iodine transfer laser at the  $I^*(^2p_{1/2}) \xrightarrow{1.31\mu m} I(^2p_{3/2})$  spin-orbit transition is well demonstrated and represents an important high-power laser, (Refs. A1-A3). In this laser, excited molecular oxygen,  $O_2(^1\Delta)$ , is generated chemically and then transferred to a laser cell where it is mixed with  $I_2$ . This results in the dissociation of  $I_2$  and the subsequent formation of  $I^*(^2p_{1/2})$  by the fast near resonant energy transfer reaction:



The equilibrium constant for this reaction is 2.9 at 300°K. Therefore, in order to achieve a population inversion, it is necessary that the  $\frac{[O_2(^1\Delta)]}{[O_2(^3\Sigma)]}$  ratio

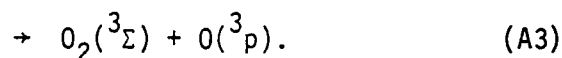
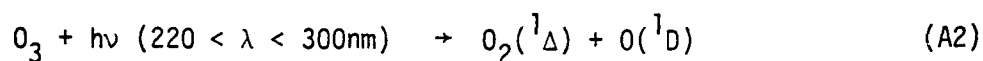
be greater than .17 at room temperature (Ref. A2).

The idea of achieving a population inversion on the atomic iodine  $I(^2p_{1/2}) \rightarrow I(^2p_{3/2})$  transition by near resonant energy transfer from  $O_2(^1\Delta)$  was proposed several years ago (Ref. A4). The lack of an  $O_2(^1\Delta)$  generator capable of delivering a sufficient yield prevented the rapid development of this idea. The first successful operation of an  $O_2(^1\Delta)$ - $I_2$  transfer laser used a chemical source for the generation of  $O_2(^1\Delta)$  (Ref. A1). In this laser  $O_2(^1\Delta)$  was produced by reaction of chlorine with basic hydrogen peroxide. About 1 Torr  $O_2$  was produced with an  $O_2(^1\Delta)$  yield greater than 40%.

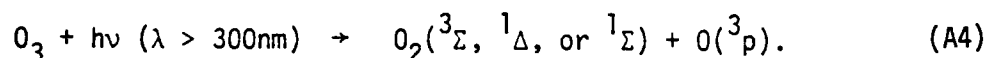
Although operation of the chemical  $O_2(^1\Delta)$ - $I_2$  laser is well demonstrated and has proven high power capabilities, the chemical generation of  $O_2(^1\Delta)$  suffers from a great deal of shortcomings. This includes the inability to generate high  $O_2(^1\Delta)$  density, the need for cooling, and the use of corrosive materials. Investigation of other possible sources of  $O_2(^1\Delta)$  includes electron beam sustained discharges (Ref. A5), microwave discharges (Ref. A6), direct nuclear pumping (Ref. A7) and photolytic decomposition of ozone (Ref. A8). Recently the authors described the prospects of utilizing nuclear energy to simultaneously produce ozone while providing energy to a KrF nuclear pumped flashlamp ( $\lambda = 249$  nm) for decomposing the nuclear-produced ozone into  $O_2(^1\Delta)$  (Ref. A9). This paper describes the physical process involved in  $O_2(^1\Delta)$  production by photolysis of  $O_3:O_2:He$  mixtures.

## II. Kinetic Model

In the photolysis of ozone (220-300 nm Hartley band) the main dissociation channels are (Ref. A10):



The quantum efficiency for channel A2 is determined to be approximately 90% with the relative quantum yield for reactions A2 and A3 being constant in the range 250 to 300 nm (Ref. A10). For  $\lambda > 310$  nm the primary photodissociation channel is (Ref. A11):



However, the photoabsorption cross section of ozone in this range is much lower than for  $\lambda < 300\text{nm}$  (Fig. 1).

The rate of photodissociation of ozone by UV light extending from  $\lambda_1$  to  $\lambda_2$  is given by

$$W = C \int_{\lambda_1}^{\lambda_2} n(\lambda) \sigma(\lambda) d\lambda \quad (\text{A5})$$

where  $C$  is the speed of light

$n(\lambda)$  is the density of photons with wavelength  $\lambda$ , and

$\sigma(\lambda)$  is the ozone photoabsorption cross section at  $\lambda$ .

For narrow-band UV light, as in the case of a rare gas halide excimer flashlamp (typical bandwidth =  $20\text{\AA}$ ), a good approximation of  $W$  is given by

$$W = C \sigma(\lambda_0) n \quad (\text{A6})$$

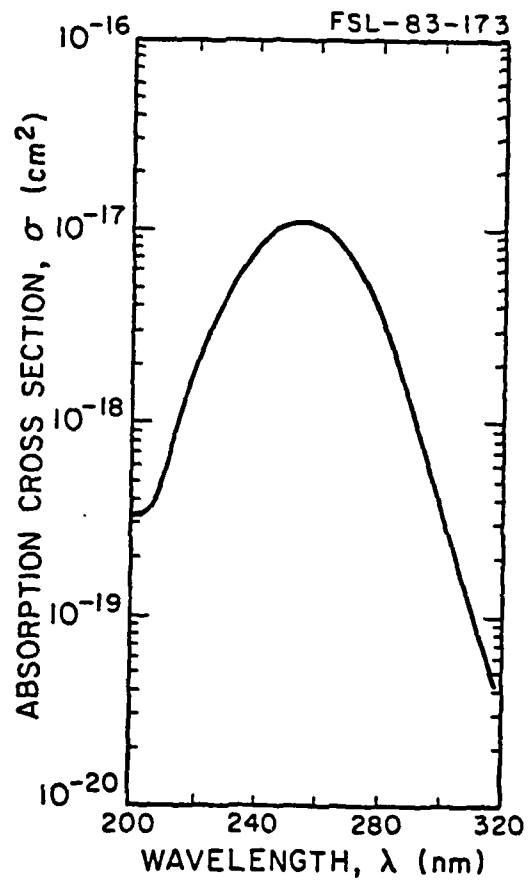


Fig. A1. Absorption spectrum of  $\text{O}_3$  in the Hartley band (Ref. A12)

where  $\sigma(\lambda_0)$  is the absorption cross section of ozone at the central wavelength of the excimer fluorescence band, and  $n$  is the photon density in the fluorescence band.

Some characteristics of several excimer flashlamps that can be utilized for  $O_2(^1\Delta)$  generation are listed in Table I.

Table A1  
Some Properties of Excimer Flashlamps (Refs. A12, A13)

System	Wavelength, $\lambda_0$ [nm]	Maximum Radiative Efficiency [%]	Ozone Absorption Cross Section at $\lambda_0$ , $\sigma$ [Mb]
XeI*	253	37.2	11.4
KrF*	249	34.0	11.1
XeBr*	282	29.1	3.4
ArF*	284	22.4	2.4

The use of a standard xenon flashlamp for the photolysis of ozone is also possible at a reduced efficiency since the flashlamp output in the 220-300 nm band is typically less than 10% for a 1 ms pulse and decreases with an increase in the flashlamp duration (Ref. A14). Although UV light above 310 nm will dissociate ozone mainly into  $O_2(^3\Sigma)$ , the low photoabsorption cross section of ozone in this region limits this process.

In this analysis a KrF\* flashlamp is considered as the UV source. Such a flashlamp has a proven efficiency higher than 10% for an electrical discharge and electron beam pumping (Ref. A15), and an estimated



efficiency of 14.25% for direct nuclear pumping (Ref. A13). If all of the flashlamp output is at the central wavelength ( $\lambda = 249$  nm), then the photon density in the absorption cell is given by:

$$n = 3.79 \times 10^7 I \quad \text{cm}^{-3} \quad (\text{A7})$$

where  $I$  is the output flashlamp intensity in  $\text{W/cm}^2$ .

Therefore, the rate of ozone dissociation is given by

$$W = 13.88 I \quad \text{sec}^{-1}. \quad (\text{A8})$$

Since the quantum yield of reaction (1a) is 90%, the rate of ozone dissociation through channels (1a) and (1b) is given by:

$$W_{1a} = 12.49 I \quad \text{sec}^{-1} \quad (\text{A9})$$

$$W_{1b} = 1.39 I \quad \text{sec}^{-1} \quad (\text{A10})$$

The reactions considered in the model are listed in Table II. Most of the rate coefficients considered in this model are the preferred values suggested in Reference A12. Generation of  $\text{O}_2(^1\Delta)$  by collisional deactivation of  $\text{O}_2(^1\Sigma)$  by ozone was neglected since the branching ratio between reactions (7b) and (7c) are unknown. As the concentration of  $\text{O}_2(^1\Sigma)$  is low, inclusion of reaction (7c) will only cause a slight increase in the produced  $\text{O}_2(^1\Delta)$ . Reaction 17b was determined to proceed  $\geq 3$  times faster than reaction 17c; therefore, energy transfer from  $\text{O}(^1\text{D})$  to ground state molecular oxygen,  $\text{O}_2(^3\Sigma)$ , generating  $\text{O}_2(^1\Delta)$  was neglected in this model.

Table A2  
Photolytic Generation of  $O_2(^1\Delta)$  Model

Reaction No.	Reaction	Rate Coefficient <sup>a</sup>	Reference
Photodecomposition of ozone:			
1a	$O_3 + h\nu \rightarrow O_2(^1\Delta) + O(^1D)$	$W_{1a}$ (see text)	
1b	$\rightarrow O_2(^3\Sigma) + O(^3P)$	$W_{1b}$ (see text)	
Regeneration of ozone:			
2	$O(^3P) + O_2(^3\Sigma) + O_2(^3\Sigma) \rightarrow O_3 + O_2(^3\Sigma)$	$6.95 \times 10^{-34}$	A12
3	$O(^3P) + O_2(^3\Sigma) + He \rightarrow O_3 + He$	$3.48 \times 10^{-34}$	A16
Three-body recombination forming $O_2(^3\Sigma)$ :			
4	$O(^3P) + O(^3P) + O_2(^3\Sigma) \rightarrow O_2(^3\Sigma) + O_2(^3\Sigma)$	$7.2 \times 10^{-33}$	A17
5	$O(^3P) + O(^3P) + He \rightarrow O_2(^3\Sigma) + He$	$9.0 \times 10^{-34}$	A18
Dissociation of ozone:			
6a	$O_3 + O(^1D) \rightarrow O_2(^3\Sigma) + O(^3P) + O(^3P)$	$1.2 \times 10^{-10}$	A12
6b	$\rightarrow O_2(^3\Sigma) + O_2(^3\Sigma)$	$1.2 \times 10^{-10}$	A12
7a	$O_3 + O_2(^1\Sigma) \rightarrow O_2(^3\Sigma) + O_2(^3\Sigma) + O(^3P)$	$1.54 \times 10^{-11}$	A12
8	$O_3 + O(^3P) \rightarrow O_2(^3\Sigma) + O_2(^3\Sigma)$	$8.4 \times 10^{-15}$	A12
9	$O_3 + O_2(^1\Delta) \rightarrow O_2(^3\Sigma) + O_2(^3\Sigma) + O(^3P)$	$3.8 \times 10^{-15}$	A12

Table II (Continued)

Reaction No.	Reaction	Rate Coefficient <sup>a</sup>	Reference
Reactions deactivating $O_2(^1\Sigma)$ in addition to 7a:			
7b	$O_3 + O_2(^1\Sigma) \rightarrow O_2(^3\Sigma) + O_3$	$6.6 \times 10^{-12}$	A12
7c	$\rightarrow O_2(^1\Delta) + O_3$	neglected	A12
10	$O_2(^1\Sigma) + O(^3p) \rightarrow O_2(^3\Sigma) + O(^3p)$	$8.0 \times 10^{-14}$	A12
11	$O_2(^1\Sigma) + O_2(^3\Sigma) \rightarrow O_2(^3\Sigma) + O_2(^3\Sigma)$	$4.0 \times 10^{-17}$	A12
12	$O_2(^1\Sigma) + He \rightarrow O_2(^3\Sigma) + He$	$1.0 \times 10^{-17}$	A12
Reactions deactivating $O_2(^1\Delta)$ in addition to 9:			
13	$O_2(^1\Delta) + O(^3p) \rightarrow O_2(^3\Sigma) + O(^3p)$	$1.3 \times 10^{-16}$	A19
14	$O_2(^1\Delta) + O_2(^1\Delta) \rightarrow O_2(^1\Sigma) + O_2(^3\Sigma)$	$2.0 \times 10^{-17}$	A20
15	$O_2(^1\Delta) + O_2(^3\Sigma) \rightarrow O_2(^3\Sigma) + O_2(^3\Sigma)$	$2.2 \times 10^{-18}$	A12
16	$O_2(^1\Delta) + He \rightarrow O_2(^3\Sigma) + He$	$1.0 \times 10^{-20}$	A21
Reactions deactivating $O(^1D)$ in addition to 6(a,b):			
17a	$O(^1D) + O_2(^3\Sigma) \rightarrow O(^3p) + O_2(^1\Sigma)$	$3.2 \times 10^{-11}$	A12
17b	$\rightarrow O(^3p) + O_2(^3\Sigma)$	$8.0 \times 10^{-12}$	A12
17c	$\rightarrow O(^3p) + O_2(^1\Delta)$	neglected	A12
18	$O(^1D) + He \rightarrow O(^3p) + He$	$1.5 \times 10^{-15}$	A22

<sup>a</sup>All rate coefficients are in units of molecules  $cm^3$  at 298 K.

For a homogeneous gas mixture consisting of ozone, oxygen, and helium, and assuming the mixture remains near room temperature during the photolysis process, the rate equations governing the concentrations of the different species can be written in the form:

$$\frac{dN_x}{dt} = \sum_i^i (\text{rate of reactions creating } N_x) - \sum_j^j (\text{rate of reactions consuming } N_x) \quad (\text{A11})$$

where the rates of two-body reactions are given by  $K_{12} [N_1][N_2]$ ,

the rates of three-body reactions are given by  $K_{123} [N_1][N_2][N_3]$ ,

and the rates of ozone photodecomposition are given by  $W_{1a}[O_3]$

for reactions 1a and  $W_{1b}[O_3]$  for reaction 1b.

Note that  $W_{1a}$  and  $W_{1b}$  depend on the flashlamp intensity and therefore follow the time evolution of the flashlamp pulse. In this model  $W_{1a}$  and  $W_{1b}$  are assumed constant throughout the absorption cell at any specific time. Physically, this means that the photon density is constant in the absorption cell. This condition is valid if  $\sigma[O_3] L \ll 1$  according to the Beers-Lambert law, where  $\sigma = 11.1 (10^{-18}) \text{ cm}^2$  at  $\lambda = 249 \text{ nm}$  and  $L$  is the width of the absorption cell.

For example, with 2 Torr  $O_3$  this condition requires  $L \ll 1.33 \text{ cm}$  if the photodecomposition of ozone is not accounted for. When the cell is irradiated from two sides,  $L \ll 2.66 \approx .5 \text{ cm}$  would satisfy the assumption of uniform photon density in the absorption cell. For a wider cell containing  $\geq 2 \text{ Torr } O_3$ , it would be necessary to include the effect of the spatial photon flux reduction as it propagates inside the cell.

### III. Results of Calculations and Discussions

A typical output of this model is shown in Fig. A2 which demonstrates the basic kinetic processes. The reactions are initiated by the photo-decomposition of  $O_3$  to  $O_2(^1\Delta)$  and  $O(^1D)$  (reaction 1a), or to  $O_2(^3\Sigma)$  and  $O(^3p)$  (reaction 1b). The branching ratio between 1a and 1b is consequently assumed to be 9:1. The flashlamp intensity as a function of time is assumed to be a Gaussian peaking at time = .042 seconds with a period of 13.8 ms. The formed  $O(^1D)$  is quickly deactivated to ground state atomic oxygen,  $O(^3p)$ , by collisions with  $O_3$ ,  $O_2(^3\Sigma)$ , and He. The  $O(^3p)$  then recombines with ground state molecular oxygen,  $O_2(^3\Sigma)$ , in a three-body recombination reaction to form ozone (reactions 2 and 3). The reformation of ozone throughout the pulse is enhanced at high He pressures and is responsible for the large  $O_2(^1\Delta)$  yields. In addition, reactions 2 and 3 aid in the depletion of the  $O_2(^3\Sigma)$  population which further enhances the  $\frac{[O_2(^1\Delta)]}{[O_2(^3\Sigma)]}$  ratio. Large  $\frac{[O_2(^1\Delta)]}{[O_2(^3\Sigma)]}$  ratios make the forward path of reaction A1 more favorable and thus more  $I^*(^2p_{1/2})$  can be produced. As time progresses, the  $O_2(^1\Delta)$  concentration is damped due to collisional processes while the  $O_2(^3\Sigma)$  density exceeds its initial value as a result of the decomposition of the ozone.

Fig. A3 shows the effect of helium pressure on  $O_2(^1\Delta)$  production. The  $O_2(^1\Delta)$  yield increases with helium pressure. This is due to the reformation of ozone throughout the pulse by three-body recombination (reaction 3), which is favored at higher pressures. Moreover, since the rate coefficient

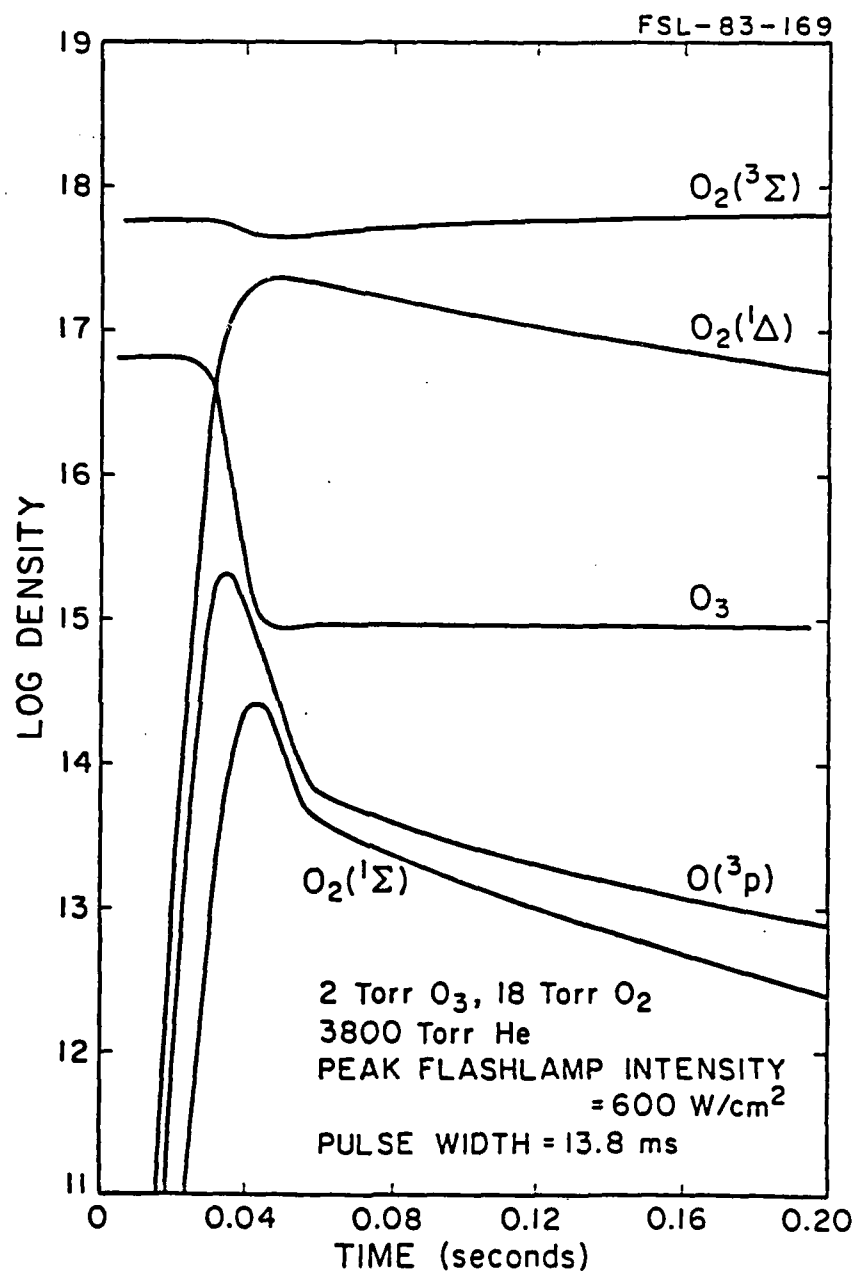


Fig. A2. Time evolution of species concentrations

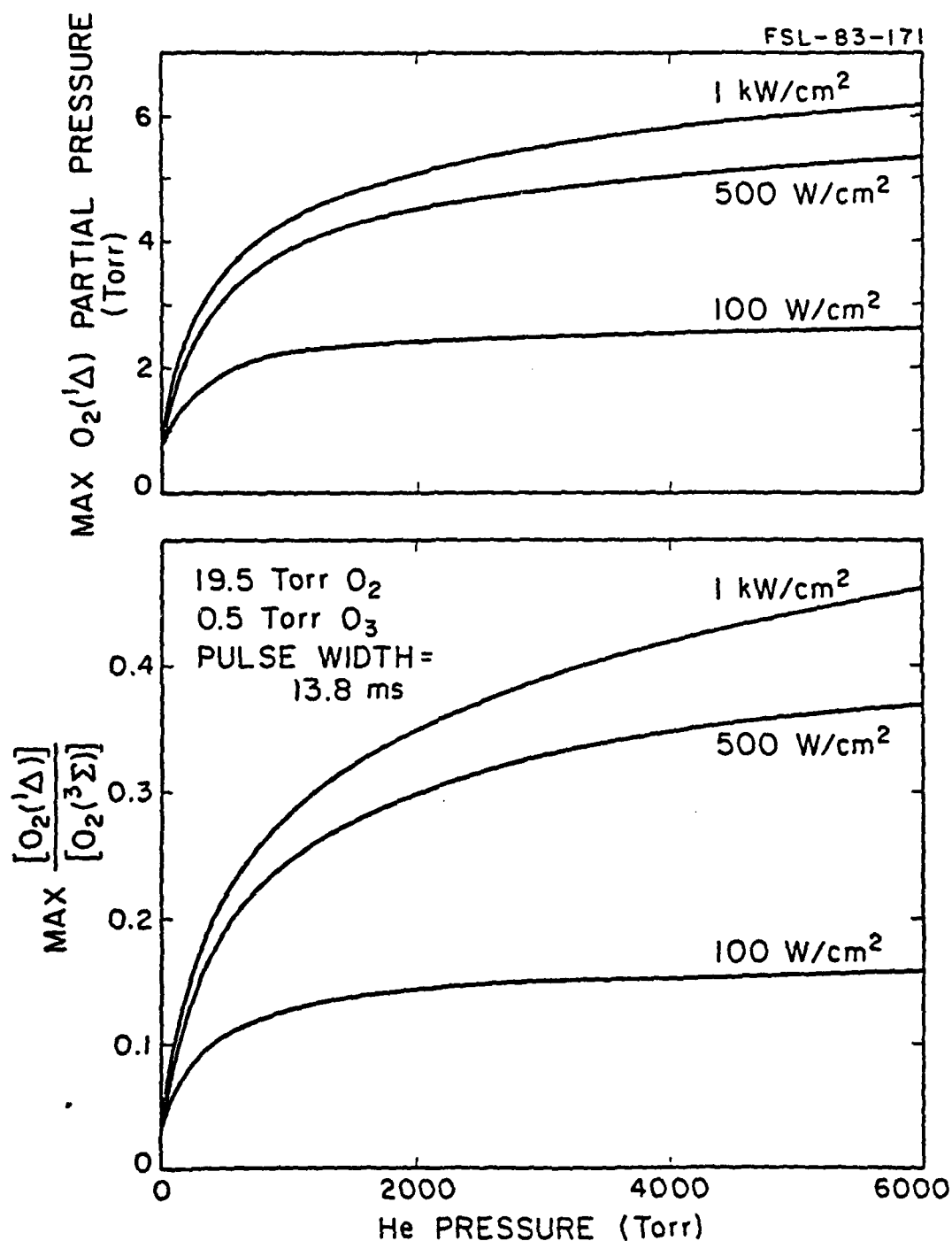


Fig. A3. Maximum  $O_2(^1\Delta)$  partial pressure ( $T = 298$  K) and  $\frac{[O_2(^1\Delta)]}{[O_2(^3\Sigma)]}$  ratio as a function of He pressure for different peak flashlamp intensities

for the deactivation of  $O_2(^1\Delta)$  by helium is low ( $<10^{-20}$ ), such high helium pressures do not greatly reduce the effective lifetime of  $O_2(^1\Delta)$ . The three-body recombination reforming  $O_2(^3\Sigma)$  (reaction 5) competes with this positive feedback regeneration of  $O_3$  and limits its effect. As the helium pressure is further increased, the concentration of  $O_2(^1\Delta)$  reaches a saturation point. This saturation point is due to the quenching of  $O_2(^1\Delta)$  by the regenerated  $O_3$  (reaction 6) which competes with its photodecomposition into  $O_2(^1\Delta)$ . The saturation point of  $O_2(^1\Delta)$  yield occurs at lower helium pressures as the flashlamp intensity is decreased. This is an expected effect of the reduction in the rate of  $O_3$  photodecomposition.

The production efficiency of  $O_2(^1\Delta)$  is highest for a short flashlamp duration. Fig. A4 is a plot of the maximum  $O_2(^1\Delta)$  yield as a function of pulse width ( $e^{-1}$  of peak value) for a constant peak flashlamp intensity and different  $O_2:O_3$  mixtures. As the pulse duration is increased the  $O_2(^1\Delta)$  yield increases up to the steady state solution of this model. However, the  $O_2(^1\Delta)$  yield for a given absorbed energy is reduced with the longer pulses. This reduction in  $O_2(^1\Delta)$  production efficiency is greater for large  $O_3$  fractions because it is a result of the slow decomposition of  $O_3$  which quenches  $O_2(^1\Delta)$ .

For operation of an  $O_2(^1\Delta)$ - $I_2$  laser it is necessary to transfer  $O_2(^1\Delta)$  from its generation point to the laser cell; therefore, the laser efficiency will depend on the effective lifetime of  $O_2(^1\Delta)$ . Fig. A5 shows the time behavior of  $O_2(^1\Delta)$  and  $O_3$  concentrations for different peak flashlamp



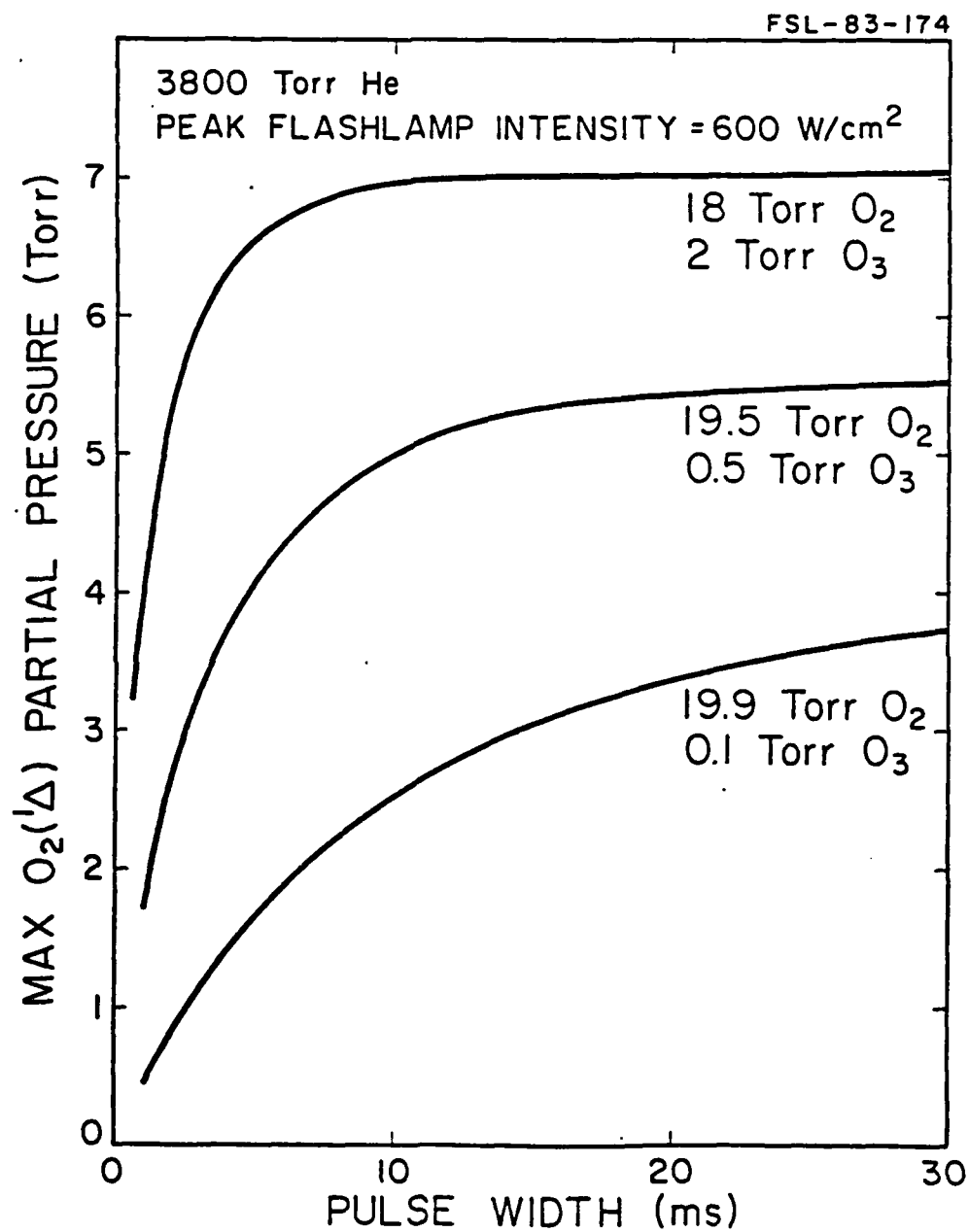


Fig. A4. Maximum O<sub>2</sub>(<sup>1</sup>Δ) partial pressure (T = 298°K) as a function of flashlamp duration

intensities. The  $O_2(^1\Delta)$  yield and its effective lifetime increase with increasing flashlamp intensity due to the enhanced rate of photodecomposition of  $O_3$ . For 2 Torr  $O_3$ , 18 Torr  $O_2$ , 3800 Torr He, a peak flashlamp intensity of  $1 \text{ KW/cm}^2$ , and a pulse width of 13.8 ms, the maximum partial  $O_2(^1\Delta)$  pressure is 7.5 Torr with an  $\frac{[O_2(^1\Delta)]}{[O_2(^3\Sigma)]}$  ratio of .58 and an effective  $O_2(^1\Delta)$  half-life of  $\approx 70$  ms. Further enhancement of the effective half-life of  $O_2(^1\Delta)$  is possible using a more intense flashlamp to further decompose  $O_3$ .

#### IV. Conclusion

Kinetic analysis of photolysis of several atmospheres of  $O_3:O_2:He$  mixtures predicts sufficient  $O_2(^1\Delta)$  yield for the operation of an  $O_2(^1\Delta)-I_2$  transfer laser. The enhancement of the rate of three-body regeneration of ozone under high pressures is responsible for the large  $O_2(^1\Delta)$  yield. Applications of such a system can include nuclear pumping of an iodine laser by utilizing a nuclear-pumped fluorescence source or its development as a solar-pumped transfer laser. In addition, the photolytic pumped  $O_2(^1\Delta)-I_2$  laser offers the potential of a continuous high-power laser with complete chemical recirculation.

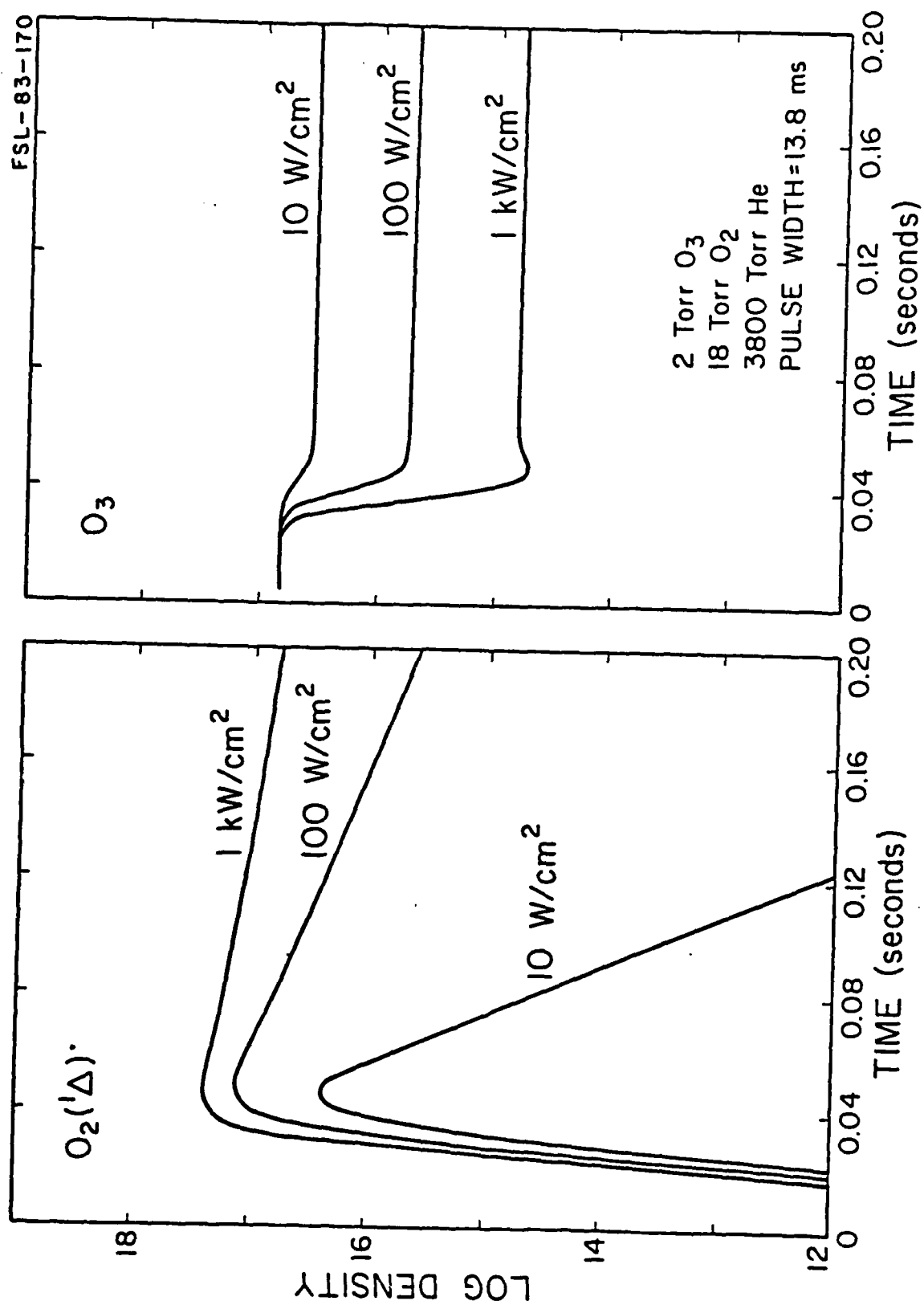


Fig. A5. Time evolution of  $O_2(^1\Delta)$  and  $O_3$  concentrations as a function of peak flashlamp intensity

## References

- A1. W. E. McDermott, N. R. Pchelkin, D. J. Benard, and R. R. Bousek, "An electronic transition chemical laser," *Appl. Phys. Lett.*, 32, pp. 469-470, 1978.
- A2. D. J. Benard, W. E. McDermot, N. R. Pchelkin, and R. R. Bousek, "Efficient operation of a 100-W transverse-flow oxygen-iodine chemical laser," *Appl. Phys. Lett.*, 34, pp. 40-41, 1979.
- A3. D. J. Miller, C. W. Clendening, W. D. English, J. G. Berg, and J. E. Trast, "A 2 KW CW chemical oxygen-iodine laser," *Conf. on Lasers and Electro-Optics*, 1982.
- A4. R. G. Derwent and B. A. Thrush, "Excitation of iodine by singlet molecular oxygen," *Faraday Disc. Chem. Soc.*, 53, pp. 162-171, 1972.
- A5. G. Fournier, J. Bonnet, and D. Pigache, "Kinetics of species produced by an electron-beam controlled discharge in oxygen at atmospheric pressure," *J. de Phys. Lett.*, 41, pp. 477-478, 1980.
- A6. G. Black and T. Slinger, "Production of  $O_2(^1\Delta)$  by oxygen atom recombination on a pyrex surface," *J. Chem. Phys.*, 74, pp. 6517, 1981.
- A7. M. S. Zediker, D. C. Shannon, H. Elsayed-Ali, and G. H. Miley, "The decay of  $O_2(^1\Delta)$  generated by nuclear pumping in a flowing Ar- $O_2$  mixture," *IEEE Int. Conf. on Plasma Science*, 1983.
- A8. A. I. Didyukov, Yu. I. Krasnoshchekov, Yu. A. Kulagin, V. A. Morozov, S. A. Reshetnyak, and L. A. Shelepin, "Photolytic generation of excited oxygen  $O_2(a^1\Delta_g)$ ," *Sov. J. Quantum Electron.*, 12, pp. 451-455, 1982.
- A9. G. H. Miley, M. Zediker, H. Elsayed-Ali, and D. Shannon, "Nuclear pumped  $I_2$  laser from  $O_3$  photodecomposition," *Conf. on Lasers and Electro-Optics*, 1983.
- A10. P. W. Fairchild and E. K. Lee, "Relative quantum yields of  $O(^1D)$  in ozone photolysis in the region between 250 and 300 nm," *Chem. Phys. Lett.*, 60, pp. 36-39, 1978.
- A11. P. F. Zittel and D. D. Little, "Photodissociation of vibrationally excited ozone," *J. Chem. Phys.*, 72, pp. 5900-5905, 1980.
- A12. D. L. Baulch, R. A. Cox, P. J. Crutzen, R. F. Hampson Jr., J. A. Kerr, J. Troe, and R. T. Watson, "Evaluated kinetic and photochemical data for atmospheric chemistry: Supplement 1," *J. Phys. Chem. Ref. Data*, 11, pp. 327-496, 1982.

- A13. J. W. Wilson and A. Shapiro, "Nuclear-induced excimer fluorescence," J. Appl. Phys., 51, pp. 2381-2393, 1980.
- A14. EG&G Electro-Optics, "High performance linear xenon flashtubes," Data Sheet F1021B-1, 1981.
- A15. Ch. A. Brau, "Rare gas halogen excimers," in Excimer Lasers, Ch. K. Rhodes, Ed., Springer-Verlag, New York, 1979, pp. 85-133.
- A16. C. L. Lin and M. T. Leu, 14th Int. Photochem. Conf., 1980. (See comments in reference 12.)
- A17. H. S. Johnson, National Standard Reference Data System, Natl. Bur. Stand., 20, 1968.
- A18. J. E. Morgan and H. I. Schiff, "Recombination of oxygen atoms in the presence of inert gases," J. Chem. Phys., 38, pp. 1495-1500, 1963.
- A19. I. D. Clark and R. P. Wayne, "The reaction of  $O_2(^1\Delta_g)$  with atomic nitrogen and with atomic oxygen," Chem. Phys. Lett., 3, pp. 405-407, 1969.
- A20. G. A. Fisk and G. N. Hays, "Kinetic rates in the oxygen-iodine system," J. Chem. Phys., 77, pp. 4965-4971, 1982.
- A21. K. H. Becker, W. Groth, and V. Schurath, "The quenching of metastable  $O_2(^1\Delta_g)$  and  $O_2(^1\Sigma_g^+)$  molecules," Chem. Phys. Lett., 8, pp. 259-262, 1971.
- A22. R. F. Heidner, D. Husian, and J. R. Wisenfield, "Kinetic study of electronically excited oxygen atoms,  $O(2^1D_2)$ , by time-resolved atomic absorption spectroscopy in the vacuum ultra-violet ( $\lambda=115, 2$  nm,  $O(3^1D_2 + 2^1D_2)$ ), Chem. Phys. Lett., 16, pp. 530-533, 1972.

## Appendix B.

## DISCUSSION OF THE MODEL

## 1) Nuclear Pumping

The basic processes modeled include the ionization and excitation of argon atoms and the oxygen molecules. The latter has been calculated with an electron distribution function and will be discussed in a later section. The ionization of argon and oxygen can be calculated using the W value approach, where the W value is the amount of energy required to create a single ion pair. Therefore, the source rate of ions becomes (Eq. B3):

$$(3) \quad S^+ = E_{\text{dep}} \phi_n,$$

where,  $E_{\text{dep}}$  = normalized energy deposition (figure B1),

$\phi_n$  = thermal neutron flux,

$W = 26.4 \text{ ev/i-p for Ar, and (Ref. B2)}$

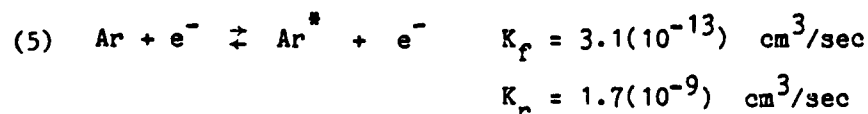
$32.5 \text{ ev/i-p for O}_2$ .

This is also used as the source rate for the fast electrons in the model.

A similar approach has been used to describe the source rate of Ar metastables with an effective W value (Eq. B4) (Ref. B3):

$$(4) \quad S^* = S^+ \left[ \frac{6.4}{20.0} \right],$$

which gave an Ar<sup>\*</sup> concentrations similar to the electron distribution function approach (Eq. B5) (Ref. B4):



Therefore, the nuclear pumping portion of the model consists of

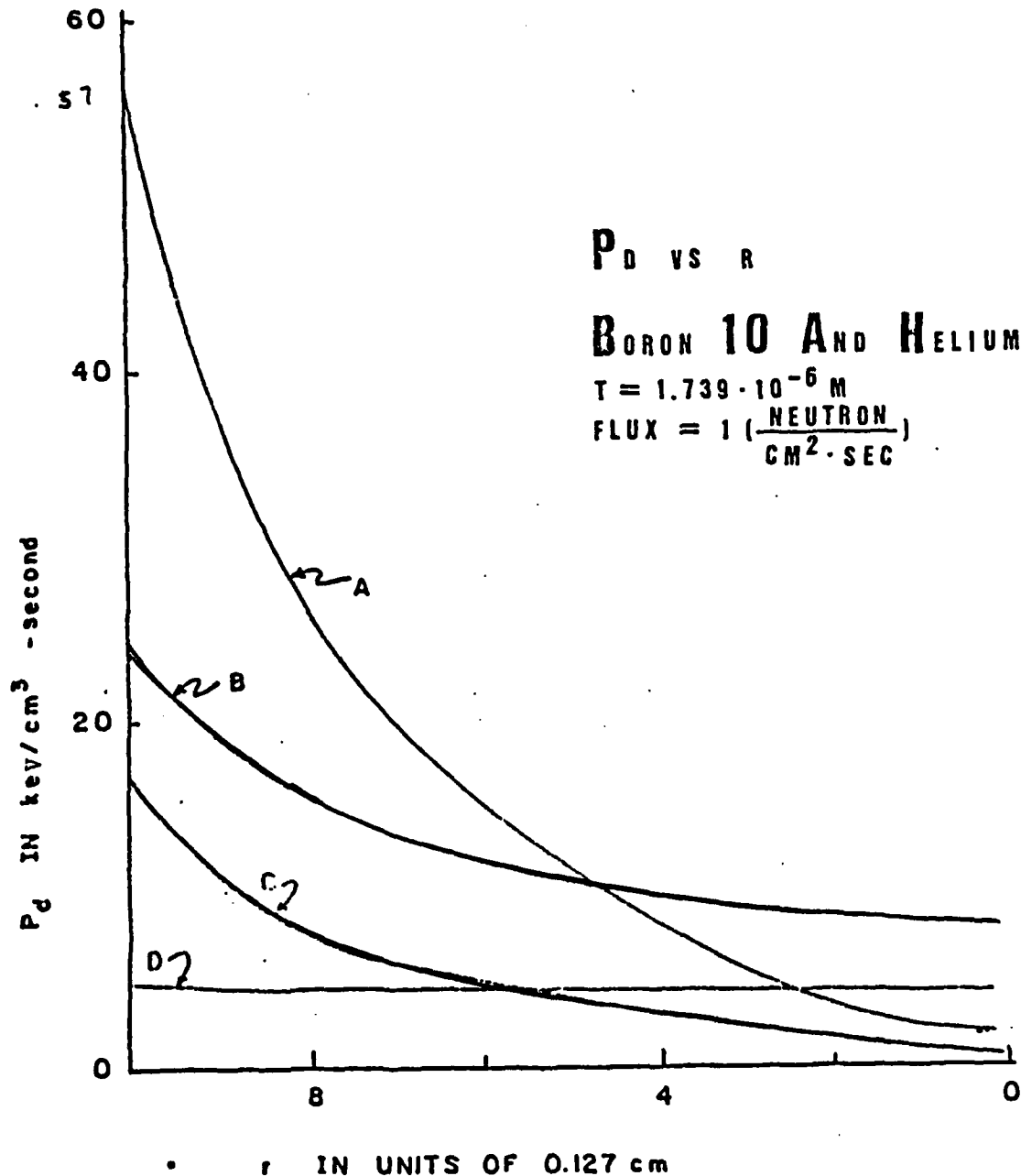


Figure B1 Power deposition of ions vs. radial distance for the case of helium gas with boron coating.

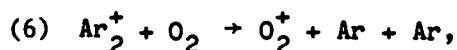
- A --- Chung's result, pressure at 760 torr
  - B --- Guyot's result, pressure at 760 torr
  - C --- Chung's result, pressure at 100 torr
  - D --- Guyot's result, pressure at 100 torr
- Coating thickness is 1.739  $\mu\text{m}$

using the appropriate power deposition term and coupling the neutron flux to the model with equation B3. Several power deposition calculations have been performed and the one quoted here is from the most recent study (Refs. B5, B6). The effects of the spatial distribution of the power (figure B1) are discussed later.

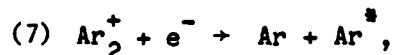
## 2) Argon Model

Nuclear pumping of an Ar-O<sub>2</sub> mixture can be broken down into; 1) Nuclear pumping of Ar, 2) energy transfer from Ar to O<sub>2</sub>, and 3) energy redistribution in O<sub>2</sub>. The net effect of adding a diatomic specie, such as oxygen, to a noble gas discharge is the complete transfer of the energy deposited in it to the diatomic.

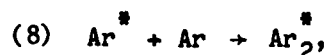
The reactions of the argon system can be found in Table B1. A flow diagram for these reactions is shown in figure B2 and reveals a very efficient pathway for the formation of O<sub>2</sub><sup>+</sup> (96% of the energy deposited in Ar<sup>+</sup> and Ar<sup>\*</sup>). This efficient energy transfer is responsible for the quenching of the optical emissions from Ar<sub>2</sub><sup>\*</sup> and Ar<sup>\*</sup>. The charge transfer reaction (Eq. B6):



prevents the dissociative recombination reaction (Eq. B7):



which effectively decreases the Ar<sup>+</sup> densities. Therefore, if the Ar<sup>\*</sup> densities are suppressed then, the reactions (Eqs. B8, B9):



are prohibited. Consequently, almost all optical emissions from these



Table B1

## ARGON MODEL REACTIONS (Eqs. B10-B21)

	<u>cm<sup>3</sup>/sec</u>	<u>Reference</u>
(10) $\text{Ar} + \alpha \rightarrow \text{Ar}^+ + e^- + \alpha$	$K = 1.3 \times 10^{-17}$	B2, B5
(11) $\text{Ar} + \alpha \rightarrow \text{Ar}^* + \alpha$	$K = 4.1 \times 10^{-18}$	B3
(12) $\text{Ar} + e \rightarrow \text{Ar}^* + e^-$	$K = 3.1 \times 10^{-13}$	B4 (x-sec)
(13) $\text{Ar}^* + e^- \rightarrow \text{Ar} + e$	$K = 1.7 \times 10^{-9}$	B4
(14) $\text{Ar}^+ + 2 \text{Ar} \rightarrow \text{Ar}_2^+ + \text{Ar}$	$K = 2.5 \times 10^{-31}$	B7
(15) $\text{Ar}_2^+ + e^- \rightarrow \text{Ar}^* + \text{Ar}$	$\alpha = 1.0 \times 10^{-6}$	B7
(16) $\text{Ar}_2^+ + e^- \rightarrow \text{Ar} + \text{Ar}$	$\alpha = 7.0 \times 10^{-7}$	B4
(17) $\text{Ar}^* + \text{Ar} \rightarrow \text{Ar}_2^+ + e_i$	$K = 5.0 \times 10^{-10}$	B7
(18) $\text{Ar}^+ + \text{O}_2 \rightarrow \text{O}_2^+ + \text{Ar}$	$K = 5.2 \times 10^{-11}$	B4, B8
(19) $\text{Ar}_2^+ + \text{O}_2 \rightarrow \text{O}_2^+ + 2 \text{Ar}$	$K = 1.5 \times 10^{-10}$	B9
(20) $\text{Ar}^+ + e \rightarrow \text{Ar} +$	$\alpha = 1.0 \times 10^{-6}$	B7
(21) $\text{Ar}^+ + \text{Ar} + e \rightarrow \text{Ar} + \text{Ar}$	$1.5 \times 10^{-30}$	B4

FSL-83-204

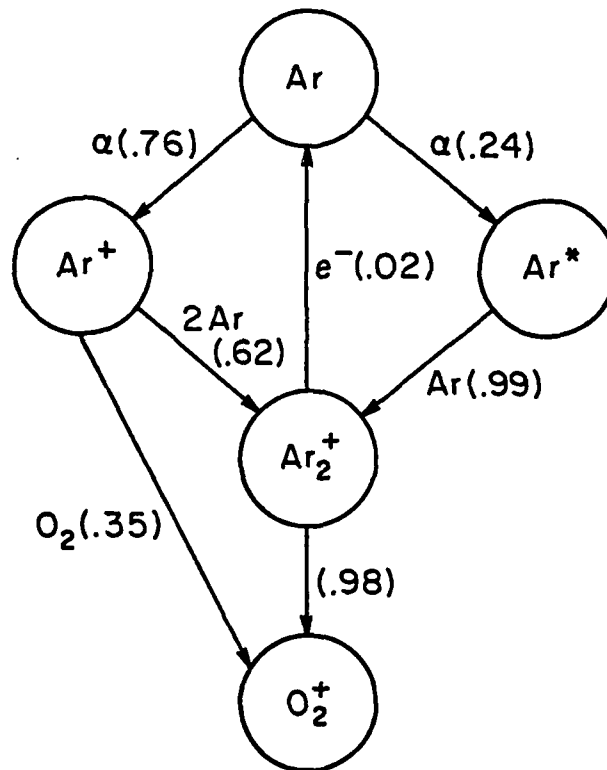


Figure B2 Energy flow diagram in an Argon-O<sub>2</sub> nuclear pumped plasma.  
 Net efficiency: α → Ar → O<sub>2</sub>: 96%

states will be suppressed upon adding even an impurity of  $O_2$  to the system.

### 3) Oxygen Model

The reaction set listed in Table B2 is based on a two energy group electron distribution function. The energy groups were defined as:

$$\begin{aligned} e_2^- & \text{ for } 10^{-2} < E < 1\text{eV} \\ e_1^- & \text{ for } E > 1\text{eV} \end{aligned}$$

This division proved to be convenient when classifying the various superelastic collisions into the cases which could supply sufficient energy to the electrons to move them from group 2 to group 1 and those that couldn't. In addition, the four distribution functions shown in figure 3 were observed by each author to have a low energy portion ( $T_e = .1 \text{ eV}$ ) which was independent of the high energy tail.

A comparison of the electron energy degradation spectrum for four cases is shown in figure B3. The results of Lo and Miley (Ref. B10), have often been accepted as describing the energy distribution function for 1 MeV alpha particles in helium. However, the addition of oxygen to the mixture should cause a downshift in the spectrum. Therefore, the use of this spectrum to calculate excitation rates from the cross sections of Fournier (Ref. B11) (figure B4) is probably an overestimation (Table B2). A better approximation is the result of Fournier (Ref. B11) for an  $Ar-O_2$  mixture at 1 atmosphere and pumped by a 2 KeV e-beam. The reaction rates calculated using this result for  $E > 1 \text{ eV}$  are listed in table B2 along with the He case. The technique used by Fournier to calculate the distribution functions was benchmarked by

Table B2  
REACTION RATES (Eqs. B22-B66)

Primary Processes (excitation)	<σv>		Eqn. No.
	[cm <sup>3</sup> /sec] α-particle (He)	[cm <sup>3</sup> /sec] 2 keV e-beam (Ar-O <sub>2</sub> )	
$e_2^- + O_2 (X^3\Sigma) \rightarrow e_2^- + O_2(a^1\Delta)$	1.05 (-15)	1.05 (-15)	B 22
$e_1^- + O_2 (X^3\Sigma) \rightarrow e_2^- + O_2(a^1\Delta)$	3.74 (-12)	9.65 (-13)	B 23
$e_2^- + O_2 (X^3\Sigma) \rightarrow e_2^- + O_2(b^1\Sigma)$	1.75 (-19)	1.75 (-19)	B 24
$e_1^- + O_2 (X^3\Sigma) \rightarrow e_2^- + O_2(b^1\Sigma)$	9.99 (-13)	2.86 (-13)	B 25
$e_1^- + O_2 (X^3\Sigma) \rightarrow e_2^- + O_2(A^3\Sigma)$	3.60 (-12)	1.75 (-13)	B 26
$e_1^- + O_2 (X^3\Sigma) \rightarrow e_2^- + O_2(B^3\Sigma)$	6.37 (-13)	7.75 (-14)	B 27
$e_2^- + O_2 (a^1\Delta) \rightarrow e_2^- + O_2(b^1\Sigma)$	1.71 (-12)	1.71 (-12)	B 28
$e_1^- + O_2 (a^1\Delta) \rightarrow e_2^- + O_2(b^1\Sigma)$	2.57 (-11)	8.56 (-12)	B 29
$e_1^- + O_2 (a^1\Delta) \rightarrow e_2^- + O_2(A^3\Sigma)$	3.60 (-12)	1.75 (-13)	B 30
$e_1^- + O_2 (a^1\Delta) \rightarrow e_2^- + O_2(B^3\Sigma)$	6.37 (-13)	7.75 (-14)	B 31
$e_1^- + O_2 (b^1\Sigma) \rightarrow e_2^- + O_2(A^3\Sigma)$	3.6 (-12)	1.75 (-13)	B 32
$e_1^- + O_2 (b^1\Sigma) \rightarrow e_2^- + O_2(B^3\Sigma)$	6.37 (-13)	7.75 (-14)	B 33
$e_1^- + O_2 (A^3\Sigma) \rightarrow e_2^- + O_2(B^3\Sigma)$	8.1 (-12)	8.1 (-13)	B 34

Table B2 (Continued)

REACTION RATES (Eqs. B22-B66)

Primary Processes (Superelastic)	<σv>		Eqn. No.
	[cm <sup>3</sup> /sec] α-particle (He)	[cm <sup>3</sup> /sec] 2 keV e-beam (Ar-O <sub>2</sub> )	
O <sub>2</sub> (B <sup>3</sup> Σ) + e <sub>2</sub> <sup>-</sup> → e <sub>1</sub> <sup>-</sup> + O <sub>2</sub> (X <sup>3</sup> Σ)	2.76 (-8)	2.76 (-8)	B35
O <sub>2</sub> (B <sup>3</sup> Σ) + e <sub>1</sub> <sup>-</sup> → e <sub>1</sub> <sup>-</sup> + O <sub>2</sub> (X <sup>3</sup> Σ)	1.96 (-10)	7.25 (-11)	B36
O <sub>2</sub> (A <sup>3</sup> Σ) + e <sub>2</sub> <sup>-</sup> → e <sub>1</sub> <sup>-</sup> + O <sub>2</sub> (X <sup>3</sup> Σ)	8.48 (-9)	8.48 (-9)	B37
O <sub>2</sub> (A <sup>3</sup> Σ) + e <sub>1</sub> <sup>-</sup> → e <sub>1</sub> <sup>-</sup> + O <sub>2</sub> (X <sup>3</sup> Σ)	2.73 (-10)	8.26 (-11)	B38
O <sub>2</sub> (b <sup>1</sup> Σ) + e <sub>2</sub> <sup>-</sup> → e <sub>2</sub> <sup>-</sup> + O <sub>2</sub> (X <sup>3</sup> Σ)	3.02 (-10)	3.02 (-10)	B39
O <sub>2</sub> (b <sup>1</sup> Σ) + e <sub>1</sub> <sup>-</sup> → e <sub>1</sub> <sup>-</sup> + O <sub>2</sub> (X <sup>3</sup> Σ)	7.67 (-12)	2.77 (-12)	B40
O <sub>2</sub> (a <sup>1</sup> Δ) + e <sub>2</sub> <sup>-</sup> → e <sub>2</sub> <sup>-</sup> + O <sub>2</sub> (X <sup>3</sup> Σ)	9.83 (-11)	9.83 (-11)	B41
O <sub>2</sub> (a <sup>1</sup> Δ) + e <sub>1</sub> <sup>-</sup> → e <sub>1</sub> <sup>-</sup> + O <sub>2</sub> (X <sup>3</sup> Σ)	1.08 (-11)	3.42 (-12)	B42
O <sub>2</sub> (B <sup>3</sup> Σ) + e <sub>2</sub> <sup>-</sup> → e <sub>1</sub> <sup>-</sup> + O <sub>2</sub> (a <sup>1</sup> Δ)	1.84 (-8)	1.84 (-8)	B43
O <sub>2</sub> (B <sup>3</sup> Σ) + e <sub>1</sub> <sup>-</sup> → e <sub>1</sub> <sup>-</sup> + O <sub>2</sub> (a <sup>1</sup> Δ)	1.30 (-10)	4.83 (-11)	B44
O <sub>2</sub> (A <sup>3</sup> Σ) + e <sub>2</sub> <sup>-</sup> → e <sub>1</sub> <sup>-</sup> + O <sub>2</sub> (a <sup>1</sup> Δ)	8.48 (-9)	8.48 (-9)	B45
O <sub>2</sub> (A <sup>3</sup> Σ) + e <sub>1</sub> <sup>-</sup> → e <sub>1</sub> <sup>-</sup> + O <sub>2</sub> (a <sup>1</sup> Δ)	1.82 (-10)	5.51 (-11)	B46
O <sub>2</sub> (b <sup>1</sup> Σ) + e <sub>2</sub> <sup>-</sup> → e <sub>2</sub> <sup>-</sup> + O <sub>2</sub> (a <sup>1</sup> Δ)	2.51 (-9)	2.51 (-9)	B47
O <sub>2</sub> (b <sup>1</sup> Σ) + e <sub>1</sub> <sup>-</sup> → e <sub>1</sub> <sup>-</sup> + O <sub>2</sub> (a <sup>1</sup> Δ)	6.63 (-11)	2.34 (-11)	B48
O <sub>2</sub> (B <sup>3</sup> Σ) + e <sub>2</sub> <sup>-</sup> → e <sub>1</sub> <sup>-</sup> + O <sub>2</sub> (b <sup>1</sup> Δ)	9.20 (-9)	4.37 (-9)	B49
O <sub>2</sub> (B <sup>3</sup> Σ) + e <sub>1</sub> <sup>-</sup> → e <sub>1</sub> <sup>-</sup> + O <sub>2</sub> (b <sup>1</sup> Σ)	6.50 (-11)	2.4 (-11)	B50
O <sub>2</sub> (A <sup>3</sup> Σ) + e <sub>2</sub> <sup>-</sup> → e <sub>1</sub> <sup>-</sup> + O <sub>2</sub> (b <sup>1</sup> Σ)	2.83 (-9)	1.70 (-9)	B51
O <sub>2</sub> (A <sup>3</sup> Σ) + e <sub>1</sub> <sup>-</sup> → e <sub>1</sub> <sup>-</sup> + O <sub>2</sub> (b <sup>1</sup> Σ)	9.1 (-11)	2.75 (-11)	B52
O <sub>2</sub> (B <sup>3</sup> Σ) + e <sub>2</sub> <sup>-</sup> → e <sub>2</sub> <sup>-</sup> + O <sub>2</sub> (A <sup>3</sup> Σ)	1.22 (-8)	1.22 (-8)	B53
O <sub>2</sub> (B <sup>3</sup> Σ) + e <sub>1</sub> <sup>-</sup> → e <sub>1</sub> <sup>-</sup> + O <sub>2</sub> (A <sup>3</sup> Σ)	1.08 (-10)	3.5 (-11)	B54

Table B2 (Concluded)

REACTION RATES (Eqs. B22-B66)

Primary Processes (Ionization)	<σv>		Eqn. No.
	[cm <sup>3</sup> /sec] α-particle (He)	[cm <sup>3</sup> /sec] 2 keV e-beam (Ar-O <sub>2</sub> )	
$O_2(X^3\Sigma), (a^1\Delta), (b^1\Sigma), (A^3\Sigma), (B^3\Sigma)$			
$+ e_1^- \rightarrow e_2^- + O_2^+$	8.68 (-13)	1.48 (-13)	B 56
$\rightarrow e_2^- + O + O + O^+$	1.26 (-13)	3.40 (-14)	B 56
<u>Dissociative Attachment</u>			
$O_2(X^3\Sigma) + e_1^- \rightarrow O + O^-$	1.20 (-13)	9.96 (-15)	B 57
$O(a^1\Delta) + e_1^- \rightarrow O + O^-$	6.6 (-13)	8.7 (-14)	B 58
$O_2(b^1\Sigma) + e_1^- \rightarrow O + O^-$	9.05 (-13)	1.28 (-13)	B 59
$O_2(A^3\Sigma) + e_1^- \rightarrow O + O^-$	9.5 (-13)	3.15 (-13)	B 60
$O_2(A^3\Sigma) + e_2^- \rightarrow O + O^-$	1.05 (-15)	1.05 (-15)	B 61
$O_2(B^3\Sigma) + e_1^- \rightarrow O + O^-$	1.24 (-12)	4.58 (-13)	B 62
$O_2(B^3\Sigma) + e_2^- \rightarrow O + O^-$	2.31 (-14)	2.31 (-14)	B 63
<u>4.5 eV Loss Processes</u>			
$O_2(X^3\Sigma) + e_1^- \rightarrow e_2^- + O_2^*$	8.02 (-13)	5.83 (-14)	B 64
<u>Elastic Collisions</u>			
$O_2(X^3\Sigma) + e_1^- \rightarrow e_2^- + O_2$	8.00 (-10)	2.84 (-10)	B 65
$O_2(X^3\Sigma) + e_2^- \rightarrow e_2^- + O_2$		2.14 (-8)	B 66

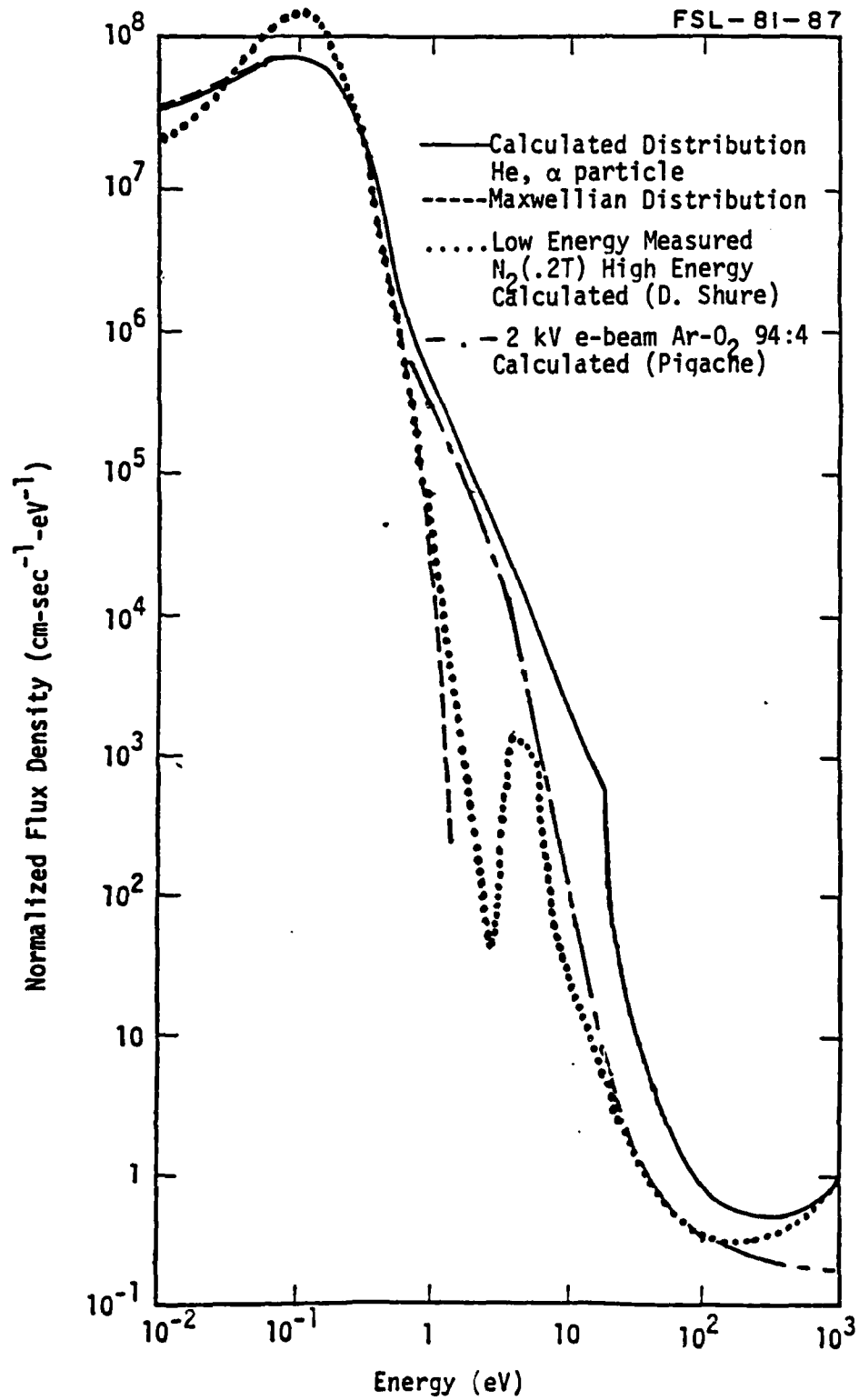


Figure B3 A comparison of three separate results for e-beams in He(Lo), Ar- $\text{O}_2$  (Pigache) and  $\text{N}_2$  (Shure, Pigache)

## CROSS SECTIONS IN OXYGEN

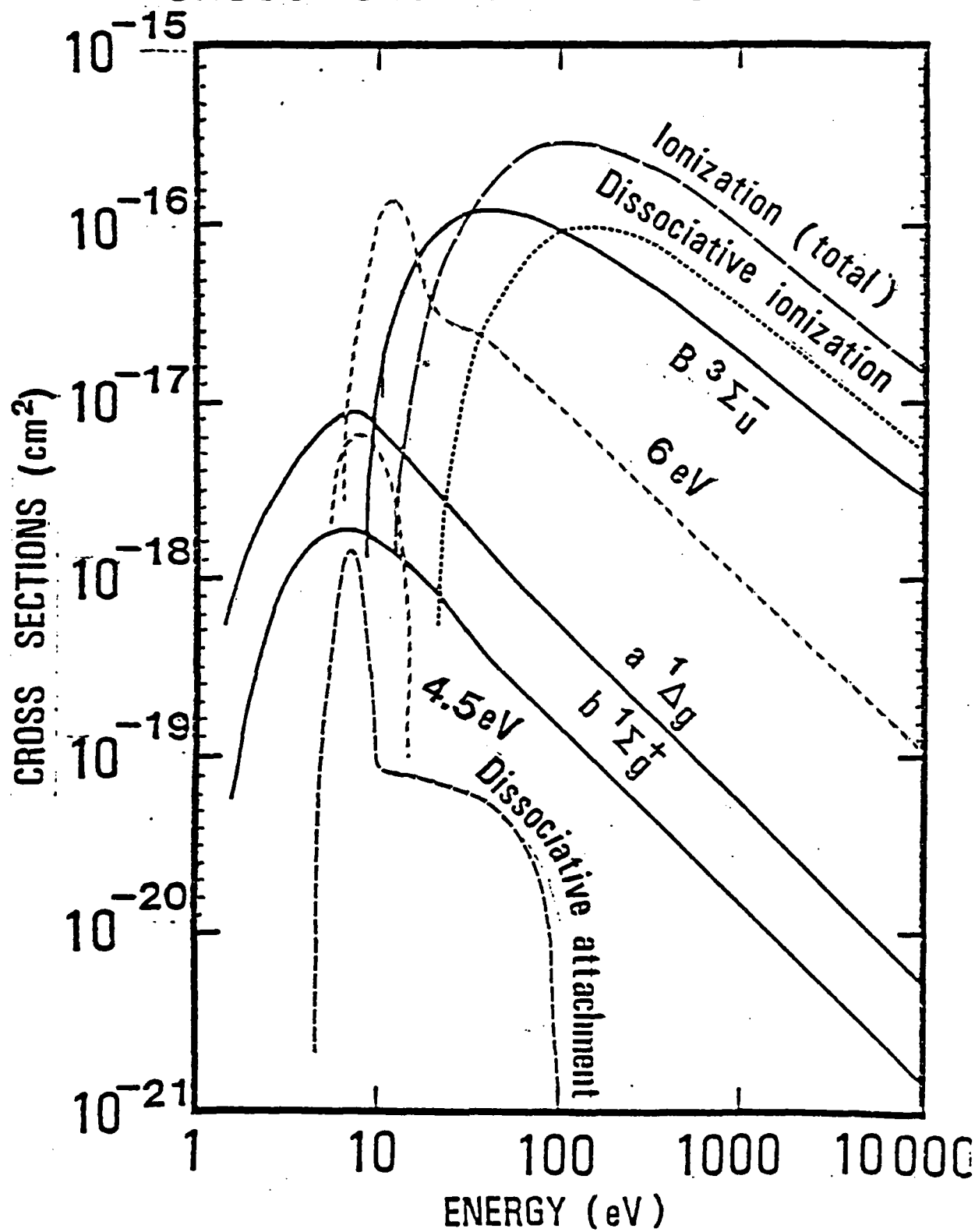


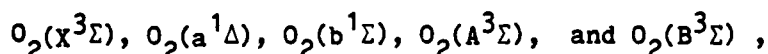
Figure B4 Cross Sections Suggested by Fournier.



performing a calculation in  $N_2$  and comparing it to the distribution function measured by Shure (Ref. B12) in a hollow cathode discharge. In general, the agreement was good over the energy range examined ( $1 < E < 10$  eV).

The calculation of  $\langle \sigma v \rangle$  was performed with cross sections obtained from Fournier (Ref. B11). In the model, the following processes have been considered (table B2):

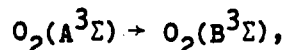
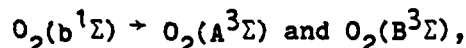
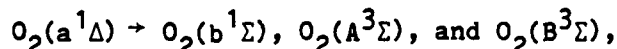
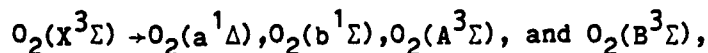
(A) Ionization;



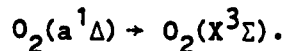
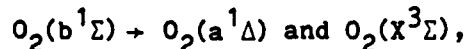
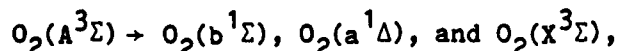
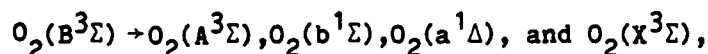
(B) Dissociative ionization of the same states,

(C) Dissociative attachment of the same states,

(D) Excitation reactions;



(E) Superelastic collisions;



The cross section for many of these processes had to be generated from the known set of cross sections given in figure B4. To obtain an excitation or ionization rate from a given electronic state, the cross section for the ground state process was translated to a lower energy by the energy content of the electronic state of interest. If possible, the resulting cross section was normalized to an

experimental results ( $O_2(a^1\Delta) \rightarrow O_2(b^1\Sigma)$ ) (Ref. B13). The superelastic rates were then calculated from the excitation cross sections generated from the ground state processes.

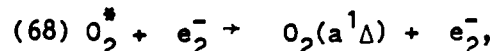
The results of these calculations are listed in Table B2. It is apparent from this table, that there is a strong coupling between the  $O_2(a^1\Delta)$ ,  $O_2(b^1\Sigma)$ , and  $O_2(x^3\Sigma)$  states. Superelastic rates from the  $O_2(A^3\Sigma)$  and  $O_2(B^3\Sigma)$  states to the lower states are large and suggest a strong relaxation of the higher lying states during the discharge. However, the excitation of the  $O_2(A^3\Sigma)$  and  $O_2(B^3\Sigma)$  by electrons is weak in the two cases studied here. Consequently, any contributions to the  $O_2(b^1\Sigma)$  and  $O_2(a^1\Delta)$  states will be small since the pumping rates into the higher states are so low. A similar argument can be applied to the  $O_2(C^3\Delta)$  and  $O_2(c^1\Sigma)$  states which lie near the  $O_2(A^3\Sigma)$  state.

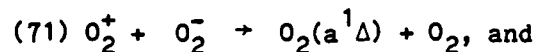
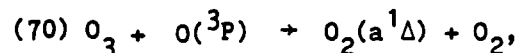
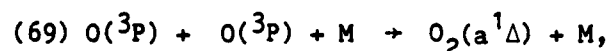
#### 4) Chemical Kinetics

Two species were measured in the experiments:  $O_2(a^1\Delta)$  and  $O_3$ . Therefore, this section is subdivided into two topics. The first discussion describes the reactions which generate  $O_2(a^1\Delta)$  while the second section discusses the reactions important in the formation of ozone.

##### a. $O_2(a^1\Delta)$

The development of the  $O_2(a^1\Delta)$  model began by considering the six pathways capable of generating  $O_2(a^1\Delta)$  (Eqs. B67-B72):





Among these reactions, 70 and 71 were found to be the least important in comparison to reactions 67 and 68. Attempts to classify reaction 69 was difficult, because the rate has only been calculated or estimated in the research performed to date. This is apparent in Table B3 which is a summary of the current literature on atomic oxygen recombination. In this table, reaction rate 73 is inconsistent with other estimations. Since it was obtained through a calculation while the others were based on experimental observation, the other estimates are probably better. Thus, based on the estimates available (table 3), there should be no significant contribution to the  $\text{O}_2(\text{a}^1\Delta)$  concentration from atomic recombination. Consequently, the dominant formation pathways in a nuclear or e-beam pumped system appear to be reactions 67, 68 and 72.

Of the five states above  $\text{O}_2(\text{a}^1\Delta)$ , only  $\text{O}_2(\text{b}^1\Sigma)$  is not readily dissociated by electron impact. This is probably due to its relatively low energy compared to the other states (1.62 eV versus  $E > 4.5$  eV) of interest. In addition, the  $\text{O}_2(\text{b}^1\Sigma)$  state was the only state which was able to build up a significant concentration throughout the pulse. Consequently, it is the only state which is of any importance in the formation of  $\text{O}_2(\text{a}^1\Delta)$ . This conclusion is supported by the reaction rates calculated in the last section and by the rates listed in Table B3. Even though the recombination rates into the  $\text{O}_2(\text{A}^3\Sigma)$  and

Table B3 (Units of  $\text{cm}^6/\text{sec}$ ) (Eqs. B73-B85)

$\text{O}_2(^3\Sigma)$	$\text{O}_2(a^1\Delta)$	$\text{O}_2(b^1\Sigma)$	$\text{O}_2(A^3\Sigma)$	Comments	Ref.
(73) $1.2(10^{-33})$	$7(10^{-34})$	$3.2(10^{-34})$	$3.8(10^{-34})$	Calc.	14
(74) $7.4(10^{-33})$	-	-	-	Exp. Disch.	15
(75) $(10^{-33})$	-	-	-	Calc.	16
(76) $2.8(10^{-33})$	-	-	-	Exp. Shock Tube	17
(77) $9.4(10^{-32})$	-	-	-	Exp. Shock Tube	18
(78) -	-	$\sim 10^{-37}$	$\sim 10^{-21}$	Exp. No + N	19
(79) -	Not Favored	-	Easily Dissociated	Exp. No + N	20
(80) $(10^{-33})$	-	$1.1(10^{-37})$	$10^{-21}$	Exp. No + N	20
(81) -	Not Observable	-	-	Exp. Disch.	21
(82) -	$1.7(10^{-37})^{**}$	$3.3(10^{-37})$	$10^{-34}$	Exp. No + N	22
(83) -	$3(10^{-37})^{**}$	-	-	Unknown	23
(84) -	$<10^{-36}$	$1.4(10^{-37})$	-	Summary	24
(85) $3(10^{-33})$	-	-	-		25, 26

\* Two body dependence

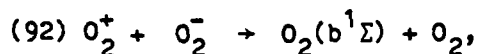
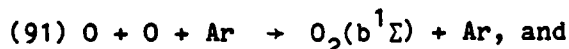
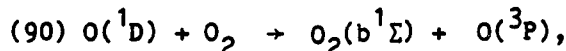
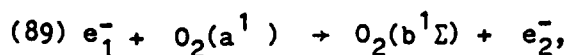
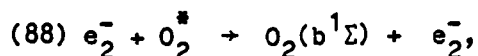
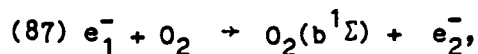
\*\* Estimated from  $\text{O}_2(^1\Sigma)$  behavior.

$O_2(B^3\Sigma)$  states are the largest, the majority of the O atoms are lost by the three body reaction (Eq. B86):



in forming  $O_3$ . This effect is obvious for  $[O_2] \gg [O]$  since reaction 69 is second order in  $[O]$  while 86 is first order.

To complete the model of  $O_2(a^1\Delta)$  generation, it is necessary to examine the possible  $O_2(b^1\Sigma)$  production mechanisms. Again, there are several candidates (Eqs. B87-B92):

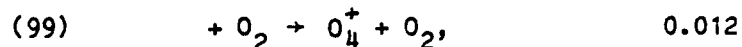
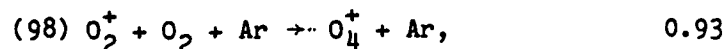
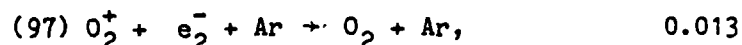
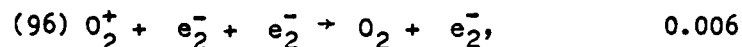


where, reaction 91 can be eliminated with the arguments presented above and reaction 92 was found to be negligible. In addition, reactions 87, 88, and 89 were found to be insignificant in comparison to the pumping rate of reaction 90. This reaction was found to dominated both the generation of  $O_2(b^1\Sigma)$  and the loss of  $O(^1D)$ .

The main source of  $O(^1D)$  in the discharge is the dissociative recombination of  $O_2^+$  (Eqs. B93-B95):

	Branching Ratio
(93) $O_2^+ + e_2^- \rightarrow O + O,$	0.008
(94) $\rightarrow O(^1D) + O(^1D),$	0.025
(95) $\rightarrow O(^1S) + O(^1S),$	0.002

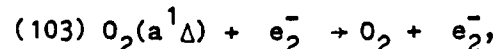
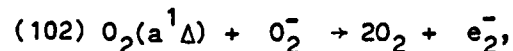
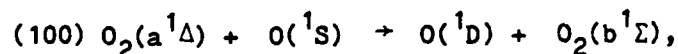
where, the  $O_2^+$  is also lost by the reactions (Eqs. B96-B99):



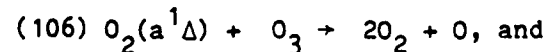
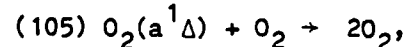
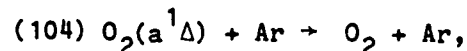
and the  $O_4^+$  is consumed by a variety of fast reactions but dominated by dissociative recombination. The final model for the production of  $O_2(a^1\Delta)$  is diagrammed in figure B5. In this figure, the relative importance of the  $O_2(a^1\Delta)$  pumping mechanisms are; (67) = 0.08, (68) = 0.77, and (72) = 0.14. From this breakdown, it is apparent that the main excitation mechanism is the energy transfer from  $O(^1D)$  to  $O_2$  to form  $O_2(b^1\Sigma)$  followed by the relaxation of  $O_2(b^1\Sigma)$  into  $O_2(a^1\Delta)$ .

Throughout the discharge and afterglow, several of the species generated can lead to the deactivation of  $O_2(a^1\Delta)$  and  $O_2(b^1\Sigma)$ . A study of the known reactions found the following reactions to be important losses of  $O_2(a^1\Delta)$  (Eqs. B100-B107):

#### Discharge



#### Afterglow



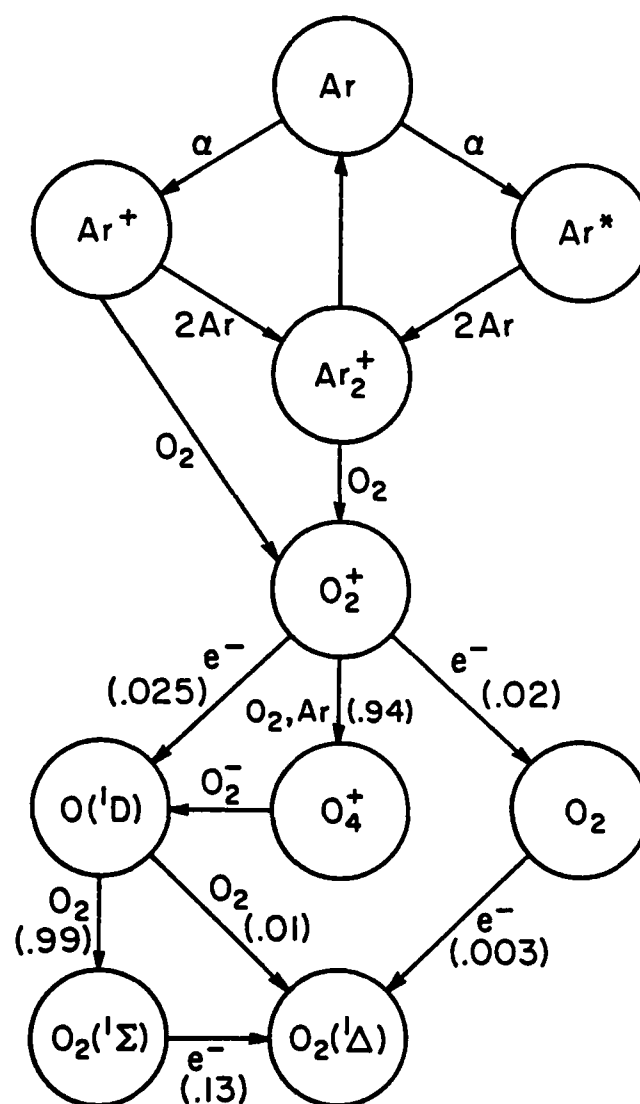
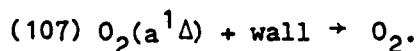
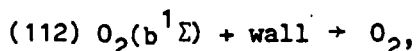
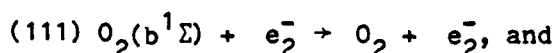
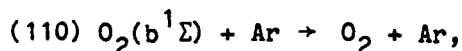
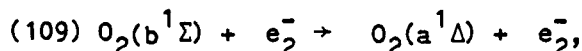
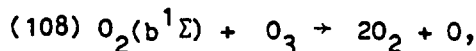


Figure B5 Energy transfer leading to the formation of  $\text{O}_2(^1\Delta)$  dominates all of the other production mechanisms in a nuclear pumped plasma.



At the low  $\text{O}_2(a^1\Delta)$  densities predicted, the bimolecular reaction was found to be unimportant. Similarly, the dominant losses for  $\text{O}_2(b^1\Sigma)$  are (Eqs. B108-B112):



where, reaction 108 is very important in the  $\text{O}_3$  kinetics scheme.

#### b. Ozone

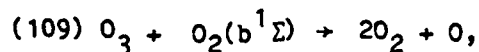
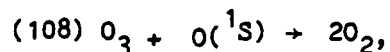
During this study,  $\text{O}_3$  was found to be one of the major species in an Ar- $\text{O}_2$  afterglow. Both calculations and experiments have indicated this which leads to the present discussion of the kinetics involved in the formation of  $\text{O}_3$ . As was the case in the last section, there are many potential sources of  $\text{O}_3$  in the discharge. With the aid of the model it was possible to sort through each of the  $\text{O}_3$  producing reactions known and determine their relative importance (Eqs. B113-B117):

	Contributing Fraction
(113) $\text{O} + \text{O}_2 + \text{Ar} \rightarrow \text{O}_3 + \text{Ar},$	0.65
(114) $\text{O}_4^+ + \text{O} \rightarrow \text{O}_3 + \text{O}_2^+,$	0.22
(115) $\text{O} + \text{O}_2^- \rightarrow \text{O}_3 + e_2^-,$	0.08
(116) $\text{O}_2^+ + \text{O}_3^- \rightarrow \text{O}_3 + \text{O}_2,$	0.04
(117) $\quad \quad \quad \rightarrow \text{O}_3 + \text{O} + \text{O},$	0.02



with the majority of the  $O_3$  being formed by the three body recombination reaction (113). The source of O atoms and  $O_4^+$  can be traced to  $O_2^+$ . A diagram of this model is indicated in figure B6 with the branching ratio of each important reaction.

The inherent stability of  $O_3$  results in the formation of large concentrations (with respect to  $O_2(a^1\Delta)$ ) after the discharge. Indeed, only two loss mechanisms were found important throughout the duration of the discharge (Eqs. B108-B109):



but since reaction (109) results in the formation of atomic oxygen, at least 1/3 of the O atoms will return to form  $O_3$  under the conditions of Ar pressure < 150 Torr. If the Ar pressure  $\gg$  150 torr, then the effects of diffusion become negligible and all of the atomic oxygen recombines to form ozone. This will result in reaction (108) becoming the dominant loss of ozone throughout the pulse. However, at  $P(\text{Ar}) = 150$  Torr, the relative importance of these two reactions were: (108) = 0.45, and (109) = 0.44. Therefore, any loss of  $O_3$  in a long pulse can be attributed to the reactions which occur during the collisions with  $O(^1S)$  and  $O_2(b^1\Sigma)$ . Since, these states are a result of the recombination of  $O_2^+$ , it appears that a short pulse will be more efficient in the formation of  $O_3$  because the metastable species require a long time to build up.

FSL-83-206

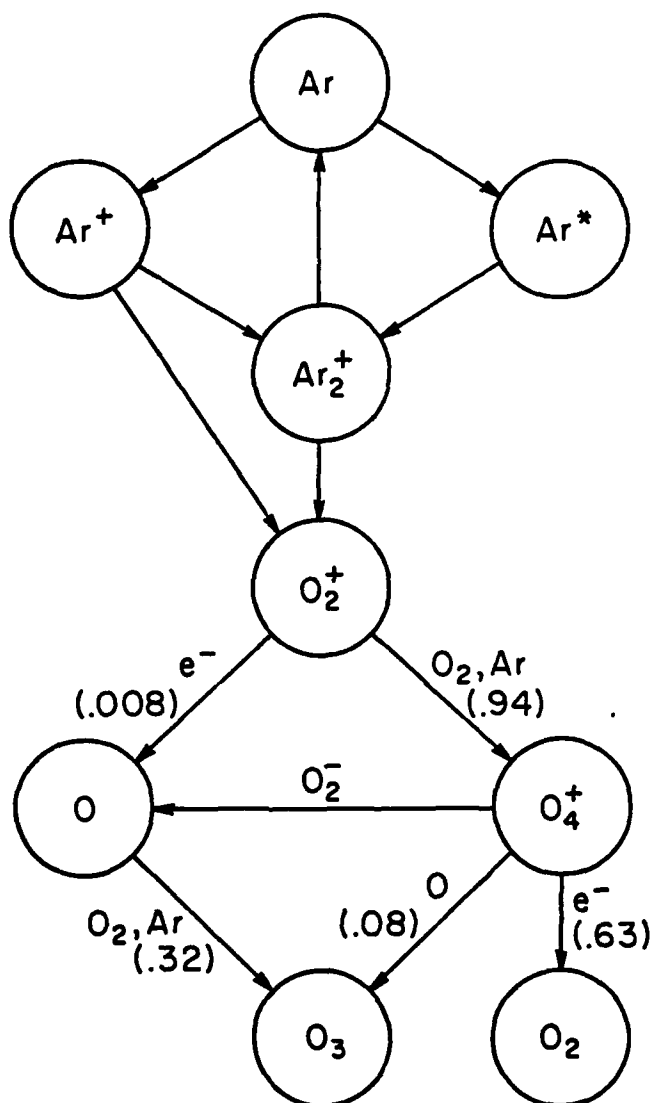
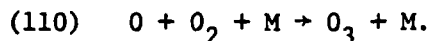


Figure B6 Flow diagram for reactors which generate O<sub>3</sub> in an Ar-O<sub>2</sub> nuclear pumped plasma for a \$3.00 pulse.

One of the largest discrepancies observed so far between the modeling and experiments involves ozone yields. The production of ozone is thought to be due to the three body reaction (Eq. B110):



Thus, any discrepancy must be a direct result of an overestimation of the atomic oxygen concentrations. One potential reason for this problem may be the neglected wall interaction mechanisms in the model. Attempts to model this effect immediately produced better agreement but required a greatly enhanced reaction rate in comparison to the value obtained by the general expression (Eq. B111):

$$(111) \quad \tau_d = \frac{\Lambda^2}{D} P + \frac{4R}{3G\gamma}$$

where:

$$\Lambda^2 = (R/\pi)^2 = \text{characteristic dimension}$$

$$P = \text{pressure of gas : 150 Torr}$$

$$D = \text{diffusion coefficient: } 228 \text{ cm}^2 \text{ Torr/sec for O atoms (Ref. B24)}$$

$$R = \text{radius of tube} = 1.27 \text{ cm}$$

$$G = \text{thermal velocity } 6.3 \times 10^4 \text{ cm/sec}$$

$$\gamma = \text{wall deactivation efficiency, } 10^{-5} < \gamma < 1.0$$

This expression yields  $1/\tau_D = 9 \text{ sec}^{-1}$  for a cosine function distribution. Consequently, it was necessary to determine more details about the diffusion mechanism and associated spatial effects.

The power deposition profile is similar to Figure B2 which is a result derived by A. Chung (Ref. B5) for various helium pressures. The very steep gradients resolved can strongly influence diffusion. To obtain an estimate of the importance of this profile an analytic solution was obtained to the diffusion equation. The source was represented as a square pulse in time

with the following spatial distribution (Eq. B112):

$$(112) \quad S_0 = A_0 (1 - \sin Bx)$$

where:

$$A_0 = \text{source rate of O atoms} \sim 10^{17} \text{ a/cm}^3\text{-sec}$$

$$B = \pi/2.$$

The solution to the diffusion equation (Eq. B113):

$$(113) \quad \frac{d[O]}{dt} = D \frac{d^2[O]}{dx^2} + A_0 (1 - \sin Bx) U(t-t_0)$$

subject to the B.C. (Eqs. B114, B115):

$$(114) \quad \frac{d[O]}{dx} = 0 \text{ @ } x = 1.0$$

$$(115) \quad [O] = 0 \text{ @ } x = 0$$

was easily obtained via Laplace transform techniques. Homogeneous reactions were then added to the solution via Danckwert's method (Eq. B116) (Ref. B27).

$$(116) \quad [O] = K_H \int_0^t [O], e^{-k_H t'} dt' + [O], e^{-k_H t}$$

A typical result for a 10 millisecond pulse and no homogeneous reactions is shown in Figure B7. Similarly, if  $K_H = 50$  only a small decrease in the peak concentrations is observed in Figure B8 while the strong depletion after the pulse is expected. Consequently, the diffusion on this simple slab case appears to dominate the losses of atomic oxygen during the pulse. This is further exemplified in Table B4 which lists the diffusion decay constant as a function of position in the slab.

A comparison of the decay constants @  $t = .012$  msec and  $t = .100$  msec indicates that a rather strong depletion occurs in the regions closest to the walls where the concentration closely follows the source's spatial distribution. This simple analysis justifies the use of an "enhanced" diffusion rate in the kinetics model.

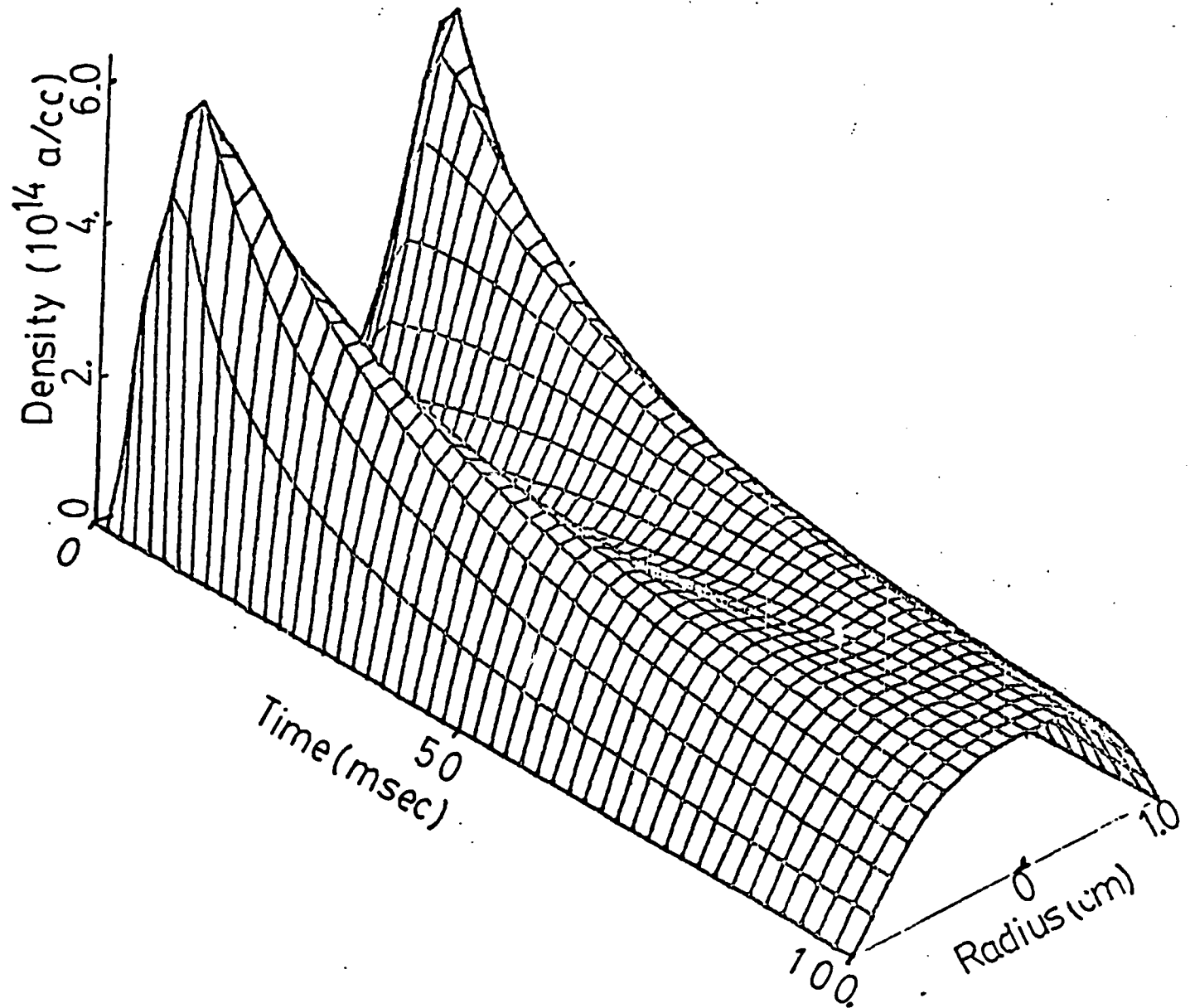


Figure B7 Time and spatial dependence of O atoms neglecting  $K_H$ .

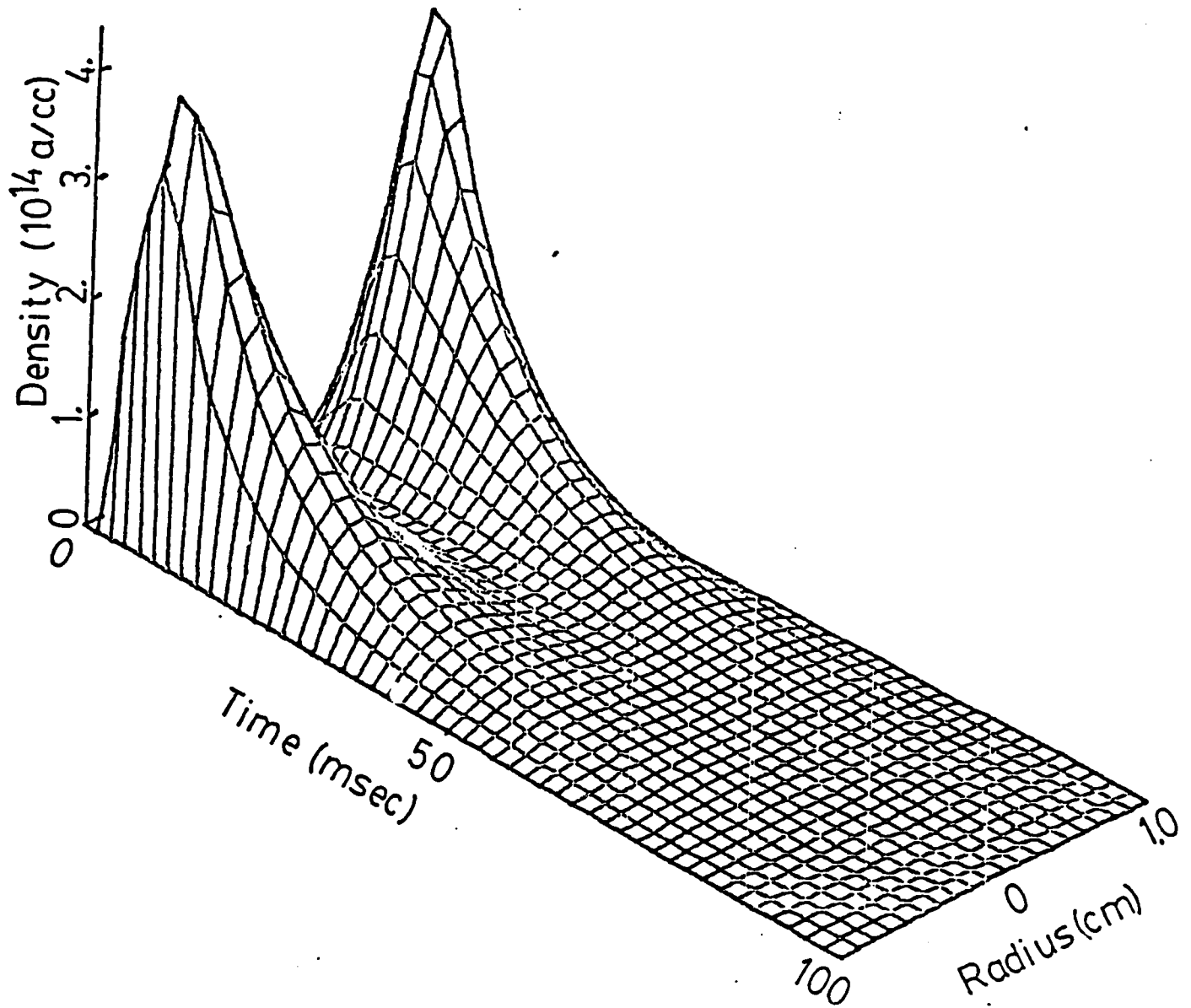


Figure B8 Time and spatial dependence with  $K_H = 50 \text{ sec}^{-1}$ .

Table B4

## DIFFUSION RATES FOR EACH REGION (1mm SPACING)

<u>X</u>	<u><math>1/\tau_0</math> (12 msec)</u>	<u><math>1/\tau_0</math> (100 msec)</u>
.9	111 sec <sup>-1</sup>	10 sec <sup>-1</sup>
.8	50	10
.7	15	9
.6	6	8
.5	-10	6
.4	-10	5
.3	-27	3
.2	-55	2
.1	-78	.9
0	-210	.5
	$\langle 1/\tau_0 \rangle = 45$	$\langle 1/\tau_0 \rangle = 8.0$

(- represents gain due to diffusion from adjacent regions)  
 $K_H = 0$

## APPENDIX B

REFERENCES

- B1. A. C. Hindemarsch, UCID-30001, UCRL-S1186, UC1D 30050, Lawrence Livermore Laboratory, P. O. Box 808, Livermore CA, 94550.
- B2. W. P. Jesse and J. Sadauskis, Physical Review, 90 1120 (1953).
- B3. S. J. S. Nagalingam, M.S. Thesis, University of Illinois, 1981
- B4. G. Bekefi, Principles of Laser Plasmas, John Wiley & Sons, New York, New York, (1976).
- B5. A Chung, M. Prelas, 1983 IEEE International Conference on Plasma Science, San Diego, 6A5 May (1983).
- B6. Guyot, G. H. Miley and J. T. Verdeyen, Nucl. Sci. Eng., 48, 373 (1972).
- B7. E. W. McDavid, et al. Technical Report H-78-1, U. S. Army Missile Research and Development Command, 1487, Dec. (1978).
- B8. J. B. Landenslager, W. T. Hunter, and M. T. Bowers., J. Chem. Phys. 61, 4600 (1974).
- B9. N. G. Adams, D. K. Blanchard and E. E. Ferguson, J. Chem. Phys., Vol 52, No. 10, 5101 (1970).
- B10. R. H. Lo and G. H. Miley, IEEE Trans on Plasma Science, PS-2, pp 198-205 (1974).
- B11. G. Fournier, J. Bonnet, J. Bridet, J. Fort, and D. Pigache, Journal De Physique C7, 40, 777 (1979). G. Fournier, J. Bonnet and D. Pigache, J. Phys. Letters 41, L-173 (1980).
- B12. D. Shure and J. T. Verdeyen, J. Appl. Phys. Vol. 47, No. 10, 4484 (1976).
- B13. R. I. Hall and S. Trajmar, J. Phys. B: Atom. Molec. Phys.
- B14. J. Keck, J. Chem. Phys. Vol. 32, No. 4, 1035 (1960).
- B15. C. B. Krefschmer, Aerojet Report #1611, Azusa, CA (1959).
- B16. E. Bauer and M. Salkoff, J. Chem. Phys. Vol. 33, No. 4, 1201 (1960).
- B17. D. L. Matthews, Phys. Fluids, 2, 170 (1959).
- B18. K. L. Wray, J. Chem. Phys., Vol. 37, No. 6, 1254 (1962).
- B19. R. A. Young and R. L. Sharpless, J. Geo. Res. 67, No. 10, 3871 (1962).



- B20. R. A. Young and R. L. Sharpless, J. Chem. Phys. Vol. 39, No. 4, 1071 (1963).
- B21. A. M. Falick, B. H. Mahan, and R. S. Myers, J. Chem. Phys. 42, 1837 (1965).
- B22. R.A. Young and G. Black, J. Chem. Phys. Vol. 44, No. 10, 3741 (1966).
- B23. K. G. Vohra, P.V. N. Nair and T. S. Muraleedharan, Aerosol Science, Vol. 3, pp. 225-236 (1972), R. H. Kummier, G. E. Report N-10875 (1968), R. H. Kummier and M. H. Bortuer, G. E. Report R675020 (1967).
- B24. R. P. Wayne, Advances in Photo Chemistry, Vol. 7, 311 (1969).
- B25. DASA Reaction Rate Handbook (Defense Atomic Support Agency Report #1848m RD 8214571, Oct. (1967).
- B26. F.E. Niles, J. Chem. Phys. Vol. 52, No. 1, 408 (1970).
- B27. P. V. Danckwint, Trans. Faraday Soc. 47 (1951) 1014.